Simulation Studies of Liquids, Supercritical Fluids and Radiation Damage effects

Chenxing Yang

Submitted in partial fulfillment
of the requirements of the Degree of
Doctor of Philosophy

5 December 2016

School of Physics and Astronomy
Queen Mary, University of London

Queen Mary
University of London

Statement of originality

I, Chenxing Yang, confirm that the research included within this thesis is my own work or that where it has been carried out in collaboration with, or supported by others, that this is duly acknowledged below and my contribution indicated. Previously published material is also acknowledged below.

I attest that I have exercised reasonable care to ensure that the work is original, and does not to the best of my knowledge break any UK law, infringe any third party's copyright or other Intellectual Property Right, or contain any confidential material.

I accept that the College has the right to use plagiarism detection software to check the electronic version of the thesis.

I confirm that this thesis has not been previously submitted for the award of a degree by this or any other university.

The copyright of this thesis rests with the author and no quotation from it or information derived from it may be published without the prior written consent of the author.

.....

Chenxing Yang

5 December 2016

Acknowledgements

First of all, I would like to thank my supervisors Dr. Kostya Trachenko and Prof. Martin Dove for their guide and support during my Phd study. I am grateful to Kostya for his close guidance, proposing ideas for this project and pointing me in the direction when I was stuck. I thank Martin for teaching me how to seriously perform simulation and showing me different approaches to solving problems. It is my great pleasure to have the opportunity to work with them. This work would not be possible without their help.

I am grateful to our collaborators Prof. Vadim Brazhkin for suggestion and discussion for Supercritical fluid and Dr Stephen Hull for yttrium-stabilised zirconia. Their knowledge and insight contribute significantly to this work.

I am grateful to all the academics in CCMMP group, especially Dr Anthony Phillips and Dr Alston Misquitta for discussion and advise. I thank Dr Evangelia Zarkadoula for teaching me to run cascade simulation at the beginning of my Phd. I thank Asmi Barot, Ling Wang, Huangqing Ye, Yuanpeng Zhang, Rory Gilmore and Min Gao for useful and interesting discussion. I thank Tingting Zhang for proofreading my thesis.

Finally, I wish to thank my parents for supporting every decision I made even for those which they disagreed.

This work was supported by the China Scholarship Council.

Abstract

The work in this thesis aims to gain fundamental understanding of several important types of disordered systems, including liquids, supercritical fluids and amorphous solids on the basis of extensive molecular dynamics simulations. I begin with studying the diffusion in amorphous zirconolite, a potential waste form to encapsulate highly radioactive nuclear waste. I find that amorphization has a dramatic effect for diffusion. Interestingly and differently from previous understanding, diffusion increases as a result of amorphization at constant density. Another interesting insight is related to different response of diffusion of different atomic species to structural disorder. I calculate activation energies and diffusion pre-factors which can be used to predict long-term diffusion properties in this system. This improves our understanding of how waste forms operate and provides a quantitative tool to predict their performance. I subsequently study the effects of phase coexistence and phase decomposition in Y-stabilized zirconia, the system of interest in many industrial applications including in encapsulating nuclear waste due to its exceptional resistance to radiation damage. For the first time I show how the microstructure emerges and evolves in this system and demonstrate its importance for self-diffusion and other properties. This has not been observed before and is important for better understanding of existing experiments and planning the new ones.

I subsequently address dynamical properties of subcritical liquids and supercritical fluids. I start with developing a new empirical potential for CO_2 with improved performance. Using this and other potentials, I simulate the properties of supercritical H_2O, CO_2 and CH_4 and map their Frenkel lines in the supercritical region of the phase diagram. I observe that the Frenkel line for CO_2 coincides with experimentally found maxima of solubility and

explain this finding by noting that the Frenkel line corresponds to the optimal combination of density and temperature where the density is maximal and the diffusion is still in the fast gas-like regime. This can serve as a guide in future applications of supercritical fluids and will result in their more efficient use in dissolving and extracting applications.

I extend my study to collective modes in liquids. Here, my simulations provide first direct evidence that a gap emerges and evolves in the reciprocal space in transverse spectra of liquids. I show that the gap increases with temperature and is inversely proportional to liquid relaxation time. Interestingly, the gap emerges and evolves not only in subcritical liquids but also in supercritical fluids as long as they are below the Frenkel line. Given the importance of phonons in condensed matter physics and other areas of physics, I propose that the discovery of the gap represents a paradigm change. There is an active interest in the dynamics of liquids and supercritical fluids, and I therefore hope that my results will quickly stimulate high-temperature and high-pressure experiments aimed at detecting and studying the gap in several important systems.

Contents

List of Abbreviations

MD	Molecular Dynamics
MC	Monte Carlo
GEMC	Gibbs ensemble Monte Carlo
NVE	Microcanonical ensemble
NPT	Isothermal-isobaric ensemble
NVT	Canonical ensemble
μPT	Grand canonical ensemble
NIST	National Institute of Standards and Technology
EPM	elementary physical model
TraPPE	transferable potentials for phase equilibria
SYNROC	synthetic rock
DFT	density function theory
DMA	Distributed Multi-pole Analysis
VACF	velocity autocorrelation function
FL	Frenkel Line

Chapter 1

Introduction

1.1 Liquids and supercritical fluids: challenge of structural and dynamical disorder

Traditionally, solid state physics was almost exclusively about ordered systems, crystals [1]. Crystallinity and periodicity give rise to several important concepts and approaches which significantly simplify physical description: the reciprocal space, plane waves describing collective modes and electronic states, analysis of structure, symmetry changes and phase transitions and so on. These concepts are used to construct theories of thermodynamic properties in most system. Those properties include energy, heat capacity and entropy as well as dynamical and transport properties. The absence of crystallinity in amorphous systems such as glasses or crystals amorphized by radiation damage has been viewed as a serious challenge for their understanding. These challenges continue to stimulate the ongoing research into disordered systems. To a large extent, these challenges have stimulated my work in this thesis.

Condensed matter as a term originated from adding liquids to solid state

physics. As far as we can tell, one of the first proposals dates back to 1930s when J. Frenkel proposed to develop liquid theory as a generalization of solid state theory and unify the two states under the term "condensed bodies" [2]. Liquids bring about another challenge for theory: the dynamical disorder. Particles in liquids jump between quasi-equilibrium positions [2] and so no fixed reference state exist as in the case of solids, crystalline or amorphous. For this reason, the community was compelled to treat liquids as general disordered statistical systems with no simplifying assumptions as those used in the solid state theory. Importantly, inter-particle interactions in liquids are strong and are comparable to those in solids. This means that a perturbation theory, widely used to treat weakly-interacting gases [3], can not directly apply[1]. Because interactions are both strong and system-specific, Landau and Lifshitz state in their textbook [6] that no general expression for liquid thermodynamic properties such as energy can be obtained. Although great strides have been achieved in our understanding of liquids [7–14], there are still important questions remaining, including understanding and predicting most basic liquid thermodynamic properties such as specific heat [15].

Notably, recent results from experiments and theory start to lift this pessimistic view about liquids [16]: in many important respects, liquids are close to solids. In particular, liquids are capable of supporting high-frequency solid-like collective modes, and this ability can be used to construct their thermodynamic theory. There are important differences in ways in which collective modes operate in solids and liquids, and these differences continue to stimulate the ongoing liquid research [17–26]. A large part of my thesis is dedicated to studying how collective modes propagate in liquids. Of particular importance here is my discovery of the emergence and evolution of the gap in the reciprocal

[1] one approach to apply perturbation theory on liquid is based on density function theory approximation [4, 5]

space in liquids and supercritical fluids.

The third theoretical motivation comes from the need to better understand the properties of matter above the critical point. In the last couple of decades, supercritical fluids started to be widely deployed in many important industrial processes [27, 28] thanks to their high dissolving and extracting properties. These properties are unique to supercritical fluids and originate from the combination of high density and particle mobility. However, little is known about the supercritical state of matter from theoretical standpoint, apart from a common general assertion that no difference can be made between a liquid and a gas above the critical point and that the supercritical state should probably be viewed as a homogenous dense hot matter [27, 28]. More recently, there were several attempts to develop a more specific picture of the supercritical matter, and of them is the proposal of the Frenkel line separating two supercritical states with liquid-like and gas-like properties [29–31]. The Frenkel line was mapped on the phase diagram for a model Lennard-Jones system only, and this stimulated my work to locate the line for several real important systems such as H_2O, CO_2 and CH_4. This work includes developing a reliable interatomic potential that can be used to model high-temperature and high-pressure of CO_2 in the supercritical state.

1.2 Radiation damage effects

Another main motivation behind my work in this thesis stems from the need to safely encapsulate nuclear waste, the important and pressing challenge that modern society faces. A variety of radiation sources are created and used in science and technology. This includes an important area of energy generation in nuclear power stations, where kinetic energy of fission products

is converted into heat and electricity. In this and other applications, the energy of emitted particles often has a two-fold effect. On one hand, this energy is converted into useful energy, by heating the material around the particle tracks. On the other hand, this energy damages the material and degrades its important properties, including mechanical, thermal, transport and so on, to the point that a material might lose its functional purpose. A problem in fission and future fusion reactors [32–34], this issue is particularly acute in the process of safe immobilization of nuclear waste, and constitutes one of the pressing issues that modern society faces [35, 36]. The issue is closely related to public acceptance of nuclear industry and therefore to the future of nuclear power. Regardless of the future of nuclear industry, the amount of accumulated nuclear waste is very large and is steadily growing while no acceptable solution of its safe storage exists.

Solid ceramic materials ("waste forms") have been proposed to encapsulate highly-radioactive nuclear waste [35–39], and this poses both technological and scientific challenges. The main requirement for the immobilisation matrix, the waste form, is to prevent the radioactive isotopes from leaking and polluting the environment. This is perceived to be a very challenging requirement, given the high radioactivity of the nuclear waste and the long radioactivity time spans that extend from several thousand years for fission products to several million years for actinides. As recently observed [39], nuclear waste encapsulation involves "design problem the likes of which humanity had never before attempted, because it involved a time scale that required predictions of material and system behaviour tens and hundreds of thousands of years into the future. Some perspective on the uniqueness of this temporal projection comes from the realisation that the most ancient monuments of past engineering achievement, such as Stonehenge and the Pyramids, are barely

five thousand years old." With no direct testing possible over long periods of time, the decision of using a particular waste form needs to be informed by indirect simulated experiments as well as detailed theoretical understanding of how irradiation affects the ability of the waste form to remain an effective immobilisation barrier.

In this thesis, I study the diffusion in amorphous zirconolite $CaZrTi_2O_7$, the material currently considered by the UK Nuclear Decommissioning Authority as a potential waste form. The atomic diffusion plays the key role for immobilizing highly radioactive atoms and recrystallisation. Therefore it is important to understand the diffusion in the wast form after being completely damaged. I also address the modelling of Yttrium-stabilised zirconia (ZrO_2) and develop an interatomic potential that can be used to model radiation damage effects in this system. ZrO_2 is very interesting due to its exceptional resistance to amorphization by radiation damage [40, 41]. Understanding the structure before damage is crucial for further radiation damage study.

As a result of several different motivations discussed above, my thesis consists of two main areas: understanding the effects of radiation damage in amorphous materials and understanding dynamics of liquids and supercritical fluids. Although these two areas may seem different, they share some common properties and applications. Both are disordered systems which are not well understood as discussed below. In terms of applications, both systems of them can be related to safe encapsulation of nuclear waste, because the supercritical fluids have been proposed as an alternative to acids to extract and dissolve radioactive waste coming from nuclear power stations [42, 43]. Studying these two areas can be beneficial to two important process of dealing safely with nuclear waste, namely that nuclear waste can be transported by supercritical fluids, then immobilised by solid ceramic materials.

1.3 Thesis outline

As mentioned above, this thesis includes two main areas of study. Chapters 3 and 4 are related to radiation damage effects. Chapters 5, 6 and 7 are related to the dynamics of liquids. In Chapter 2, methods related to my simulations is introduced. Firstly, I discuss the algorithms of integrate Newton's equation, ensembles and rigid bodies. Then I described how to calculate the interactions of particles in molecular dynamics simulation such as Coulomb interactions and short-range interactions.

In Chapter 3, the simulation results of atomic diffusion in solid zirconolite is discussed. It focuses on how amorphization and density can affect the atomic diffusion in the material.

In Chapter 4, I analyse the crystal structure of Yttria-stabilized zirconia, $Zr_{1-x}Y_xO_{2-x/2}$ and discuss how Y doping changes zirconia structure. The analysis is done in a wide range of Y (0–25 %). Then I discuss how the emergent structure can affect O diffusion in $Zr_{1-x}Y_xO_{2-x/2}$.

In Chapter 5, I discuss the development of new CO_2 interatomic potential and test the vapour-liquid coexistence line for this model.

In Chapter 6, I discuss the Frenkel line and calculate the Frenkel line of CO_2, H_2O and CH_4 in the supercritical region on the phase diagram. Then I discuss how the experimentally observed solubility maximum can be related to the Frenkel line.

In Chapter 7, I analyse the dynamical properties of liquids and supercritical fluids and study the collective modes in these systems. I calculate high-frequency solid-like transverse modes and their temperature evolution in both

subcritical liquids and supercritical fluids. I find that the gap emerges in the reciprocal space and widens with temperature. On the basis of these results, I establish a quantitative relationship between the gap and liquid relaxation time.

Chapter 2

Methods

The main method used in this thesis is classical molecular dynamics (MD) simulations discussed in the next section. Due to fast development of computing technology, we can now study what used to be very challenging. The new developments include the ability to simulate large system sizes, parallel simulations required to average the results as well as more comprehensive detailed analysis. In this chapter, I discuss the MD method and algorithms used.

2.1 Molecular dynamics simulation

The main advantage of MD is that it can directly study the dynamical properties of the system such as structure, structural transformations, system thermodynamic properties as well as dynamical behaviour including collective modes, diffusion coefficients and so on. Provided reliable interatomic potentials are used, classical MD simulations can give reliable results that can be directly compared to experimental results and theoretical predictions.

An MD simulation is based on the classical Newton's equations, namely

$force = mass \times acceleration$. The choice of algorithms of integrating Newton's equation is crucial for the MD simulation. A simulation provides a full trajectory of the system in the phase space, including particles coordinates and momenta. The initial configuration and the interatomic potential are specified from the outset. To calculate the new position of particles, the Taylor expansion of the spatial coordinate can be used both forward and backward in time t:

$$\begin{aligned}
\mathbf{r}(t+\Delta t) &= \mathbf{r}(t) + \frac{\partial \mathbf{r}(t)}{\partial t}\Delta t + \frac{1}{2}\frac{\partial^2 \mathbf{r}(t)}{\partial t^2}(\Delta t)^2 + \cdots && (2.1)\\
&= \mathbf{r}(t) + \mathbf{v}(t) + \frac{\mathbf{f}(t)}{2m}(\Delta t)^2 + \cdots && (2.2)\\
\mathbf{r}(t-\Delta t) &= \mathbf{r}(t) - \frac{\partial \mathbf{r}(t)}{\partial t}\Delta t + \frac{1}{2}\frac{\partial^2 \mathbf{r}(t)}{\partial t^2}(\Delta t)^2 + \cdots && (2.3)\\
&= \mathbf{r}(t) - \mathbf{v}(t) + \frac{\mathbf{f}(t)}{2m}(\Delta t)^2 + \cdots && (2.4)\\
& && (2.5)
\end{aligned}$$

where, the Δt is timestep, $v(t)$ is velocity, $f(t)$ is the force and m is the mass. The new position and velocity can be calculated by adding and subtracting the above two equations:

$$\begin{aligned}
\mathbf{r}(t+\Delta t) &= 2\mathbf{r}(t) - \mathbf{r}(t-\Delta t) + \frac{\mathbf{f}(t)}{m}(\Delta t)^2 + O(\Delta t)^4 && (2.6)\\
\mathbf{v}(t) &= \frac{\mathbf{r}(t+\Delta t) - \mathbf{r}(t-\Delta t)}{2\Delta t} + O(\Delta t)^3 && (2.7)
\end{aligned}$$

This is known as Verlet algorithm.

It can be seen that the velocity is always less accurate than the position, and that the calculation of velocity is always one step behind of position. As we can see in Eq. (2.7), the velocity, at time t, is calculated based on the position at time $t + \Delta t$ and $t - \Delta t$. However, there is a way to calculate the velocity at the same time and also improve the accuracy by introducing a half step:

$$\mathbf{v}(t + \Delta t/2) = \mathbf{v}(t) + \frac{1}{2}\frac{\partial^2 \mathbf{r}(t)}{\partial t^2}\Delta t \qquad (2.8)$$

substituting above equation into Eq. (2.1) and (2.2) gives:

$$\mathbf{r}(t+\Delta t) = \mathbf{r}(t) + \mathbf{v}(t+\Delta t/2)\Delta t \tag{2.9}$$

The velocity for the new timestep $t+\Delta t$ can be calculated as:

$$\mathbf{v}(t+\Delta t) = \mathbf{v}(t+\Delta t/2) + \frac{1}{2}\frac{\partial^2 \mathbf{r}(t+\Delta t)}{\partial t^2}\Delta t \tag{2.10}$$

Substituting Eq. (2.8) into above equation gives:

$$\mathbf{v}(t+\Delta t) = \mathbf{v}(t) + \frac{1}{2}\left(\frac{\partial^2 \mathbf{r}(t+\Delta t)}{\partial t^2} + \frac{\partial^2 \mathbf{r}(t)}{\partial t^2}\right)\Delta t \tag{2.11}$$

This method is called Velocity Verlet algorithm, which is the default integration method in the MD package we use, DL_POLY [44].

The timestep is important for the accuracy of the result. One way to increase the accuracy is to use smaller timestep, but this increases the computational cost. Another way is to use large timestep by storing information about higher order derivatives. Although higher-order algorithms tend to have very good energy conservation for short times, the energy may drift for long times. Verlet algorithm tends to have moderate energy conservation at short times and little drift at longer times.

MD simulation can be a very powerful approach if we consider its limitation. System size provides some constraints in the system. For instance, the wave number of phonon is restricted by the periodic boundary conditions $2n\pi/L$, where L is the system size and n is an integer. Furthermore, we expect the system to be ergodic, but MD is a non-ergodic system. It means that simulating longer time does not necessarily give better statistical results. Another thing we need to worry about is the force field. The most common force field used in MD simulation is empirical potential. The empirical potential can not describe quantum effects, such as Jahn-Teller effect or vibrational motion with

a frequency ν where h$\nu > k_{\mathrm{B}}T$.The potential is usually fitted based on the known experimental results, which makes empirical potential an inappropriate tool for structure predication of unknown phases of a material.

MD simulation used be able to be performed with the system size $\sim 10^5$. By using the UK's largest supercomputer ARCHER and state-of-the-art MD code DL_POLY, I am able to perform the MD simulation with the system size $\sim 10^6$. Thus some large scale system, such as radiation damage events, can be simulated, which used to be thought impossible [33, 34].

2.2 Thermodynamic ensembles

2.2.1 Microcanonical ensemble

Since the MD simulation obeys Newton's equation, it automatically satisfies energy conservation. A popular ensemble keeps the energy, volume and the number of particle constant. This ensemble is called microcanonical (NVE) ensemble. The Hamiltonian of this ensemble can be written as:

$$\mathcal{H} = \sum_i \frac{p_i^2}{2m_i} + \frac{1}{2}\sum_i E_p(\mathbf{r}_i) \tag{2.12}$$

where p_i is the momentum of atom i, m_i is the mass, and $E_p(\mathbf{r}_i)$ is the potential energy of atom i at position $\mathbf{r}_i$. The factor $\frac{1}{2}$ is due to the double counting.

Keeping constant volume and energy is not enough to cover all the situation, because most experiments are performed under controlled temperature and pressure. In this case, the constant pressure or temperature ensemble (NPT) is used [45].

2.2.2 Constant pressure or stress ensembles

To perform MD simulation at constant pressure or stress, the size and the shape of the configuration need to be allowed to change during the simulation. Ranmann and Parinello [46, 47] found a successful approach by introducing new dynamical variables **h** into the Hamiltonian:

$$\mathcal{H} = \frac{1}{2}\sum_i m_i \dot{\mathbf{s}}_i^{\mathrm{T}} \cdot (\mathbf{h}^{\mathrm{T}} \cdot \mathbf{h}) \cdot \dot{\mathbf{s}}_i + \frac{1}{2}\sum_i E(\mathbf{s}_i, \mathbf{h}) + \frac{1}{2} M \,\mathrm{Tr}(\dot{\mathbf{h}}^{\mathrm{T}} \cdot \dot{\mathbf{h}}) + PV \qquad (2.13)$$

where **h** is a square matrix constructed by three edge vectors of configuration as **a**, **b** and **c**, and $\mathbf{s}_i$ is the column vector of fractional coordinates x_i, y_i and z_i. The position of atom i is: $\mathbf{r}_i = \mathbf{h} \cdot \mathbf{s}_i = x_i\mathbf{a} + y_i\mathbf{b} + z_i\mathbf{c}$. The symbol M is the effective mass. The effective mass does not affect the size of fluctuations of configuration, but their time scale. In this case the effective mass can be related to a time constant, which is the formulation used in DL_POLY.

2.2.3 Constant temperature ensemble

One way to achieve constant temperature is to scale the velocities of atoms during the simulation [45]. At the beginning of the MD simulation, the atoms are assigned a set of velocities that corresponding to a given temperature. However the configuration of the system may not correspond to an equilibrium state. In this case the velocities need to be re-scaled periodically until the temperature oscillates around a mean value. The simulation can be subsequently run in the NVE ensemble and we can collect the data. However, the above re-scaling method has no robust basis in statistical mechanics, and can be only used to prepare a system. Nosè [48] proposed to introduce an artificial coordinates s into the Hamiltonian:

$$\mathcal{H} = \sum_i \frac{p_i^2}{2m_i s^2} + \frac{1}{2}\sum_i E(\mathbf{r}_i) + \frac{1}{2} Q\dot{s}^2 + (3N+1)k_{\mathrm{B}}T \ln s \qquad (2.14)$$

where N is the number of particles and Q is the effective mass. The variable s can be viewed as effectively scaling time. As we can see, the temperature fluctuates around a mean value, corresponding to a heat bath in contact with the system.

2.2.4 Grand canonical ensemble (Gibbs ensemble)

The Gibbs ensemble is widely used to simulate liquid-vapour and liquid-liquid coexisting phase. Different from the ensemble described above, the Gibbs ensemble is used in Monte Carlo (MC) simulation by default, and there are some recent developments of using the Gibbs ensemble in MD simulations [49–51]. Temperature, pressure and chemical potential μ are the same for two states in the coexisting phase. Thus, the ideal ensemble for simulating the coexisting phase is μPT ensemble. However, μ, P and T are all intensive properties, which leaves extensive property unbounded. At least one of the extensive property must be fixed for a proper ensemble.

The Gibbs ensemble, proposed by Panagiotopoulos [52], is the combination of the NVT, NPT and μPT ensemble. The schematic sketch of Gibbs ensemble is shown in Fig. 2.1. The Gibbs ensemble contains two subsystems. The total volume $V = V_A + V_B$ is constant, the total number of particle $N = N_A + N_B$ is constant and the temperature is also constant, but the volume and particles can exchange between two boxes. Each MC step involves three trial moves: (1) displace a randomly selected particle; (2) change the volume of boxes while maintaining the total volume constant; (3) move a randomly selected particle from one box to another. When the whole system reaches to the equilibrium state, the chemical potential μ and pressure P of two subsystems are equal to each other.

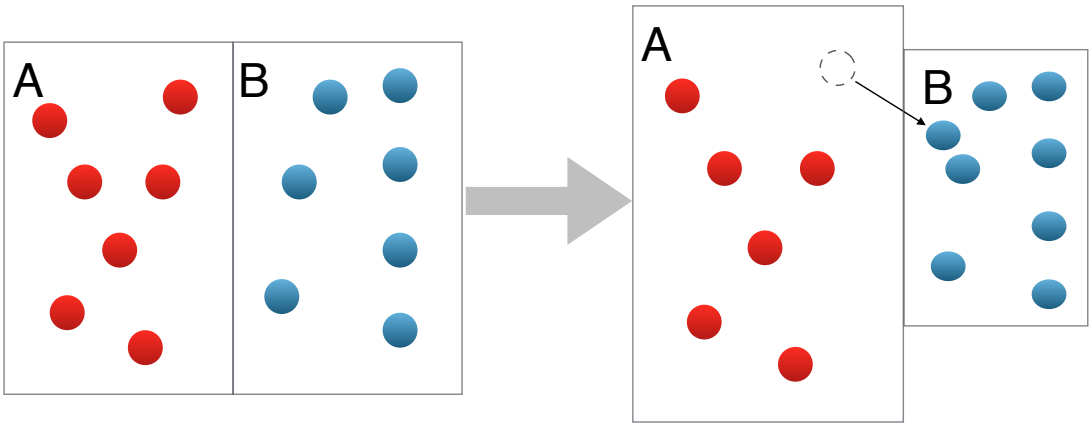

Figure 2.1: Schematic sketch of Gibbs ensemble. Two system can exchange both particles and volume.

2.3 Rigid bodies

Rigid bodies are used to model a set of atoms whose local structure does not change during the simulation. Since the frequency of intramolecular vibration is usually much higher than inter-molecular frequency, it is necessary to use much smaller timestep to capture the motion of atoms, which causes more computational cost. Moreover, it can also cause some problems when there is a massless charge site inside the molecule, such as TIP4P water potential. For those reasons, using rigid bodies can both save computational cost and avoid problems.

The motion of rigid bodies can be described as translation of the centre of mass and rotation about the centre mass. The difficulty of describing the rotation is that the operators do not commute with each other. The rotation can be described by Euler angles. If the system is first rotated by an angle α around the z axis, then rotated an angle β around the new y axis and finally rotated

an angle γ about the new z axis, the rotation matrix is defined as:

$$\mathbf{R} = \begin{pmatrix} \cos\alpha\cos\gamma - \cos\beta\sin\alpha\sin\gamma & \sin\alpha\cos\gamma + \cos\alpha\cos\beta\sin\gamma & \sin\beta\sin\gamma \\ -\cos\alpha\sin\gamma - \sin\alpha\cos\beta\cos\gamma & -\sin\alpha\sin\gamma - \cos\alpha\cos\beta\cos\gamma & \sin\beta\cos\gamma \\ \sin\alpha\sin\beta & -\cos\alpha\sin\beta & \cos\beta \end{pmatrix} \tag{2.15}$$

However, there is a problem with using Euler angles. If $\beta = 0$ the first and third rotation becomes identical:

$$\mathbf{R} = \begin{pmatrix} \cos(\alpha+\gamma) & \sin(\alpha+\gamma) & 0 \\ -\sin(\alpha+\gamma) & -\cos(\alpha+\gamma) & 0 \\ 0 & 0 & 1 \end{pmatrix} \tag{2.16}$$

As a result the system loses one degree of freedom. This would cause instability in the MD simulation. The problem can be avoided by using four new variables called quaternions. A quaternion is a four-dimensional unit vector defined as:

$$\begin{aligned} q_0 &= \cos\frac{\alpha+\gamma}{2}\cos\frac{\beta}{2} & q_1 &= \cos\frac{\alpha-\gamma}{2}\sin\frac{\beta}{2} \\ q_2 &= \sin\frac{\alpha-\gamma}{2}\sin\frac{\beta}{2} & q_3 &= \sin\frac{\alpha+\gamma}{2}\cos\frac{\beta}{2} \end{aligned} \tag{2.17}$$

The rotation matrix can be written as:

$$\mathbf{R} = \begin{pmatrix} q_0^2+q_1^2-q_2^2-q_3^2 & 2(q_1q_2+q_0q_3) & 2(q_1q_3-q_0q_2) \\ 2(q_1q_2-q_0q_3) & q_0^2-q_1^2+q_2^2-q_3^2 & 2(q_2q_3+q_0q_1) \\ 2(q_1q_3+q_0q_2) & 2(q_2q_3-q_0q_1) & q_0^2-q_1^2-q_2^2+q_3^2 \end{pmatrix} \tag{2.18}$$

In DL_POLY, the rotation of rigid body is defined by this quaternion matrix.

2.4 Ewald sum

The problem of calculating the Coulomb interaction is that interactions are long-ranged. The computational cost increases with the range of the interaction, since more pairs of atoms need to be included in the calculation. Using

truncation of distance for interaction would cause problems for energy conservation when the interaction switches on and off at a pre-defined distance. If simulating a periodic system, the interaction range would exceed the size of the MD box. The Ewald's sum is a method to calculate long-range interaction in a periodic system. [45, 53]

The Ewald method divides the Coulomb interaction into short-range and long-range contributions. The short-range contribution is calculated in real space and the long-range contribution is calculated in reciprocal space. For mathematical convenience, the quantity $1/r$ is presented as a definite integral of a Gaussian function:

$$\frac{1}{r} = \frac{2}{\sqrt{\pi}} \int_0^\infty \exp(-r^2\rho^2)\,\mathrm{d}\rho \tag{2.19}$$

The Coulomb energy can be written as:

$$E_\mathrm{C} = \frac{1}{2} \sum_\ell \sum_{i,j} \frac{Q_i Q_j}{2\pi^{3/2}\epsilon_0} \int_0^\infty \exp(-r_{ij}^2(\ell)\rho^2)\,\mathrm{d}\rho \tag{2.20}$$

where i and j are labels of atoms, r_{ij} is the distance between atoms i and j. Q is the charge of that atom and l is the label of the periodic configuration. The integral can be separate into two parts:

$$\int_0^\infty \exp(-r^2\rho^2)\,\mathrm{d}\rho = \int_0^g \exp(-r^2\rho^2)\,\mathrm{d}\rho + \int_g^\infty \exp(-r^2\rho^2)\,\mathrm{d}\rho \tag{2.21}$$

$$= \int_0^g \exp(-r^2\rho^2)\,\mathrm{d}\rho + \frac{\sqrt{\pi}}{2}\frac{\mathrm{erfc}(gr)}{r} \tag{2.22}$$

where g is the convergence parameter, and $\mathrm{erfc}(x)$ is called the complementary error function defined as:

$$\mathrm{erfc}(x) = \frac{2}{\sqrt{\pi}} \int_x^\infty \exp(-y^2)\,\mathrm{d}y \tag{2.23}$$

The first term represents an atom j interacting with charge cloud located at site j with the same charge as that atom. The second term becomes the point

change surrounded by the opposite charge cloud, which falls to zero rapidly with increasing r. Transforming the first term in the reciprocal space, we write:

$$\frac{2}{\sqrt{\pi}}\sum_{\ell}\exp(-r_{ij}^2(\ell)\rho^2) = \frac{2\pi}{V}\sum_{\mathbf{G}}\rho^{-3}\exp(-G^2/4\rho^2)\exp(i\mathbf{G}\cdot\mathbf{r}_{ij}) \tag{2.24}$$

where $\mathbf{r}_{ij}$ is the vector between atoms i and j, V is the volume of the box, and G is a reciprocal lattice vector. The integral gives:

$$\int_0^g \rho^{-3}\exp(-G^2/4\rho^2)\exp(i\mathbf{G}\cdot\mathbf{r}_{ij})\,\mathrm{d}\rho = \frac{2\exp(-G^2/4g^2)}{G^2}\exp(i\mathbf{G}\cdot\mathbf{r}_{ij}) \tag{2.25}$$

The problem with the above equation is that the atom would interact with itself when $l = 0$ and $i = j$. We can calculate this self-energy term from the real-space summation as:

$$E_{\text{self}} = \lim(r\to 0)\frac{1}{2}\sum_i \frac{Q_i^2}{4\pi\epsilon_0}\frac{\operatorname{erfc}(gr)-1}{r} \tag{2.26}$$

$$= -\frac{1}{4\pi\epsilon_0}\sum_i \frac{gQ_i^2}{\sqrt{\pi}} \tag{2.27}$$

The total electrostatic energy equals the sum of Eq. (2.23), (2.25) and (2.27):

$$\begin{aligned} E_{\mathrm{C}} = \quad & \frac{1}{2}\sum_{ij}\frac{Q_iQ_j}{4\pi\epsilon_0}\frac{4\pi}{V}\sum_{\mathbf{G}}\frac{\exp(-G^2/4g^2)}{G^2}\exp(i\mathbf{G}\cdot\mathbf{r}_{ij}) \\ & +\frac{1}{2}\sum_{ij}\frac{Q_iQ_j}{4\pi\epsilon_0}\sum_{\ell}\frac{\operatorname{erfc}(gr_{ij}(\ell))}{r_{ij}(\ell)} - \frac{1}{4\pi\epsilon_0}\sum_i\frac{gQ_i^2}{\sqrt{\pi}} \end{aligned} \tag{2.28}$$

2.5 Interatomic potentials

The short-ranged interaction is calculated using empirical potentials. In my simulations, I used two types of potential: Lennard-Jones potential [54] and Buckingham potential [55].

In the Lennard-Jones potential, the strong short-range repulsion models strong repulsion due to Pauli exclusion when two atoms are come close to each other. This can be represented as:

$$\phi_r(r_{ij}) = A/r_{ij}^{12} \tag{2.29}$$

where A is a parameter and r_{ij} is the distance between atoms i and j.

The long-ranged part of attractive interaction can be due to fluctuating instantaneously induced dipoles. This is called dispersive interactions and can modelled as:

$$\phi_a(r_{ij}) = -B/r_{ij}^6 \tag{2.30}$$

where B is a parameter. The sum of two above terms gives the Lennard-Jones potential:

$$\phi(r_{ij}) = A/r_{ij}^{12} - B/r_{ij}^6 \tag{2.31}$$

The Lennard-Jones is usually used to describe the interactions in simple solids such as Ar and is commonly used to model liquids.

The Buckingham potential is similar to the Lennard-Jones, but the repulsive part is replaced by the more accurate Born-Mayer term:

$$\phi_{\text{repulsive}} = A\exp(-r_{ij}/\rho) \tag{2.32}$$

where both A and ρ are adjustable parameters. The Buckingham potential is written as:

$$\phi(r_{ij}) = A\exp(-r_{ij}/\rho) - C/r_{ij}^6 \tag{2.33}$$

2.6 General Utility Lattice Programme (GULP)

GULP is able to calculate energies and minimise the energy through relaxing the structure, physical properties such as elastic constants and lattice dynamics. It is commonly used to fit the parameters in majority of model potential based on experimental data and *ab initio* energies [56]. In the thesis, I used to GULP to develop the model for Yttrium stabilised zirconia and CO_2 and calculate phonon dispersion for CO_2.

2.7 DL_POLY

DL_POLY is a general purpose MD simulation software using classical mechanics. It can simulate both equilibrium and non-equilibrium system. Furthermore, DL_POLY_4 parallelisation is based on domain decomposition method, which makes DL_POLY a nearly perfect scalable. Those features make DL_POLY_4 a great tool for studying radiation damage effect and other systems.

In this thesis, the general procedure of a MD simulation is described as below. Firstly, the equilibration is simulated in NPT ensemble to ensure that the system is at given temperature and pressure. The first stage of equilibration is to speed up the process of reaching the equilibrium state by scaling the velocities of atoms, then the simulation is performed in NPT ensemble without scaling the velocities. After the measured properties no longer changes with running longer time in NPT ensemble, the simulation is performed in NVE simulation and collect data.

Chapter 3

Solid-state diffusion in amorphous zirconolite

In this chapter I discuss how structural disorder and amorphization affects solid-state diffusion, and consider zirconolite ($CaZrTi_2O_7$) as a currently important case study. It is currently considered by the UK Nuclear Decommissioning Authority as a potential "waste form", a material capable to safely immobilize highly-radioactive nuclear waste. By performing extensive molecular dynamics simulations, the effects of amorphization and density are disentangled. I show that a profound increase of solid-state diffusion takes place as a result of amorphization. The amorphization of a waste form is the result of structural decay of alpha-emitting radioactive ions, where most of the structural damage comes from heavy recoils in alpha-decay. Importantly, this can take place at the same density as in the crystal, representing an interesting general insight regarding solid-state diffusion. I find that increasing the volume in the amorphous system increases pre-factors of diffusion constants. I also find that atomic species in zirconolite are affected differently by amorphization and density change. My microscopic insights are relevant for understanding

how solid-state diffusion changes due to disorder and for building predictive models of operation of materials to be used to encapsulate nuclear waste.

3.1 Introduction

Waste form alteration, the main concern for the safe encapsulation of nuclear waste, is a complex phenomenon involving diffusion, leaching and dissolution [57, 58]. Understanding the effects of irradiation on waste form durability is challenging because the process is complex and includes many mechanisms at work [35, 36, 58]. Generally, waste form alteration as a result of irradiation can include chemical changes at the surface, reactions with water and other environmental agents, increase of solid-state diffusion of atoms in the bulk due to radiation damage, increased defect mobility, defects interaction and so on. The above processes can be system specific, yet have a common underlying mechanism, thermal diffusion. It is therefore important to understand diffusion in waste forms and its changes due to radiation damage, because the solid diffusion plays a key role on the recrystallization and the ability of immobilising highly radioactive atoms in encapsulation materials.

An important effect of irradiation on the waste form is the remarkable increase of diffusion as a result of radiation-induced amorphization [59, 60]. Seen in easily amorphizable materials, this effect has been thought to be either absent or reduced in materials resistant to amorphization by radiation damage [61]. However, even most resistant materials such as ZrO_2 still show considerable damage in the form of a large number of well-separated point defects [62].

An interesting possibility is having a waste form which is amorphized by radiation damage yet still shows low levels of alteration and continues to be an effective immobilization barrier. Zirconolite, $CaZrTi_2O_7$, is one of the

phases in SYNROC mixture of different ceramics each tailored to immobilize different ions present in the highly-radioactive nuclear waste [37, 38]. The SYNROC is a synthetic rock to immobilize the liquid nuclear waste form by compressing the SYNROC powder with nuclear waste using hot isostatic pressing process. The SYNROC is currently the preferred waste form by the UK National Decommissioning Authority for immobilization of actinides. In more recent experiments [57, 63, 64], zirconolite has been rendered X-ray amorphous by alpha-decay processes of Pu and, surprisingly and contrary to other materials, did not reveal significant chemical and physical alterations, witnessed by the absence of phase changes and microcracks even at fairly large volume increases. Furthermore, zirconolite maintained strong elastic response and overall chemical durability [57, 63, 65], in contrast to other materials studied. At the same time, the aqueous durability of zirconolite is strongly affected by radiation damage [65], with the evidence supporting diffusion-controlled ion exchange as the main mechanism of alteration of radiation-damaged zirconolite. These results call for further detailed investigation of the mechanisms involved in the alteration of this waste form and diffusion mechanism in particular.

According to current understanding, the increase of diffusion due to radiation-damaged system is due to the associated density decrease. Indeed, apart from rare examples such as Si, radiation-induced structural changes and amorphization are accompanied by density decrease. The effect of density on the activation energy for diffusion U (the energy needed by an atom to jump from its surrounding cage to the neighbouring quasi-equilibrium location) has been well understood since the early work of Frenkel [2]. When interatomic separations are at their equilibrium values in a solid, U is too high for the jump event to take place during any feasible time. However, if the cage can increase

its size (for example, due to thermal fluctuations) and open up a low-energy local diffusion pathway, the jump can proceed much faster. If Δr is the increase of the cage size required for the jump to take place, U is equal to the work required to expand the change elastically, and is

$$U = 8\pi G r \Delta r^2 \tag{3.1}$$

where G is shear modulus and r is the cage radius [2]. Note that the elastic energy to expand the sphere of radius r by amount Δr depends on shear modulus G only because no compression takes place at any point. Instead, the system expands by the amount equal to the increase of the sphere volume [2], resulting in a pure shear deformation. Indeed, the strain components u from an expanding sphere (noting that $u \to 0$ as $r \to \infty$) are $u_{rr} = -2b/r^3$, $u_{\theta\theta} = u_{\phi\phi} = b/r^3$ [66], giving pure shear $u_{ii} = 0$.

From a theoretical standpoint, density is considered to be the main factor governing G and hence U [2]. Indeed, when density decreases as a result of radiation-induced structural changes, the interatomic interaction strength decreases, reducing G. Further, Δr decreases due to the increase of the cage volume. Therefore, if G is constant at constant density, Eq. (3.1) makes two predictions. First, U reduces due to density decrease, the widely anticipated result corroborated by more recent work on diffusion processes in glasses and viscous liquids [67]. Second, U does not change at constant density.

In contrast to the density effect, the consequences of amorphization at *constant density* for diffusion are not understood. Indeed, if a structural change (e.g. amorphization or large accumulation of point defects and their clusters as in ZrO_2 [62]) takes place at constant density, the volume of the atomic cage around the diffusing atom does not change on average. However, the wide distribution of interatomic angles in the disordered structure leads to the

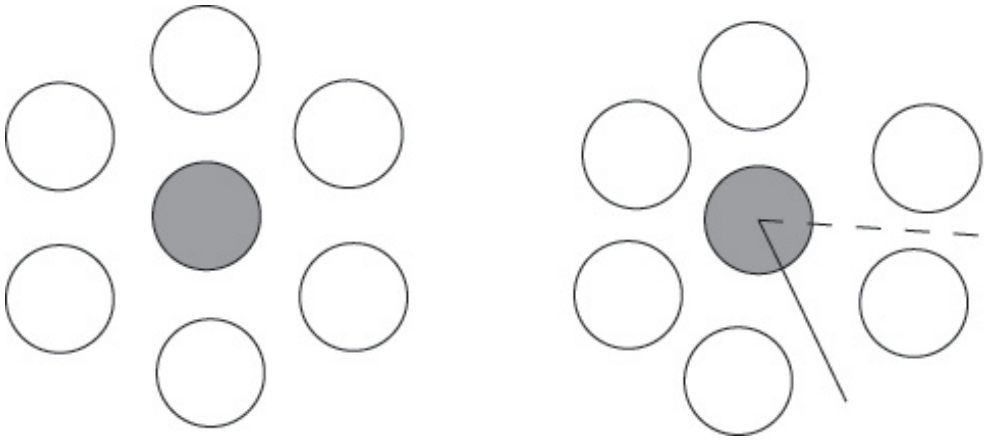

Figure 3.1: Schematic picture showing equivalent interatomic distances and local diffusion pathways in the crystalline structure (left). The disordered structure with the same density as the parent crystal has a wide distribution of interatomic distances and angles and gives rise to both faster (solid line) and slower (dashed line) local diffusion pathways.

appearance of both faster and slower local diffusion pathways (see Fig. 3.1), even if this structure is of the same density as the parent crystal, with the net effect of increasing the diffusion. This is an agreement with experimental results reporting the decrease of G as a result of amorphization at the same density [68].

Hard to estimate theoretically, the combined effect of local fast and slow diffusion pathways at the same density is important to understand from the waste form perspective [58] as well as from the general point of view of properties of disordered state. Indeed, since the early work [69], the extent to which structural disorder affects system properties remains to be widely debated. For example, recent work aimed at resolving the long-standing debate about the origin of the Boson peak in the energy spectrum of glasses, and has found that, contrary to earlier expectations, the difference of vibrational spectra and other important properties between the amorphous system and its parent crystal disappears once the densities of both systems are taken to be the same [70]. Generally, recently accumulated evidence suggests that disorder

leaves some important properties of the system surprisingly unaffected, but modifies other properties substantially [71].

In this chapter, I address an important element of waste form alteration, the change of thermal diffusion due to radiation damage in the waste form. I use molecular dynamics (MD) simulations to study the change of diffusion of different atomic species in zirconolite as a result of structural disorder. Importantly, MD simulations enable us to disentangle the effects of amorphization and density increase on diffusion and discuss these effects separately. Such a separation is very hard to achieve in experimental radiation-damaged samples. I find that a profound increase of solid-state diffusion takes place as a result of amorphization. Importantly, this can take place at the same density as in the crystal, representing an interesting general insight regarding solid-state diffusion. I find that increasing the volume in the amorphous system increases pre-factors of diffusion constants. I also find that atomic species in zirconolite are affected differently by amorphization and density change. My findings are relevant for both understanding solid-state diffusion in the presence of disorder and for building predictive models of operation of nuclear waste forms.

3.2 Methods

There are several ways in which structural disorder can be introduced. Although direct simulation of collision cascades gives detailed information about the nature of the damage, producing completely disordered structures by multiple cascade overlaps is not practical, especially for realistic high-energy events and large system sizes [72]. In amorphous solid, atoms is not randomly distributed in the system, which still maintain certain short range order, thus

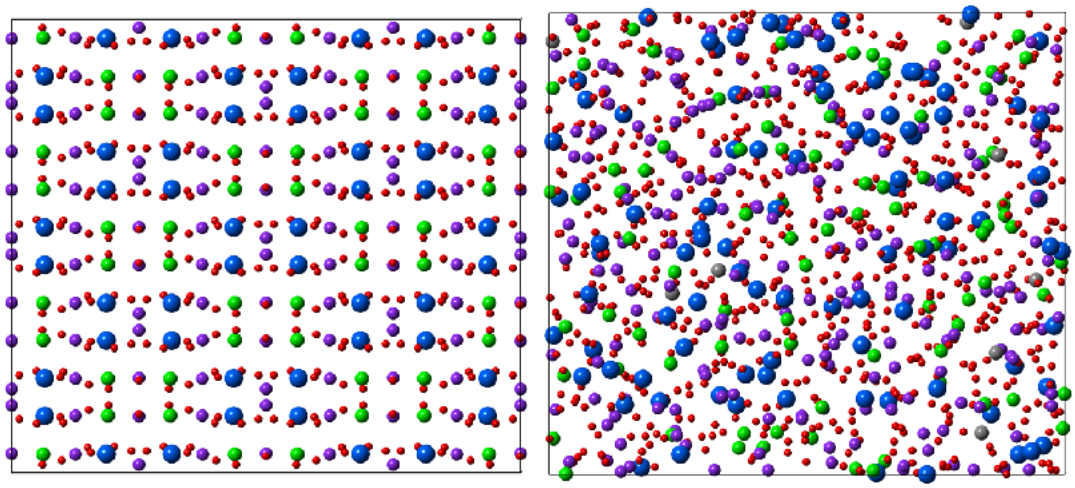

Figure 3.2: Structure of crystalline (left) and amorphous (right) zirconolite. Ca is coloured in blue, Ti is coloured in purple, Zr is coloured in green, U is coloured in grey and O is coloured in red.

I follow a procedure which is similar to the annealing process. I prepared the amorphous structures by first melting the system at 5000 K, equilibrating the high-temperature liquid for 100 ps and subsequently quenched the liquid slowly to room temperature, 300 K. I note that amorphization by quenching the liquid can be different from radiation-induced amorphization in several respects [59, 60, 73, 74], however my main motivation is to address a fundamental question of how diffusion is affected by topological disorder in general.

I use DL_POLY MD simulation package [44] and the system of 1056 atoms with the recent interatomic potential fitted to zirconolite properties [75]. To achieve the metastable amorphous state, I equilibrated all structures at 2000 K, then decrease the temperature to 300 K with a rate 2 K/ps to make the equilibration as slow as possible in MD simulations. The equilibration is simulated in NPT ensemble and the diffusion is simulated in NVE ensemble. The timestep is set as 0.001 ps. I have simulated and relaxed three different zirconolite structures: crystalline, high-density amorphous with density equal to the crystal and low-density amorphous zirconolite with 5% decreased density as

Table 3.1: Buckingham parameters and the charge of O, Ca, Zr, Ti and U in this study.

	A (eV)	ρ (Å)	C (eV· Å)	Charge (|e|)
O–O	22764	0.1490	32.8	-2
Ca–O	584.187	0.3460	0.0	2
Zr–O	1547.795	0.3470	0.0	4
Ti–O	1244.016	0.3510	0.0	4
U–O	1761.755	0.3564	0.0	4

in the experimental samples damaged by the radiation damage [36, 76]. 10% of U atoms were introduced as a substitution for Zr atom, representing a typical waste load in waste forms. The position of Zr atoms was chosen manually. The structure of crystalline and amorphous zirconolite has shown in Fig. 3.2. The interatomic potential for the U–O interaction was taken from Ref. [77]. The parameter of interaction potential in this study are listed in Table 3.1.

Experiments on alteration of damaged waste forms are conducted at high temperature in order to observe alteration and diffusion during laboratory time scale [57–60, 63, 64, 76]. Similarly, I performed several MD simulations at temperature high enough to observe diffusion. Diffusion was observed as the linear time dependence of the mean square displacement, $\langle r^2 \rangle = 6Dt$, where D is the diffusion coefficient. The coefficient 6 depend on the dimension of the system.

3.3 Results

In Fig. 3.3, I show representative $\langle r^2 \rangle$ calculated for crystalline and amorphous zirconolite. I note that at short time, $\langle r^2 \rangle$ crosses over from the oscillatory to the diffusive regime, acquiring the linear time dependence characteristic of diffusion (see Fig. 3.3–3.4). I perform subsequent analysis on the basis of the linear $\langle r^2 \rangle \propto t$ diffusive regime at long times. I limit the analysis to 5 ns

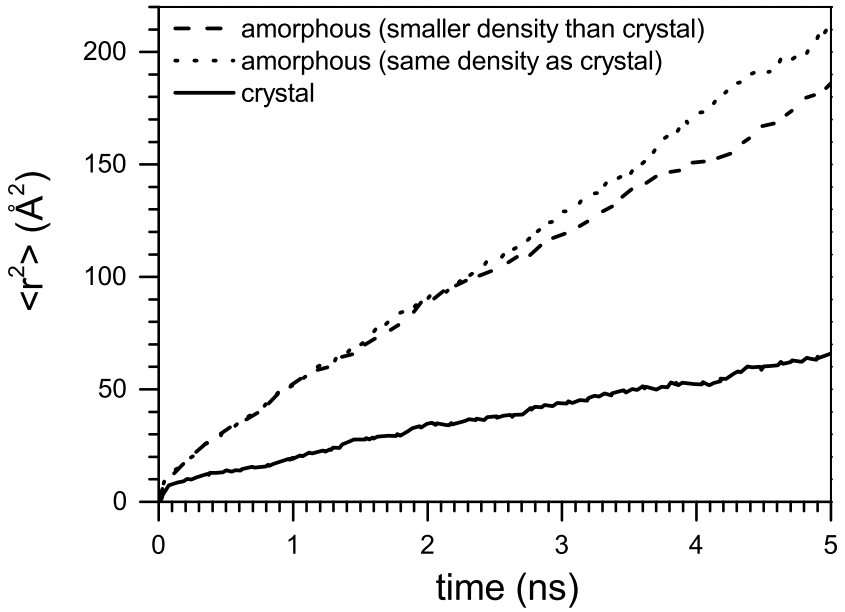

Figure 3.3: Mean-squared displacement of O ions (averaged over all ions) in crystalline and amorphous zirconolites of two different densities at 2000 K.

in time since at longer times at high temperature I observe the signatures of recrystallisation, witnessed by the appearance of peaks in Zr–Zr and Ti–Ti sublattices beyond the medium-range order.

In the following analysis, I will use two equations for the temperature dependence of the diffusion coefficient D and hopping time τ, the average time between two consecutive atomic jumps at one point in space [2]:

$$D = D_0 \exp\left(-\frac{U}{T}\right) \tag{3.2}$$

$$\tau = \tau_D \exp\left(\frac{U}{T}\right) \tag{3.3}$$

where U is the activation barrier for the diffusion event, τ_D is the shortest (Debye) vibration period of about 0.1 ps, the pre-factor D_0 is the high-temperature

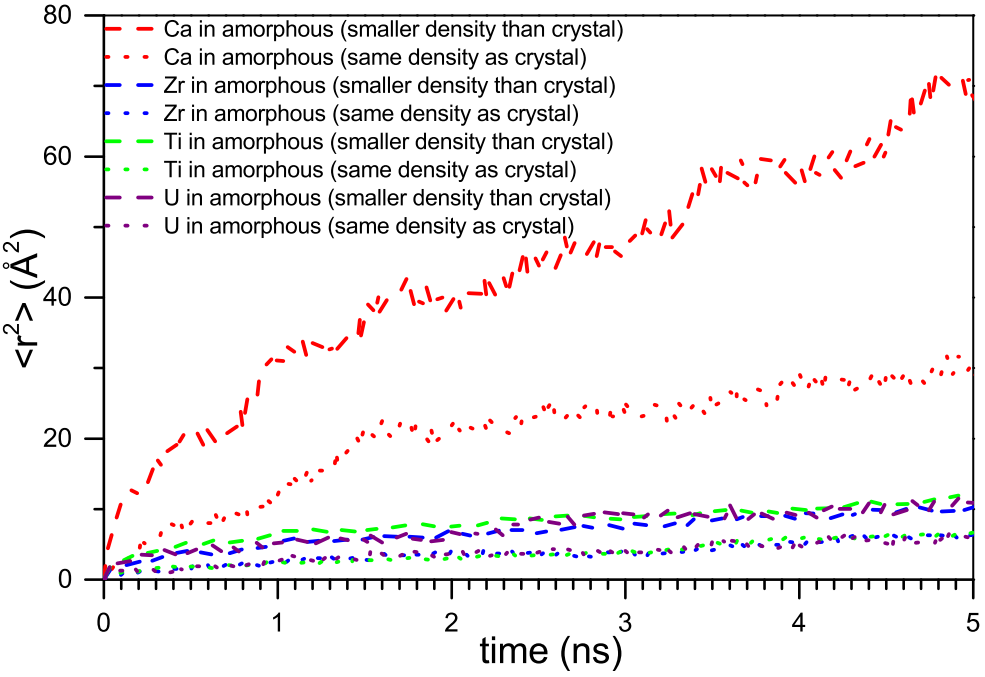

Figure 3.4: Mean-squared displacement of Zr, Ti, Ca and U ions (averaged over all ions) in amorphous zirconolites of two different densities at 2000 K.

limit of the diffusion coefficient when $\tau \to \tau_{\mathrm{D}}$ and $k_{\mathrm{B}} = 1$.

Apart from O ions, I observe no diffusion in the crystalline systems on the time scale of my MD simulations. On the other hand, I observe the diffusion of all ions in the amorphous systems at the same temperature (see Fig. 3.3–3.4). Importantly, this includes the diffusion in amorphous structures of the same density as the parent crystal. I therefore find that structural disorder at the same density increases the diffusion constant profoundly, an unexpected finding since the early work [2], it was density which was believed to govern the activation energy barrier for diffusion [67]. This represents the first main result of this study.

I next calculated main parameters of diffusion, U and D_0, in amorphous systems and their change due to different density. I calculate U by fitting the data in Fig. 3.5 to Eq. (3.2) as $\ln D = \ln D_0 - \frac{U}{T}$, and show the results

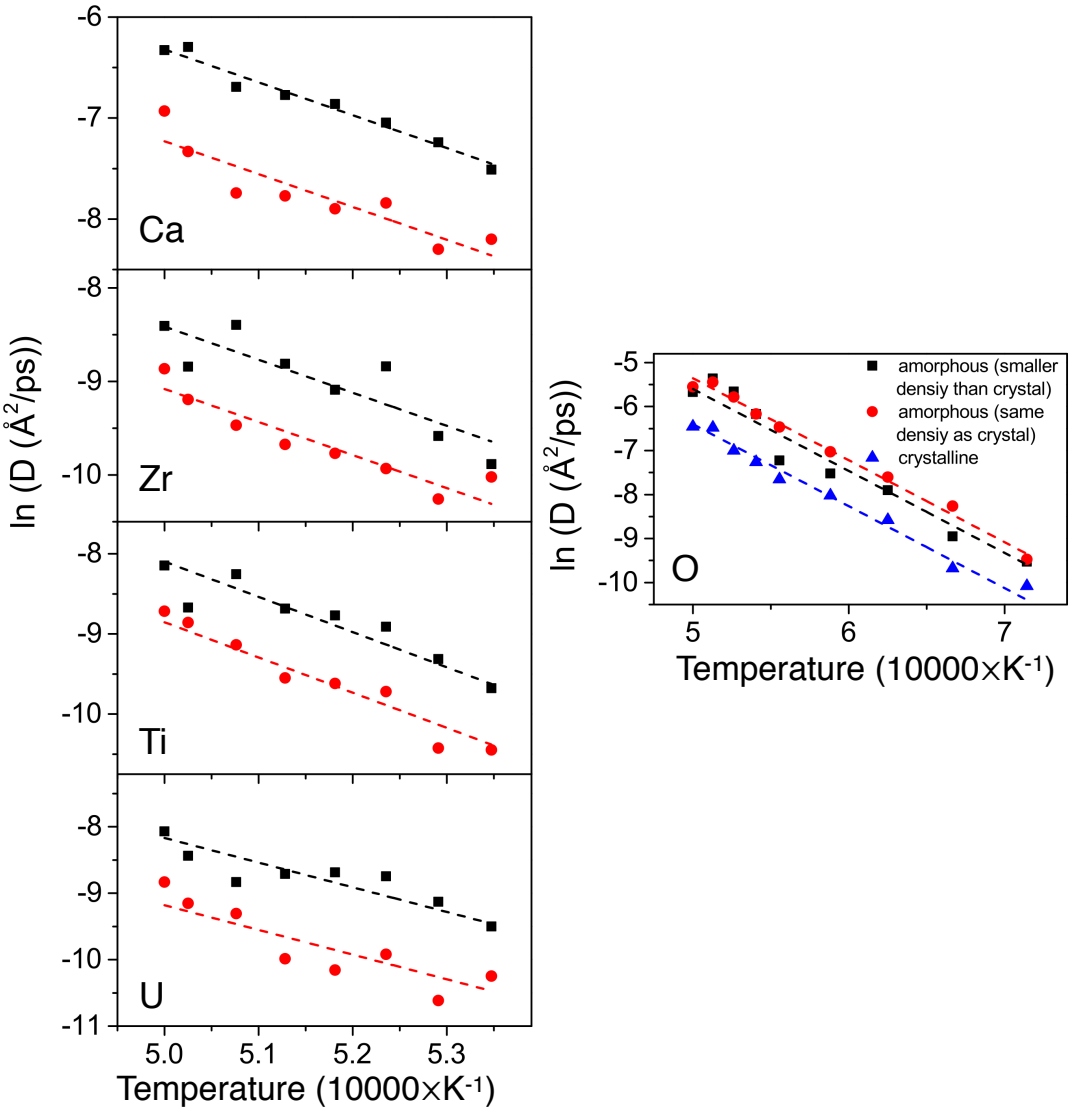

Figure 3.5: $\ln(D)$ vs inverse temperature, $\frac{1}{T}$ for different atomic species. The range of temperatures in the x-axis is 1400–2000 K for O and 1870–2000 K for cation. The dashed lines are fits of both sets of points to the straight lines assuming that the slopes are the same within the errors present.

Table 3.2: Activation energy U (eV) of atomic species in the crystalline and amorphous zirconolite at two different densities. Pre-factors D_0 (m^2/s) are denoted as D_{01} (amorphous system at larger crystalline density), D_{02} (amorphous system at smaller density) and $D_{crystal}$ (pre-factor of diffusion of O ions in the crystal). The change of diffusion pre-factors is evaluated using two methods discussed in the text: calculating D_0 from direct fitting to calculated D (a) and estimating the range of D_0 at different temperature (b). Subscripts 1 and 2 refer to amorphous systems at larger (crystalline) and smaller density, respectively.

	Ca	Zr	Ti	U	O
U (amorphous, same density as crystal)	2.80 ± 0.53	3.05 ± 0.73	3.79 ± 0.63	3.20 ± 0.86	1.61 ± 0.06
U(amorphous, smaller density)	2.80 ± 0.20	3.05 ± 0.71	3.79 ± 0.55	3.20 ± 0.54	1.61 ± 0.15
U (crystal)					1.61 ± 0.07
(a)					
$\ln \frac{D_{02}}{D_{01}}$	0.91 ± 0.09	0.66 ± 0.15	0.76 ± 0.13	1.01 ± 0.18	0.0 ± 0.2
$\ln \frac{D_{01}}{D_{crystal}}$					1.04 ± 0.1
(b)					
$\ln \frac{D_{02}}{D_{01}}$	$0.89 - 0.92$	$0.62 - 0.71$	$0.54 - 1.00$	$0.79 - 1.27$	
$\ln \frac{D_{01}}{D_{crystal}}$					$0.94 - 1.11$

in Table 3.2. Since I observe no appreciable differences of slope between amorphous structures of different densities, the slopes were assumed to be same within the errors of the fitting. The calculated values of U in amorphous zirconolite represent our next quantitative result enabling future prediction of how diffusion in the waste form will operate during long time scales, as discussed below in more detail.

In Table 3.2, the scatter of errors is related to large fluctuations in the system at very high temperature I simulated, and is larger for the less numerous U ions. I therefore find that the considered moderate density decrease, corresponding to the experimental swelling of radiation-damaged zirconolite [36, 76], does not have a significant effect on U.

Since I do not observe diffusion in the crystalline zirconolite apart from O ions, I am unable to calculate U in the crystal and compare it to the amorphous system. However, I can estimate the lower bound of U in the crystal, U_l, using Eq. (3.3): $U_l = T_h \ln \frac{\tau_l}{\tau_D}$, where τ_l is the longest simulation time and T_h is the highest temperature simulated in the crystal. Taking $T_l = 2100$ K and $\tau_l = 130$ ns, I find U_l of about 3 eV. U_l is therefore of the same order of magnitude as typical U in crystals (typical U in crystals can be larger by up to about a factor of 2 for different ions).

A discernible trend in Fig. 3.5 is the increase of pre-factor D_0 at smaller density. I estimate this increase using two methods. First, I directly calculate the increase of D_0 by fitting the MD data to $\ln D = \ln D_0 - \frac{U}{T}$. This gives $\frac{D_{02}}{D_{01}}$ in the range $2-3$ for different ions, where subscripts 1 and 2 refer to amorphous systems at larger (crystalline) and smaller density, respectively (see Table 3.2). Second, the range of $\frac{D_{02}}{D_{01}}$ can be estimated by subtracting $\ln D_1 = \ln D_{01} - \frac{U_1}{T}$ and $\ln D_2 = \ln D_{02} - \frac{U_2}{T}$. Using my earlier result that U are the same within the error, I find $\ln \frac{D_{02}}{D_{01}} = \ln \frac{D_2}{D_1}$. Then, the range of $\ln \frac{D_{01}}{D_{02}}$ is found by calculating $\ln \frac{D_2}{D_1}$ at low and high temperature in Fig. 3.5, giving $\frac{D_{02}}{D_{01}}$ in the range similar to the first method, as follows from Table 3.2. I therefore find that the increase of diffusion pre-factors with system's volume is appreciable.

The results show an interesting heterogeneity of atomic species in terms of diffusion. As mentioned above, O ions stand out from the rest of ionic species in that their diffusion is seen in the crystalline zirconolite, because the nature O "vacancies" exist in $CaZrTi_2O_7$. $CaZrTi_2O_7$ is based on fluorite structure. Because the formal charge of Ca is +2 and O is -2, some of O sites need to be vacant for charge balance, which cause high diffusivity. Furthermore, O ions do not show discernible decrease of U as a result of amorphization and density decrease. However, I observe the increase of D_0 as a result of amorphization

by the factor of about 3. Contrary to other ions, however, this factor is not sensitive to density decrease (see Fig. 3.5 and Table 3.2). Ca also shows much higher diffusivity than other cation in amorphous zirconolite. The reason for the difference is that the Ca-O bond is more ionic than other cation-O bond in the system.

3.4 Discussion and summary

There are several important insights from this study. First, I find that structural disorder and amorphization in particular, introduced to the system at the *same* density as the parent crystal, can result in a profound increase of solid-state diffusion. This is an interesting general insight in view that both earlier and current theories emphasise density as the main factor controlling the diffusion [2, 67]. This implies that the net effect of the appearance of slower and faster local diffusion pathways in the disordered structure (see Fig. 3.1) is the increase of diffusion.

According to this result, faster local diffusion pathways dominate over slower ones in the same-density disordered structure. This is analogous to the well-known case of introducing equal amounts of harder and softer inclusions in an elastic matrix, with the result that the overall elastic response is mostly governed by the softer phase (in a simple example, this is illustrated by the inverse sum rule for bulk or shear moduli). The analogy is further relevant here because lower-density faster diffusion pathways and higher-density slower pathways can be approximately viewed as local regions that are softer and harder, respectively (see Fig. 3.1). Then, the net effect is elastic softening of the system and hence smaller G, in agreement with experimental results [68]. This implies smaller U according to Eq. (3.1) and hence larger D according to Eq.

(3.2), consistent with my findings.

I note here that contrary to the role of density which is well understood and quantified, the effect of disorder at constant-density is not amenable to a simple treatment or a model, but is important in a wider context of understanding the essential differences between crystalline and amorphous systems. For example, it has been long thought that amorphous systems are notably different in terms of their vibrational spectra, yet recent evidence has found that this is not the case if the amorphous system is at the same density [70]. This is consistent with a wider picture emerging that many important thermodynamic properties of the system are insensitive to disorder due to the similarity of their spectra whereas other properties, namely the transport properties such as thermal conductivity, are strongly affected [71].

Second, the increase of diffusion due to amorphization is important for the operation of waste forms. For example, under the typical waste load zirconolite will become amorphous from irradiation after about 1000 years. Being a very small fraction of time of operation of the waste form (100,000-1,000,000 years), this implies that solid-state diffusion will take place almost entirely in the amorphous state. This will take place with the associated increased diffusion constants that I have found in this work. Our results, and the calculated values of U in particular, can therefore be used to predict the solid-state diffusion in the waste form during the most important period of its operation.

Third, I have found specifically that the combined effect of amorphization and volume increase can affect both the activation energy and diffusion pre-factors, but that different ionic species can be differently affected. For example, the diffusion of most numerous and mobile O ions is not affected by amorphization to the same extent as in other ionic species.

3.5 Conclusions

In summary, by using MD simulations I have disentangled the effects of amorphization and density on solid-state diffusion, and showed that contrary to existing theories, a profound increase of diffusion takes place as a result of amorphization at the same density. I have found that increasing the volume in the amorphous system increases the pre-factors of diffusion constants. I have also found that atomic species in zirconolite are affected differently by amorphization and density change. Our microscopic insights are relevant for understanding how solid-state diffusion changes due to disorder and for constructing predictive physics-based models aimed at predicting the performance of waste forms over long time scales.

Chapter 4

Microstructure and Oxygen Diffusion in Yttrium-stabilised Cubic Zirconia

In this chapter I discuss, characterise and quantify the microstructure of $Zr_{1-x}Y_xO_{2-x/2}$. By combining the DL_POLY code and the ARCHER supercomputer mentioned in the previous section, the system size could be extended up to 4,116,000 atoms in my MD simulation. For the fist time microstructure transformation of Y-doped ZrO_2 is able to be captured by simulation due to the very large sample size. I observe that microstructures transform during monoclinic to cubic transition in Y-doped Zirconia. During the transition, the system contains microstructures with two coexisting phases. Although I do not observe a metastable tetragonal phase in my simulations, there is a clear phase transition around 10% of Y. Furthermore, I find that changes of the the microstructure can have a big impact on O diffusion. Thus it is essential to include microstructure effect when analysing O diffusion in Y-stabilised zirconia.

4.1 Introduction

Zirconia (ZrO_2) is an important industrial material. Owing to high oxygen ion conductivity, it finds many applications, for example in oxygen sensors, solid-oxide fuel cells and catalytic sensors. These applications are for the cubic phase of ZrO_2, which can be made by doping the structure with high concentrations of Yttrium. Since the formal charge of Y is +3 and Zr is +4, to preserve charge balance oxygen is removed when Zr is replaced by Y, allowing high oxygen diffusion [78–80].

There have been a lot of studies focused on the phase stability of Y-doped ZrO_2 [78, 79, 81–84]. At room temperature, the crystal structure of pure ZrO_2 is monoclinic. The structure transforms to the phase of tetragonal symmetry at 1170 °C and the phase of cubic symmetry at 2370 °C. However, ZrO_2 also forms a stable cubic phase by doping with a high concentration of divalent or trivalent cations and a metastable tetragonal phase with a low concentration of divalent or trivalent cations at room temperature. The metastable tetragonal structure slowly transforms to the stable monoclinic structure at low temperature ($\sim$ 400 K). Chevalier et al. [78] collected a wide range of data for both the metastable and stable phase diagram of Y-doped ZrO_2. In the metastable phase diagram, there is a metastable tetragonal phase existing for concentrations of Y between 8–18% at room temperature. In the stable phase diagram, ZrO_2 forms cubic phase when the concentration of Y reaches 20% at room temperature.

Experimentally, both Kim et. al [84] and García-Martín et. al [83] observed the domains of different phases coexisting in ZrO_2 with 3.2% and 8% of Y_2O_3 by transmission electron microscopy. However, the challenge of experimental study on these microstructures is that Y could be unevenly distributed in the material due to low cation diffusion, so cubic structures tend to form in high

Y-concentrated region [79]. Since microstructure also plays an important role in the diffusion, it is essential to study how microstructure emerges and evolves in detail.

There are a small number of simulation studies focusing on the microstructure during the phase transformation. Most of these were based on rather small system size, which means it would be impossible to include the emerging microstructure [85–87]. The studies included microstructure created artificial grain by Voronoi tessellation method[88]. It is important to study the changes of microstructure of Y-doped ZrO_2 formed "naturally" using MD simulations with very large sample size.

There are numerous diffusion studies on Y-stabilised ZrO_2, since most of its applications are based on the diffusion property. Most experimental studies show that the activation energy of O exhibits an almost linear correlation with concentration of Y [89–94]. Interestingly, the activation energy of O diffusion also changes with temperature [91, 92, 95]. The reason for this phenomenon is still unclear. In comparison, the results of simulation studies show a more complicated and unclear trend with concentration of Y [89, 90, 96, 97], but these studies can not include the microstructure effect on oxygen diffusion.

In this study, I aim to develop a model that can simulate the microstructure transformation during the monoclinic–cubic transition of Y-stablised ZrO_2. I performed extensive MD simulations for ZrO_2 in a wide range of concentration of Y. The system size was extended up to 360 Å of the supercell size. Then I quantify the emergent microstructures and observe a phase transition around 10% of Y. Finally, I explain how those microstructure change can affect O diffusion.

4.2 Methods

4.2.1 ZrO_2 potential

In collaboration with my supervisor Prof. Martin Dove, we developed a new model for ZrO_2 based on Buckingham potential which is shown in Table 4.1. The parameter was fitted using GULP [56]. The potential is fitted based on the properties of monoclinic, cubic and tetragonal phase of ZrO_2, crystalline Y_2O_3 and cubic $Zr_{0.786}Y_{0.214}O_{1.893}$. We fitted the parameters in the model interatomic potential against the energies from DFT calculation [98], crystal structure and elastic constant from experiment data [99] using GULP for developing empirical potentials.

The comparison of elastic constants between this model, other models and experimental result are listed in Table 4.2. It can be seen that our model gives better result for Y-stabilised cubic phase, and Schelling's model gives better result for the tetragonal phase. Although, similarly to other ZrO_2 studies based on empirical potentials, our model suffers the problem that the structure of ZrO_2 prefers to form the orthorhombic phase which is more symmetrical than monoclinic phase, my model provides the correct order of energetic characteristics and reasonable elastic constants. In this study, I use the orthorhombic phase to discuss the main effects of microstructure and its evolution.

4.2.2 Details of molecular dynamics simulations

Cubic pure ZrO_2 was chosen as initial structure. To obtain the right composition of the Y-doped ZrO_2, randomly chosen Zr atoms are replaced by Y, then randomly-selected O are removed from system to ensure the charge balance. These work was done by the data2config which is written by my

Table 4.1: Fitted Buckingham parameters and the charge of O, Zr and Y for ZrO_2. This potential is obtained based on fitting to the properties of monoclinic, cubic and tetragonal phase of ZrO_2, crystalline Y_2O_3 and cubic $Zr_{0.786}Y_{0.214}O_{1.893}$. The properties include structures and elastic constants from experimental data [99], and energies from DFT calculation [98].

	A (eV)	ρ (Å)	C (eV· Å)	Charge (|e|)
O–O	1071	0.3623	175	-1.2
Zr–O	7375	0.2265	0.0	2.4
Y–O	181110	0.1726	0.0	1.8

Table 4.2: Comparison of elastic constants (GPa) for ZrO_2 by using our model, Schelling's model [87] and experiment result [99].

	Our model	Schelling model	Experiment
C_{11}(cubic)	391	664	402
C_{12}(cubic)	69	104	95
C_{44}(cubic)	68	98	56
C_{11}(tetragonal)	276	523	451
C_{12}(tetragonal)	159	270	240
C_{44}(tetragonal)	9	58	39

supervisor Martin Dove. Then MD simulation is performed using DL_POLY [44] to simulate the structure and O diffusion for Y-stabilised ZrO_2 with 0–25% of Yttrium with the system size that consist 96,000–4,116,000 atoms with cell size 100–360 Å. Similarly to the previous chapter, I equilibrated all structures at 2000 K, then decrease the temperature to 300 K with a rate 2 K/ps to make the equilibration as slow as possible in MD simulations. The equilibration is performed in NST ensemble which allow the both volume and shape of the simulation box change during the simulation. The oxygen diffusion is performed in NVE ensemble for 100 ps. The timestep is set as 0.001 ps. I ran the simulation on up to 1500 cores for 20 hours on the ARCHER national supercomputer.

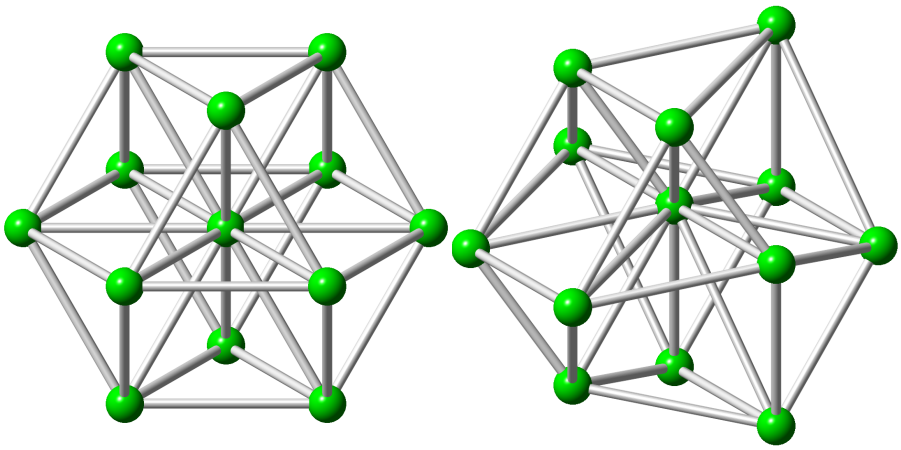

Figure 4.1: Cation and its coordination cation for cubic (left) and orthorhombic phase(right).

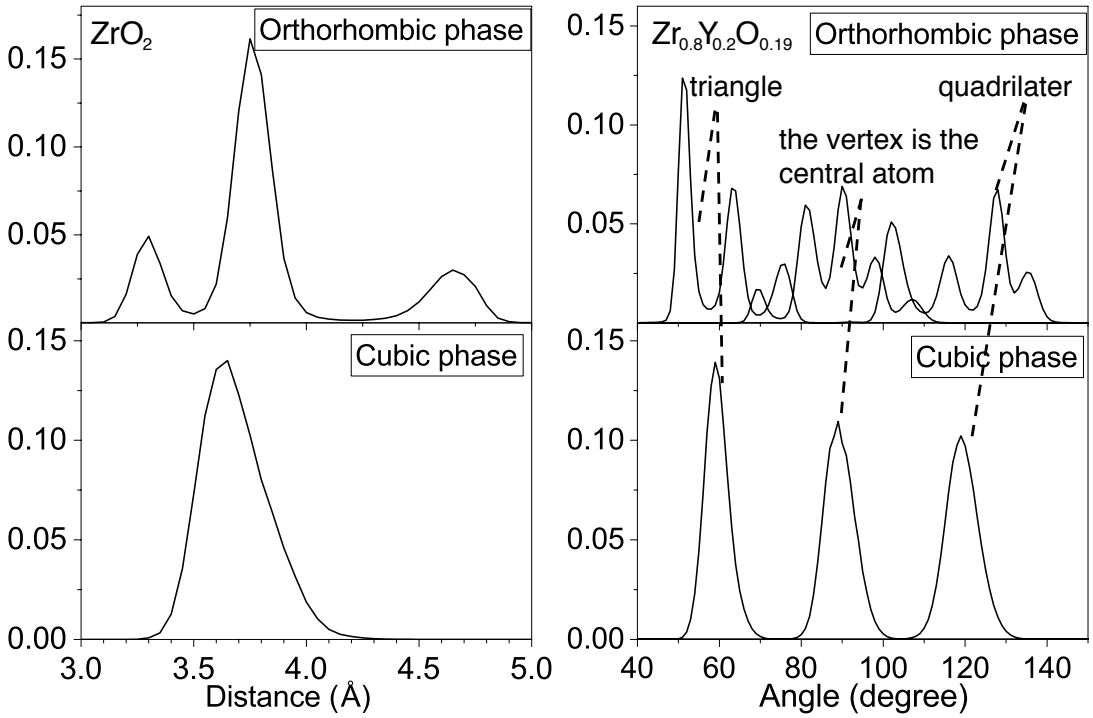

Figure 4.2: Cation-cation distance and angle distribution of dodecahedrons for cubic (left) and orthorhombic phase(right). The angle distribution is divided in three scenarios: (a) the vertex is denoted by the central atom; (b) angles form the triangle of the dodecahedra; (c) angles form the quadrilater of the dodecahedra.

4.2.3 Cation coordination

To separate different phases in the system, I assign each cation to a corresponding phase by analysing its coordination. I search the nearest cations for the selected cation. The selected cation and its coordinations form a dodecahedron. The dodecahedrons are shown in Fig. 4.1, featuring different shape for cubic and orthorhombic phase, respectively. The angle and distance distribution of those dodecahedrons determine which phase the selected cation is in. I wrote a code to analyse the angle and distance distribution of dodecahedrons using Fortran 90. Fig. 4.2 shows the angle and distance distribution calculated from pure ZrO_2 and $Zr_{0.8}Y_{0.2}O_{1.9}$, respectively. These are used as a baseline for separating the two phases shown in Fig. 4.1. During the analysis of dodecahedrons, the code calculates distances and angles for each dodecahedrons and then checks if the distribution fits the distribution of each peak in the baseline. In the situation that the peak of angle distribution is not well defined in the orthorhombic structure, the distribution is divided in three scenarios: (a) the vertex is denoted by the central atom; (b) angles form the triangle of the dodecahedra; (c) angles form the quadrilateral of the dodecahedra.

4.3 Results and discussion

4.3.1 Microstructure transforming in Y-stabilised Cubic Zirconia

Phase transition of ZrO_2 caused by doping with Y

Fig. 4.3 shows that microstructures transform in domains with increasing concentration of Y. The system without Y forms the orthorhombic phase with different orientations, but I can still observe a small amount of cubic phase existing in the grain boundary between orthorhombic grains. When the concentration of Y reaches 20%, the system transforms to the cubic structure.

Between 0–20%, both cubic and orthorhombic phases coexist in the system, and the concentration of the cubic phase increases with the concentration of Y. Similar microstructure was also observed in experimental studies [83].

It is necessary to simulate these microstructures in a very large system, because the simulated structure, in the periodic system, can be affected by the shape of the supercell. This effect reduce with the supercell increase. In Fig. 4.4, at low concentration of Y, most of the crystalline structure aligns to a specific orientation in the ZrO_2 system consisting of 864,000 cations with the cell size around 310 Å, but that phenomenon does not appear in the $Zr_{1-x}Y_xO_{2-x/2}$ system consisting of 1,372,000 cations with the cell size of about 360 Å. This indicates that the simulation can still be affected by the constraint provided by the supercell size up to 360 Å.

Since Y is randomly distributed in the system, I can study the relationship between the formation of the cubic phase and the local concentration of Y atoms. In Fig. 4.5, I plot the proportion of Y in the cubic cluster. As can be seen in Fig. 4.5, before the structure completely transforms to the cubic phase, the concentration of Y in the cubic domain is around 25% higher than the concentration Y in the system. This confirms that the cubic phase domains prefer to form in high-Y concentration region.

To quantify this transform, I calculated the concentration of cations in the cubic phase with 4 different system sizes shown in Fig. 4.6. It seems that there is a large fluctuation in the system consisting of $Zr_{1-x}Y_xO_{2-x/2}$ with 32,000 cations and a cell size around 105 Å, but the result becomes more consistent in the larger system size. For the concentration of Y between 0–9%, there is only a small amount of cubic structures growing inside the grain boundary. After around 10% of Y, there is a rapid increase of cubic phase. The cubic phase

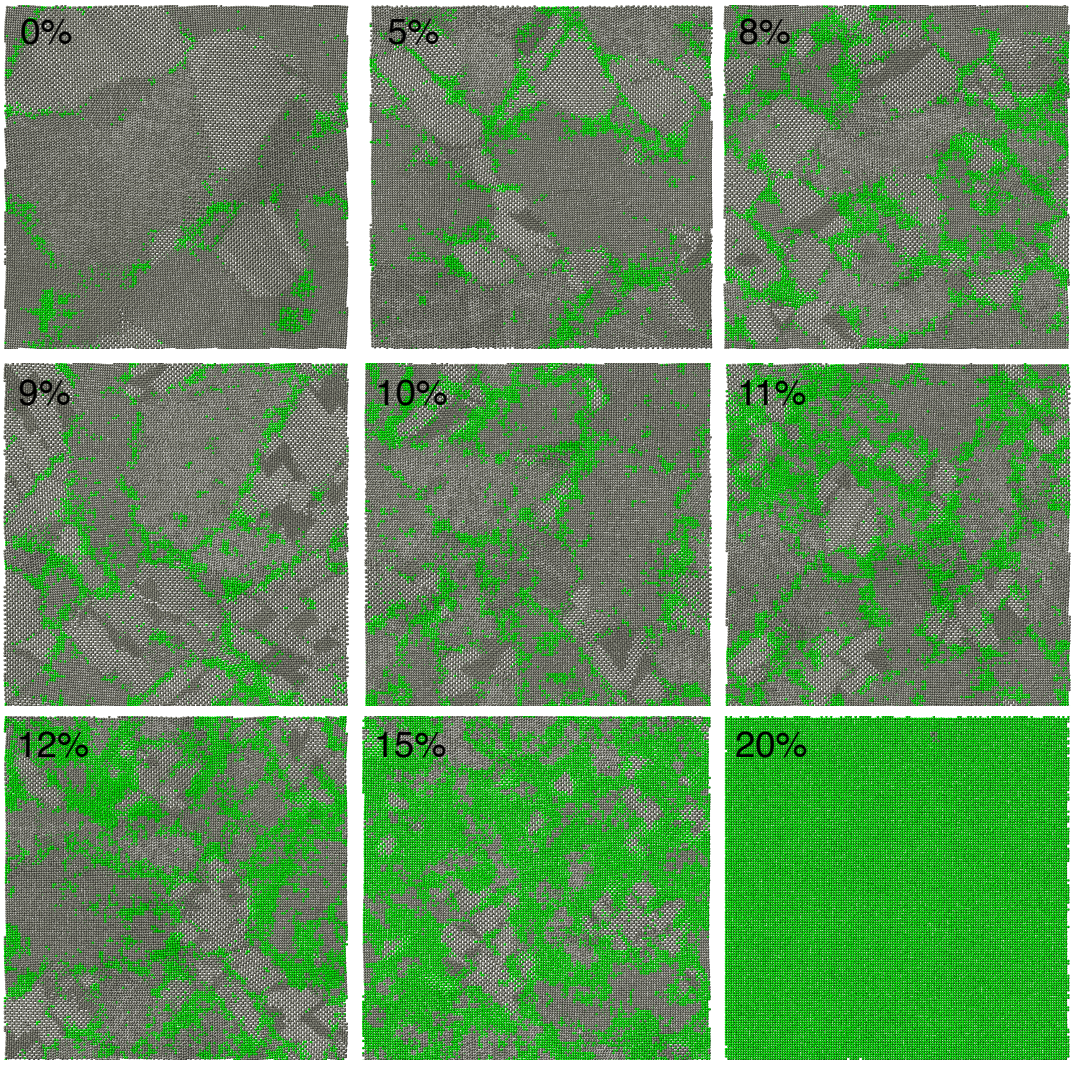

Figure 4.3: Microstructure of the cubic phase (green) coexisting with the orthorhombic phase at different concentrations of Y in the formula with 1,372,000 cations and cell size around 360 Å. I only show cations in the structure. The cubic phase is seen to grow in the system with increasing concentration of Y.

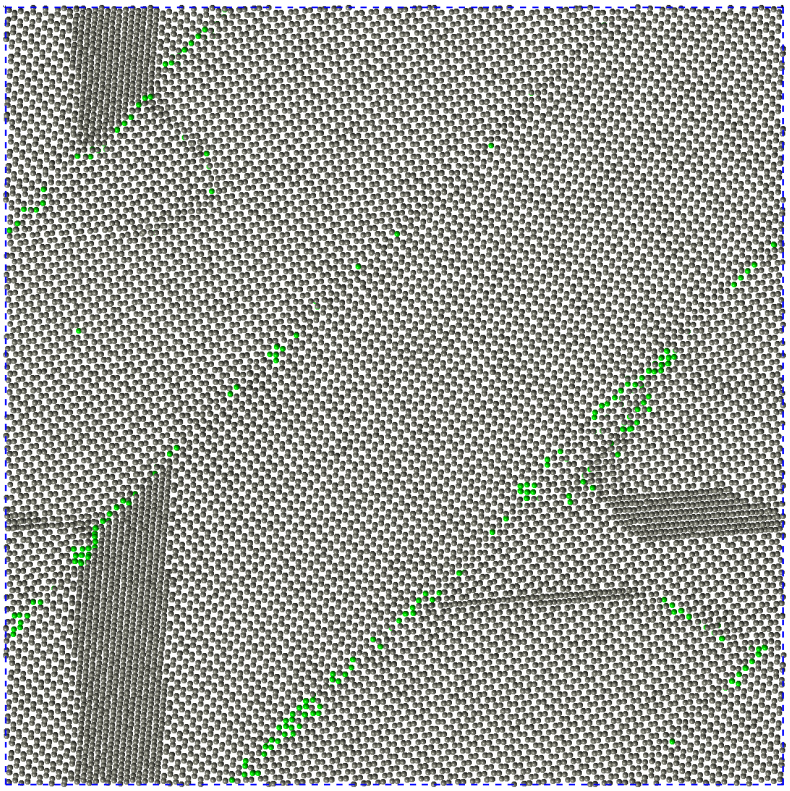

Figure 4.4: Microstructure of the cubic phase (green) and orthorhombic phase for ZrO_2 with 864,000 cations and the cell size around 310 Å. The orthorhombic phase align along a specific direction if the system size is too small.

reaches saturation after 18% of Y. Those results indicate that there may be a phase transition at around 10% of Y.

The change of volume also confirms the phase transition around 10% of Y. In Fig. 4.7, I converted the volume to the linear size as $V^{\frac{1}{3}}$. It can seen that the volume increases slightly with the concentration of Y before 10% of Y due to the fact that the ion size of Y is larger than Zr, and then the volume starts to decrease rapidly with Y concentration. After 20%, the volume starts to increase again. The volume of ZrO_2 without Y and with 20% of Y correspond to the volume of orthorhombic and cubic phase of ZrO_2, respectively.

The only phase transition known in the literature is the tetragonal-monoclinic

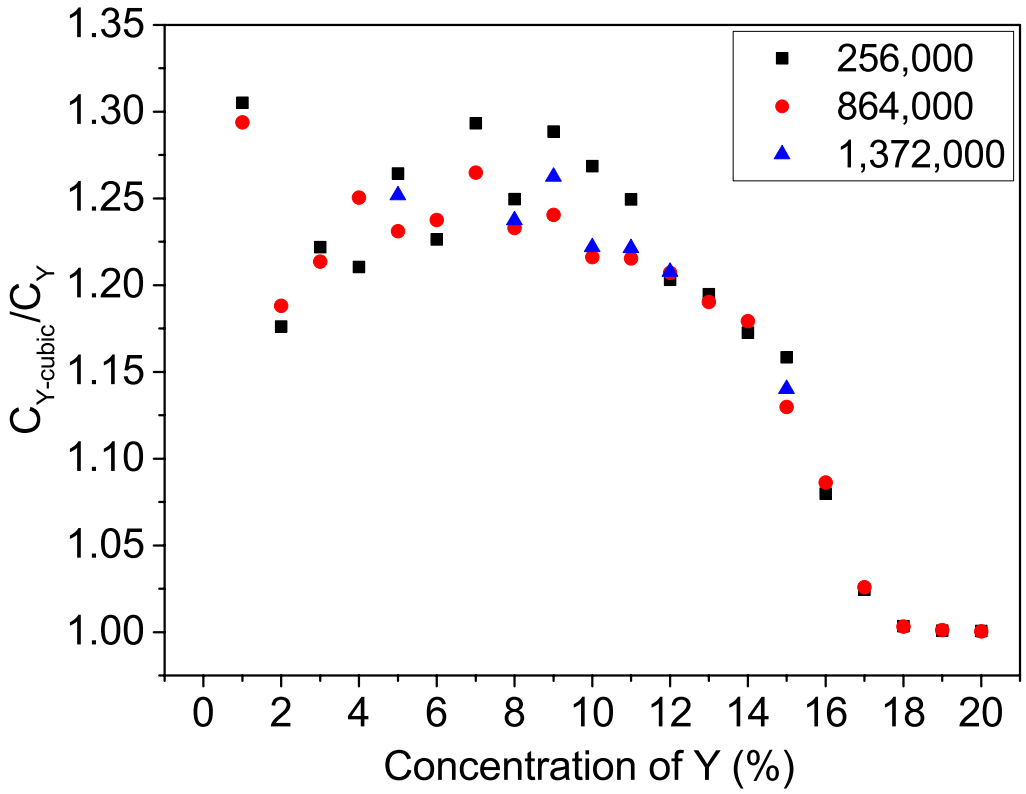

Figure 4.5: Concentration of Y in the cubic domain divided by concentration of Y in the system for different system size.

transition at around 8% of Y on the metastable phase diagram. There might be some connection between this metastable transition and the transition in my simulations.

Grain size changing during the transition

To quantify the grain size, I calculated the correlation function for the cubic phase. I assume that the cation of the cubic phase corresponds to 1 and cation of orthorhombic phase corresponds to 0. Then, the correlation function can be calculated as $g(r) = \langle S(0) \cdot S(r) \rangle$. If atoms at position r is cubic phase, $S(r)$ equals to 1, and if atoms at position r is orthorhombic phase, $S(r)$ equals to 0. It can be seen from Fig. 4.8 that the correlation function decays from 1 to the

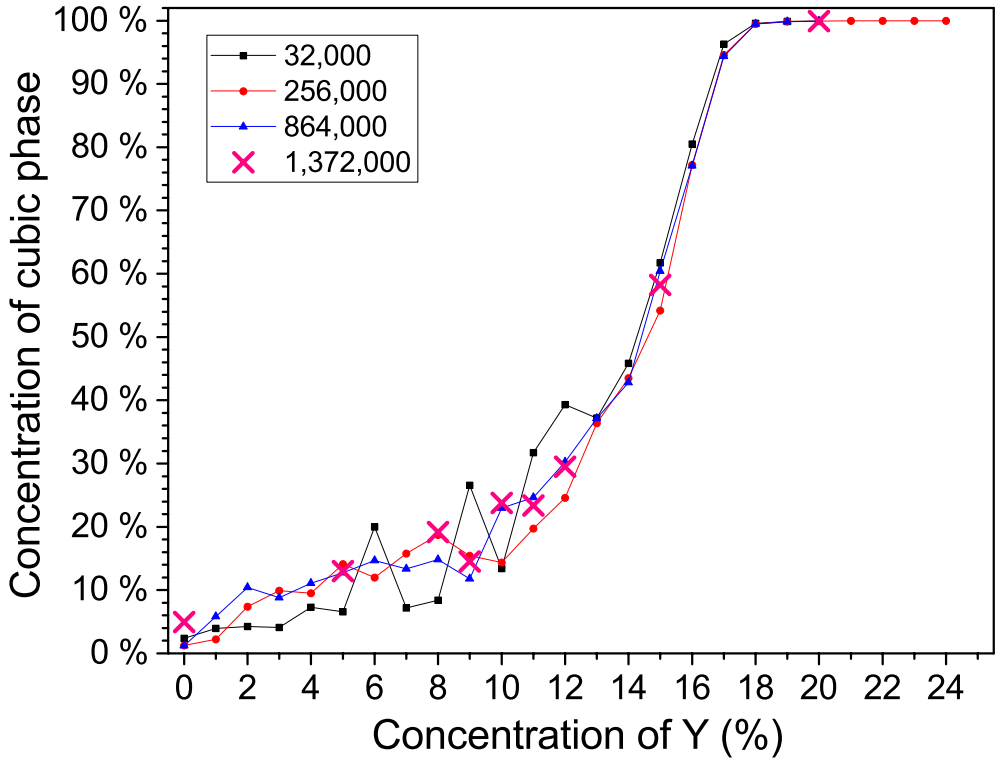

Figure 4.6: Concentration of the cubic phase for different system size vs concentration of Y. Concentration of the cubic phase increase with the concentration of Y.

concentration of cubic phase. The correlation function is fitted by:

$$g(r) = (1 - c)\exp(-r/\xi) + c \tag{4.1}$$

where c is the concentration of cubic phase, and ξ is the correlation length.

To calibrate the relationship between the correlation length and the grain size, I construct artificial cubic boxes with fixed size in the system as shown in Fig. 4.9. I then calculated the correlation function of the artificial boxes to get the correlation length. Since I already knew the cubic size, the relationship between the correlation length and cubic size is plotted in Fig. 4.10. The grain size shown is calculated by scaling the correlation length using the relationship between the size and ξ in Fig. 4.11.

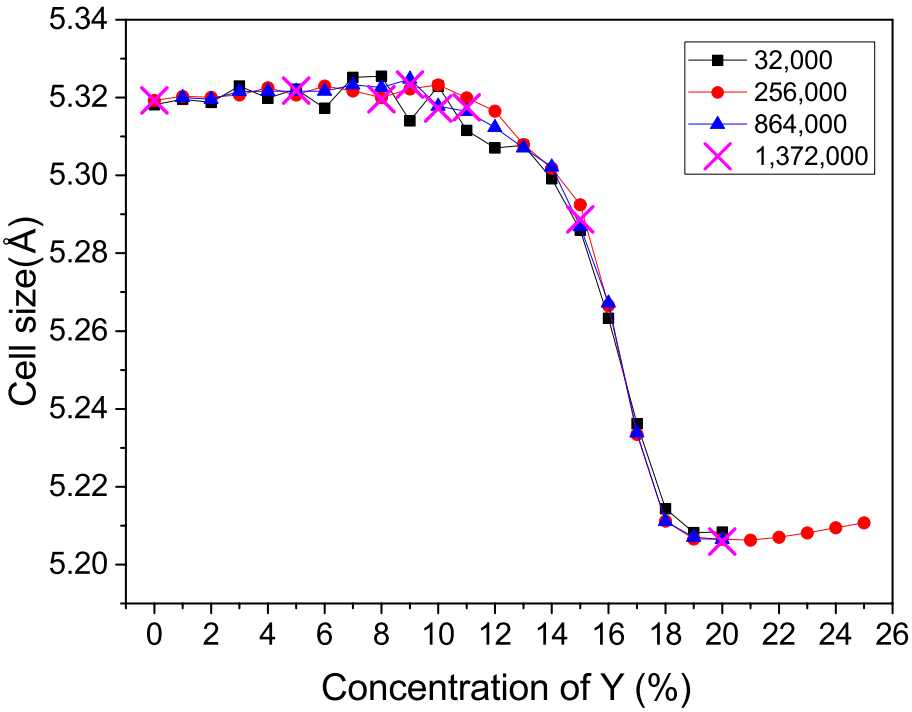

Figure 4.7: Cell size ($V^{\frac{1}{3}}$) for different system size vs concentration of Y. A phase transition occur at around 10% of Y.

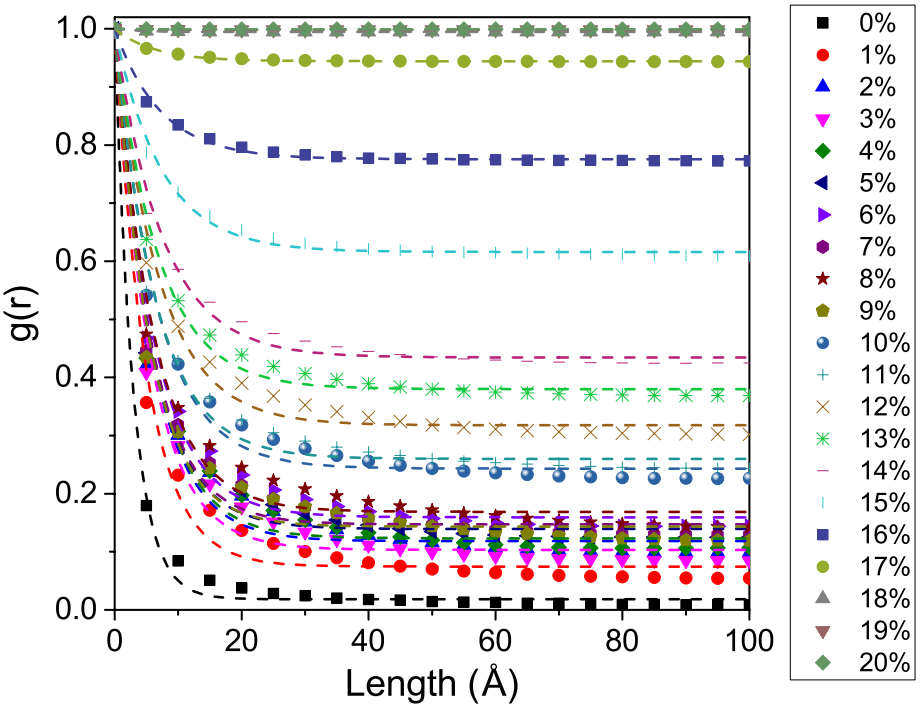

Figure 4.8: Correlation function of the cubic phase of the ZrO_2 with 0% – 20% of Y.

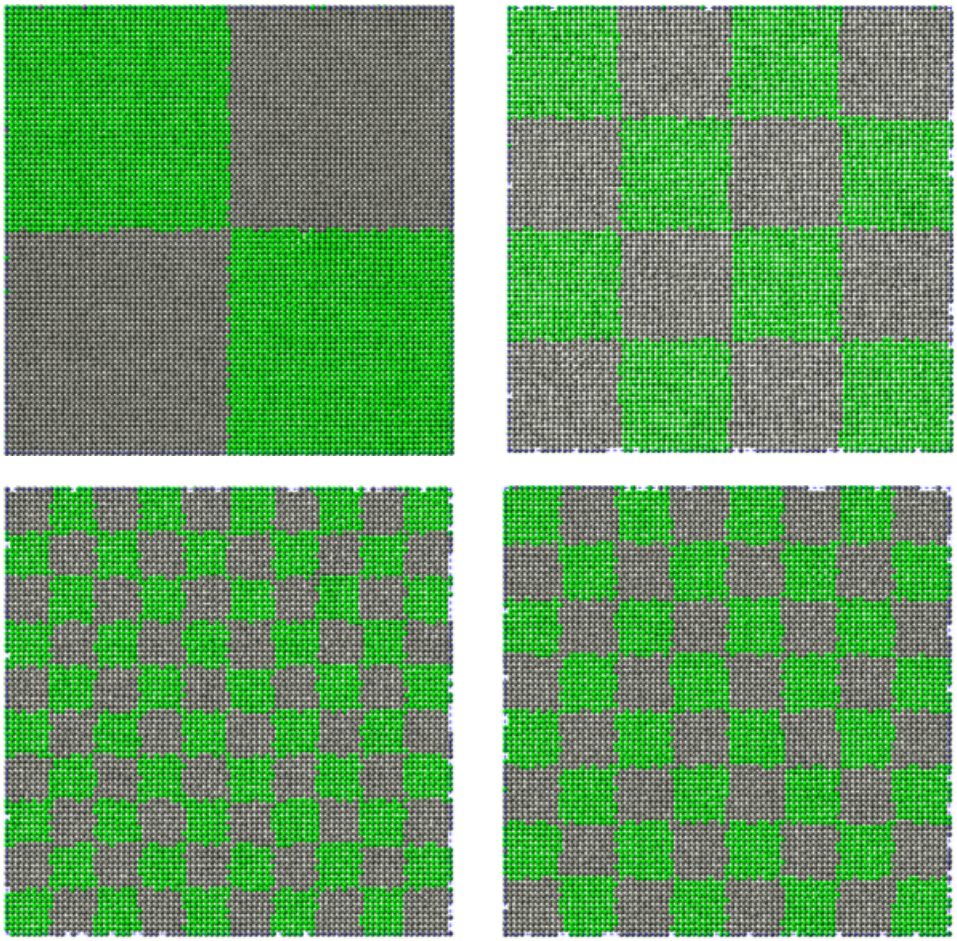

Figure 4.9: Examples of artificial system contain cubic boxes with same size.

Fig. 4.11 shows the grain size of the microstructures. It can be seen that the fluctuation is clearer for the $Zr_{1-x}Y_xO_{2-x/2}$ with 32,000 cations. It is also seen that at low concentration of Y, the microstructure is affected by the simulation size more. This is probably caused by the orthorhombic phase aligning along the same direction at smaller system size shown in Fig. 4.4. When the concentration of Y is above 15%, the grain sizes are in agreement with each other provided the system size is above 256,000 cations. For the $Zr_{1-x}Y_xO_{2-x/2}$ system with 1,372,000 cations, the grain size does not change for low concentration of Y until the phase transition occurs. After the phase transition, the grain size starts to increase again, although this trend is different

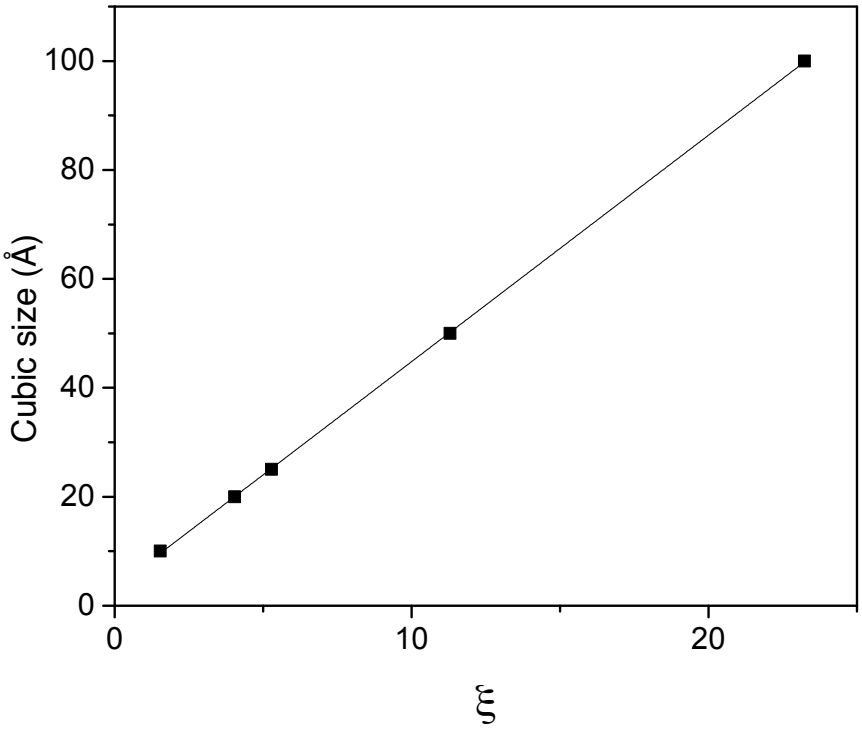

Figure 4.10: Cubic edge length vs correlation parameter ¸. The plot shows linear relationship between cubic edge length vs correlation parameter.

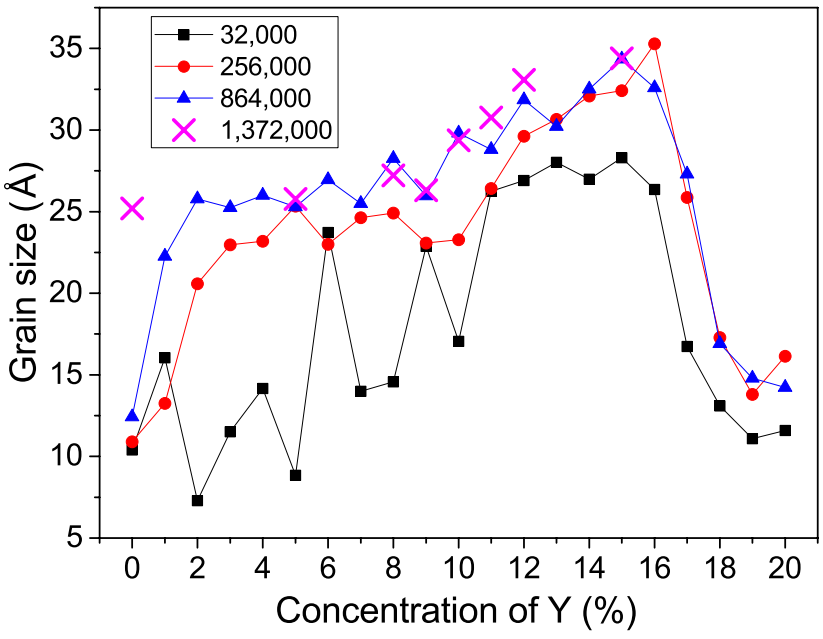

Figure 4.11: Grain size vs concentration of Y for systems with different size.

in the smaller system: the grain size in the smaller system increases at the beginning, then becomes flat and increases again after the phase transition. This is likely caused by the specific orientation of the orthorhombic phase shown in Fig. 4.4.

4.3.2 Oxygen vacancy distribution

The diffuse scattering study has confirmed that the oxygen vacancy pairs forms along [1 1 1] fluorite direction in Y-stabilised ZrO_2 [82]. Oxygen vacancy distribution can effect the pathway of oxygen diffusion. Before the oxygen diffusion study, it is important to check if our model can reproduce the oxygen vacancies distribution correctly. I locate the oxygen vacancy using the criterion defined in Ref [100]. Each four closest cations form a tetrahedron structure. If there is no oxygen in the tetrahedron, the centre of the tetrahedra is defined as the position of a vacancy. In my simulations, there are oxygen atoms with large displacement located just outside of tetrahedra. These tetrahedra also define an oxygen vacancy in the middle, which can create a incorrect oxygen-vacancy pair. The oxygen-vacancy partial distribution function is plotted in Fig. 4.12. The peak near 1 Å is due to the incorrect oxygen-vacancy pair mentioned above. Thus, I introduce an artificial cutoff between the oxygen vacancy and oxygen atom pair as 1.5 Å.

The vacancy vacancy partial distribution of $Zr_{1.8}Y_{0.2}O_{1.9}$ at room temperature is compared with that distribution from initial random distribution in Fig. 4.13. In Fig. 4.13, the positions of first three peaks are same as the peak positions of O-O partial pair distribution in $Zr_{0.8}Y_{0.2}O_{1.9}$, which those peaks correspond to cation-centered oxygen pairs along [1 0 0], [1 1 0] and [1 1 1]direction. It shows that the cation-centered oxygen vacancy pairs prefers to form along [1 1 1] direction . This result is in agreement with the diffuse scattering experiment

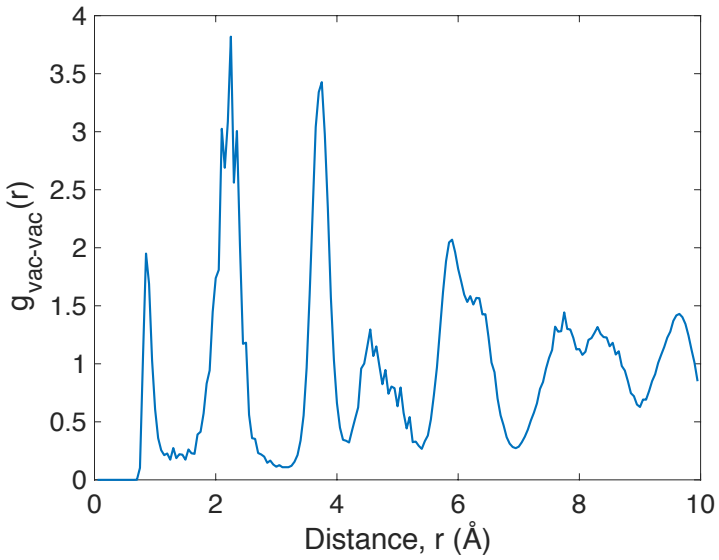

Figure 4.12: Partial distribution for $Zr_{0.8}Y_{0.2}O_{1.9}$ between oxygen atoms and oxygen vacancies at room temperature. The first peak is caused by incorrectly identified O vacancy.

result, which shows vacancy pairs forms along [1 1 1] fluorite direction in ZrO_2 with high concentration of Y [82]. In our simulation, 89 % of cation-centered oxygen vacancy pair is along [1 1 1] fluorite direction, 10 % is along [1 1 0] and less than 1 % of oxygen vacancy is along [1 0 0] at room temperature.

4.3.3 Oxygen Diffusion in Y-stabilised Cubic Zirconia

As mentioned above, the microstructure is less affected by the simulation size at high concentration of Y. Therefore, my diffusion study is mainly performed on $Zr_{1-x}Y_xO_{2-x/2}$ with 256,000 cations and a cellsize around 200 Å.

In Fig. 4.14, the diffusion coefficient of O calculated from the mean squared displacement, same methods as chapter 3, is plotted against the concentration of Y in temperature range between 1000 K and 1500 K. It shows that the maximum of oxygen diffusion coefficient occurs around 18% of Y. The maximum position of the concentration of Y is in good agreement with the experiment

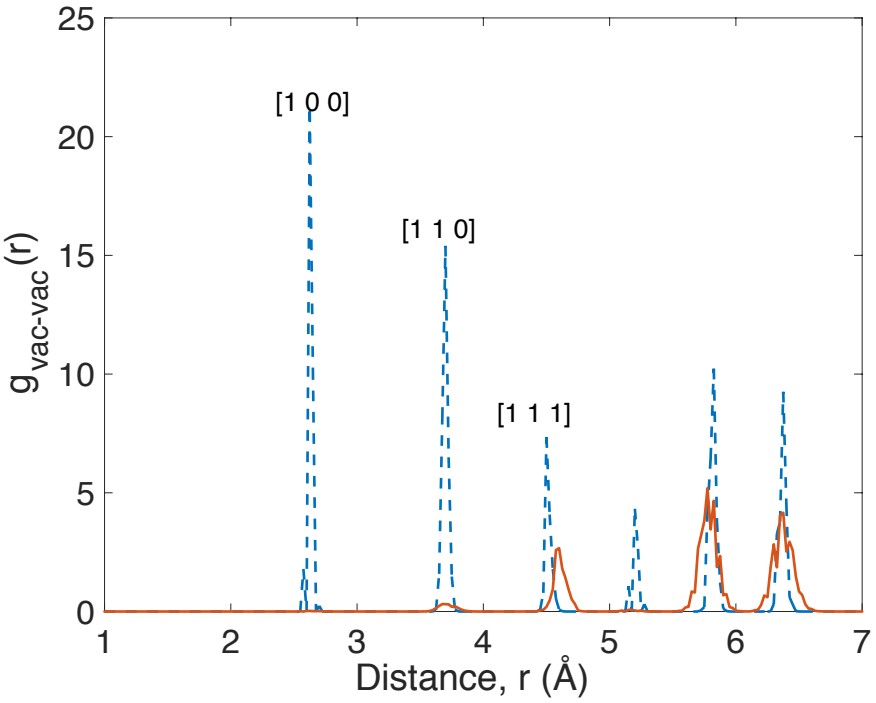

Figure 4.13: Partial distribution for $Zr_{0.8}Y_{0.2}O_{1.9}$ between oxygen vacancies and oxygen vacancies at room temperature. The red solid line is the distribution at room temperature and the blue dashed line is the random distribution of O vacancy.

result which is between 18–20% [89, 101]. We also noticed that the maximum position increases with decreasing temperature in our model. Although this result is different from the shift of maximum position from other studies [94, 101], the data is not extensive in those studies. It is necessary to perform more extensive experimental studies on diffusion maximum position.

In Fig. 4.15, the diffusion coefficient is plotted as ln D vs $1/T$, and the slope corresponds to the activation energy. The top of the graph shows that the slope is very steep at low concentration of Y and then decreases with concentration. The changes of slope become very small above 20% of Y concentration.

The diffusion coefficient in the system with low concentration of Y is shown in Fig. 4.15 where the temperature range is extended to 2000 K. I observe that the

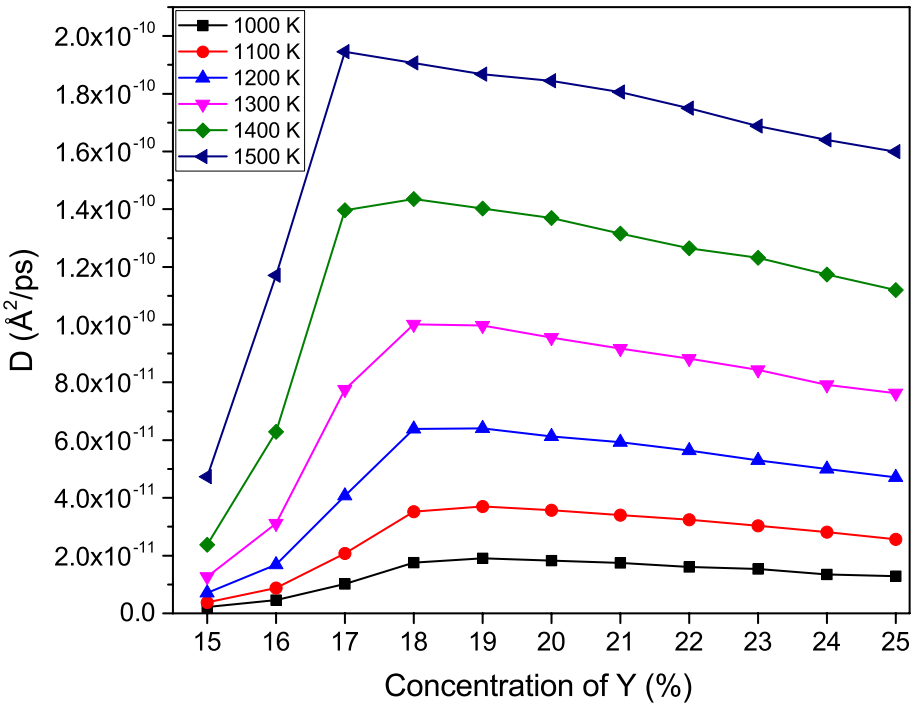

Figure 4.14: Diffusion coefficient of O vs concentration of Y for different temperature. The diffusion maximum occurs between 17% to 19% of Y.

slope changes with temperature. At higher temperature the slope decreases to its similar range at high concentration of Y. These results suggest that the activation energy of O diffusion only changes for different temperature range if the system is mixed with cubic and orthorhombic phase.

To establish how microstructures affect the activation energy of O diffusion, I examined the structures of a system that has not fully transformed to cubic phase at room temperature. The structures are selected at two temperature point, which correspond to before and after the change of the activation energy in Fig. 4.15. Fig. 4.16 shows the structure of ZrO_2 with 16% of Y at 1000 K and 1800 K, respectively. I observe that all the structure transforms to cubic when the temperature goes up to 1800 K. It suggests that temperature increase results in more domains transforming to the cubic phase. Since the structure also contributes to the O diffusion, the slope becomes steeper at lower temperature

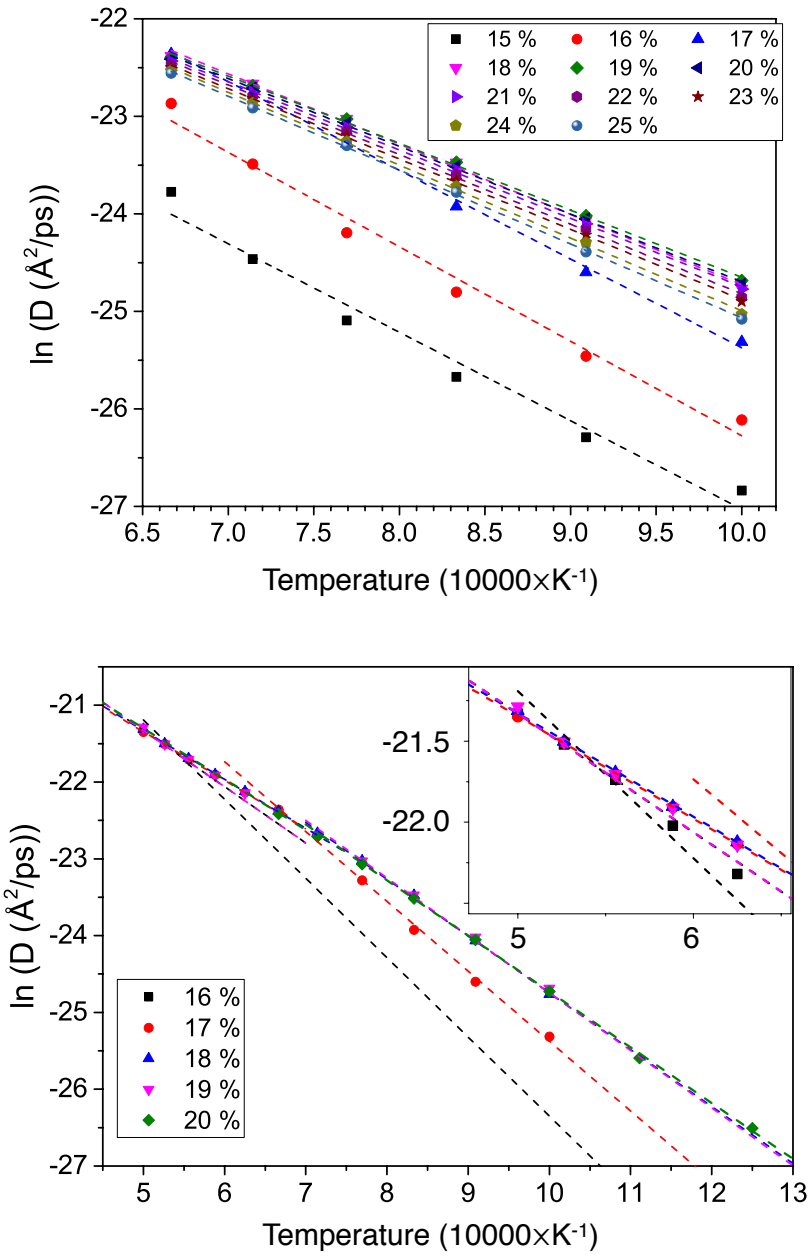

Figure 4.15: ln D vs $1/T$ for different concentration of Y. The slope changes with temperature.

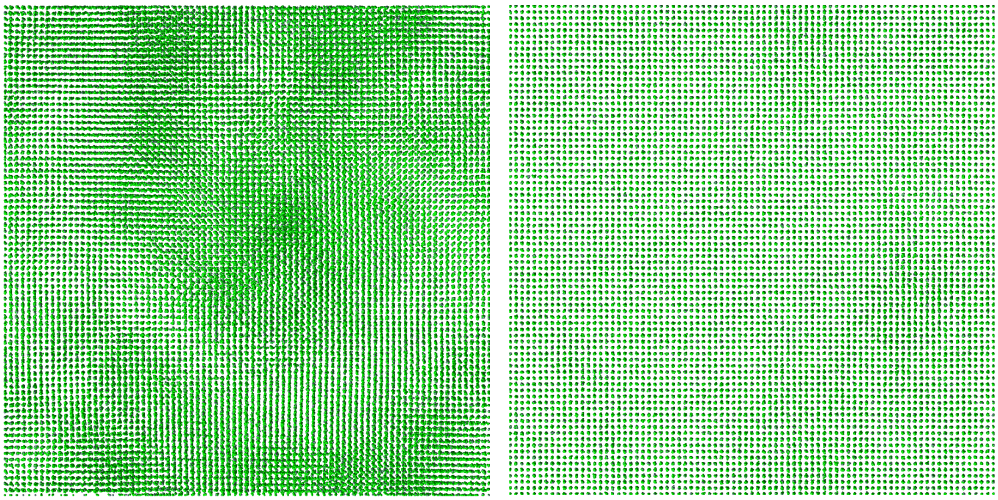

Figure 4.16: Structure for ZrO_2 with 16% of Y (Zr is coloured in green and Y is coloured in grey). The structure on the left is at 1000 K and on the right is at 1800 K. The structure transforms to the cubic phase entirely when temperature increase to 1800 K.

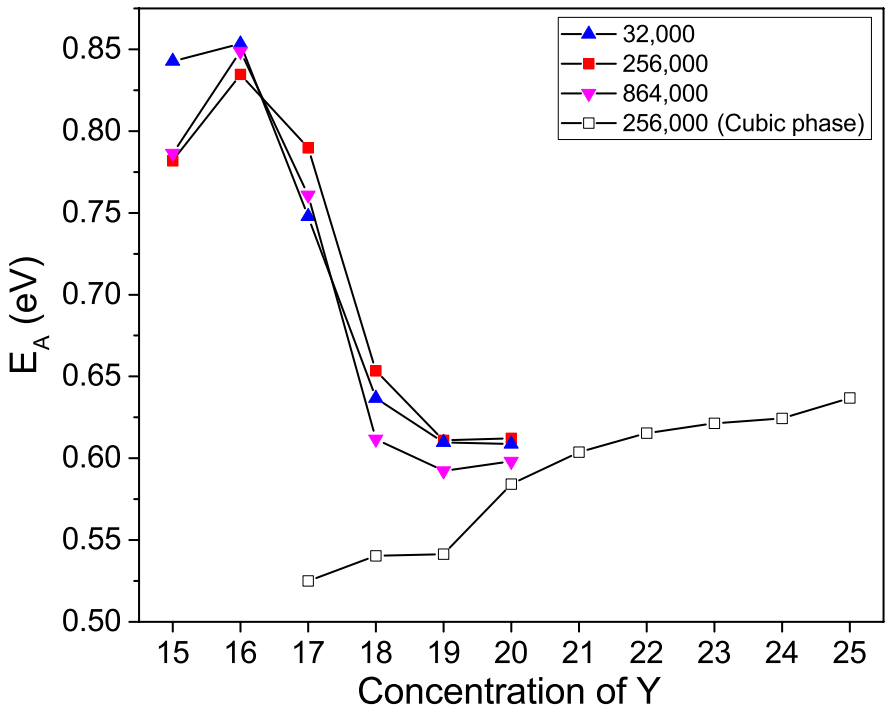

Figure 4.17: Activation energy of O diffusion vs concentration of Y for different system sizes. The activation energy of black open square is calculated in the system only contained cubic structure.

if there are orthorhombic domains in the system. These finding can explain the changes of activation energy observed in experiment studies [91, 92, 95].

There are 3 factors that could affect oxygen diffusion coefficient: concentration of oxygen vacancy, concentration of Y and structural change. ZrO_2 can transform to cubic structure at high temperature even without Y. The diffusion coefficient for cubic $Zr_{1-x}Y_xO_{2-x/2}$ can still be measured at lower concentration of Y at high enough temperature. Thus I can separate the effect of microstructure on the diffusion coefficient.

To summarise, the microstructures can be removed from the system by increasing temperature. I can control whether or not microstructure exists in the system by tuning the temperature. Hence, I can measure quantities that are not supposed to change with temperature such as the activation energy with or without microstructure.

Fig. 4.17 shows the activation energy of oxygen diffusion for $Zr_{1-x}Y_xO_{2-x/2}$ with 32,000, 256,000 and 864,000 cations. The black open square was calculated in the $Zr_{1-x}Y_xO_{2-x/2}$ with a single domain containing cubic structure shown in the right of Fig. 4.16. The rest were calculated in the systems with microstructure in the temperature range of 1500–2000 K. As can be seen from the black open square, where microstructure does not exist in the system, the activation energy shows almost linear increase with the concentration of Y. This is similar to the result of other simulations in the cubic phase [96, 102]. However if the microstructure exists, the activation energy starts from around 0.8 eV and decreases with the concentration of Y until the structure transforms completely to the cubic phase. The overestimated activation energy is due to the fact that the microstructure transforms with increasing temperature. To be more specific, when the temperature increases, the orthorhombic mi-

crostructure transforms to the cubic structure, which also enhances the O diffusion. Since the proportion of the orthorhombic microstructure decreases with increasing concentration of Y, the effect of microstructure decreases with increasing the concentration of Y. Hence, the activation energy starts at a higher value which then decreases to the same range as the activation energy in the cubic $Zr_{1-x}Y_xO_{2-x/2}$.

In summary, the microstructure plays a very important role in the diffusion process in the Y-stabilised ZrO_2. Its impact on activation energy is more significant than that the concentration of Y. This may be the reason why many diffusion simulations give a complicated and often unclear picture of what governs the activation energy [89, 90].

4.4 Conclusions

I have quantified and characterised the microstructure of $Zr_{1-x}Y_xO_{2-x/2}$ by simulation for the first time. To achieve the microstructure without constraining the cell, it is essential to perform simulations of very large systems. I observe that the system is composed by an interesting microstructure of cubic and orthorhombic coexisting phases. The microstructure transformation is quantified in the cubic-orthorhombic phase coexisting system. Although I do not observe the metastable tetragonal phase, there is a clear phase transition around 10% of Y. Both the concentration of the cubic phase and grain size show a rapid increase around 10% of Y.

In addition, I have also performed diffusion simulation in the Y-doped ZrO_2 with microstructure and have found that microstructure plays important role in the diffusion of O in the Y-doped ZrO_2. If the microstructure effect is excluded, an almost linear increase of the activation energy with increasing concentration

of Y follows.

Chapter 5

Developing a new CO_2 potential

In this chapter, I discuss my work in assisting the development of a new CO_2 potential that can better predict the dynamical properties of CO_2. Gibbs ensemble Monte Carlo (GEMC) simulations are performed to test the vapour-liquid coexisting line for our model. I subsequently tune the parameters of the potential to get better agreement with phonon dispersion curves.

5.1 Introduction

CO_2 is one of the most common moleculars in the world. There are some widely used empirical potentials in the literature such as EPM2 model [103] and TraPPE model [104]. They usually can reproduce good agreement of some of the fluid properties such as the vapour-liquid coexisting line, diffusion coefficient and density. Since our research is focused on dynamical properties of CO_2, I calculate phonon dispersion curves of crystalline CO_2, shown in Fig. 5.1, using the TraPPE model. As compared to the EPM2 model, this gives equally accurate for the phase diagram of CO_2 and better agreement for the mixture containing CO_2. However, it does not show good agreement with experiment phonon dispersion curves. Therefore, we would like to develop a

Table 5.1: Fitted Buckingham parameters and charge of C and O for CO_2.

	A (eV)	ρ (Å)	C (eV· Å)	Charge (|e|)
C–O	1978.66	0.2637	12.61	
O–O	2109.85	0.2659	22.28	-0.30403
C–C	1122.96	0.2778	0.0	0.60806

CO_2 potential based on ab initio simulations which can give a better agreement with both dynamical properties such as phonon dispersion curves and the energy surface.

5.2 Methods

The interaction between CO_2 molecules is described by the Buckingham potential. This potential was initially developed by my colleague Dr Min Gao and our PhD supervisor Prof. Martin Dove.The atomic charges were calculated using density function theory (DFT) method using NWchem [105, 106], combined with Distributed Multipole Analysis (DMA) method [107] using CamCASP [108]. DMA is a method that assigns multipole moments to specified site in a molecule. To provide more information about the energy surface, the formation energy of a large number different configurations of CO_2 is calculated by second order Møller-Plesset perturbation theory. Then the formation energies are used to fit the parameters of Buckingham potential using GULP [56].

To calculate the liquid-vapour coexisting curve the GCMC simulation was performed using the towhee code [110]. The system contain 500 CO_2 rigid molecules. I equilibrate the system using 1×10^4 MC cycles and collect the result for the following 4×10^4 MC cycles. Each cycle involves trail move for every molecular, change of volume and swap molecule between sub-box. The parameters are manually tuned and then fitted against the formation energies by GULP until we find a set of parameters is a good agreement with the

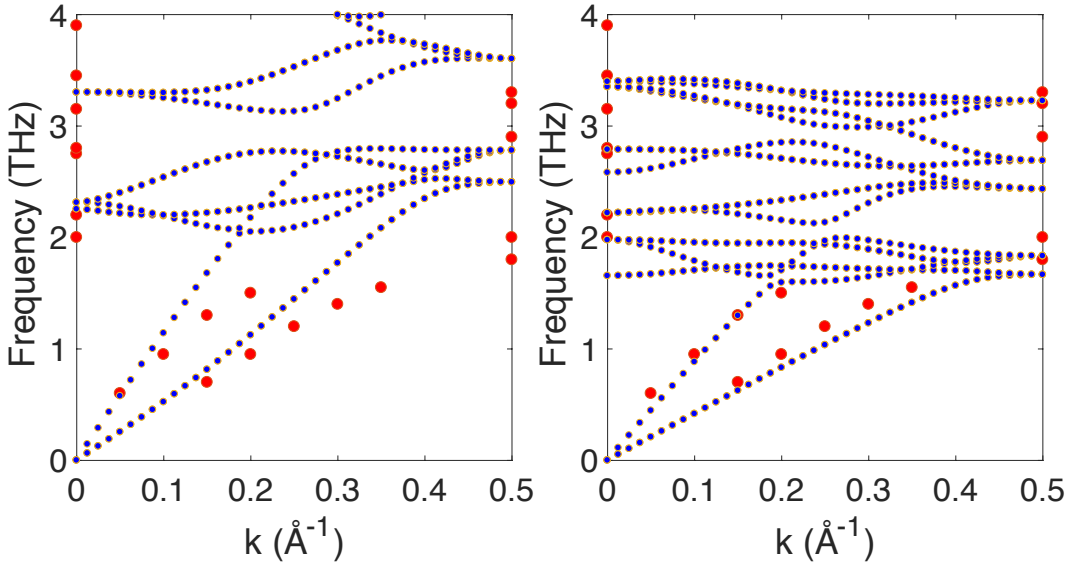

Figure 5.1: The dispersion curve of crystalline CO_2. The red circle are the experiment results and the blue asterisks are simulation results. The blue circle at the left and right were calculated from the TraPPE potential and our model, respectively.

experimental data of the coexisting line. The parameters of this potential are listed in Table 5.1.

The critical point cannot be directly calculated by the GCMC simulation because the formation energy of the liquid-vapour interface becomes smaller when the system is closer to the critical point. Thus, the liquid-vapour coexistence cannot be observed for the system just below the critical point [111]. To estimate the critical temperature, the critical density and temperature is fitted by the law of rectilinear diameters [45]. The rectilinear diameters states that there is a linear relationship between the average of density of gas and liquid and the temperature [112]:

$$\frac{\rho_l + \rho_g}{2} = \rho_c + A(T - T_c) \tag{5.1}$$

where ρ_l and ρ_g are the density of liquid and gas phase respectively, ρ_c is the critical density, T_c is the critical temperature and A is a parameter. The

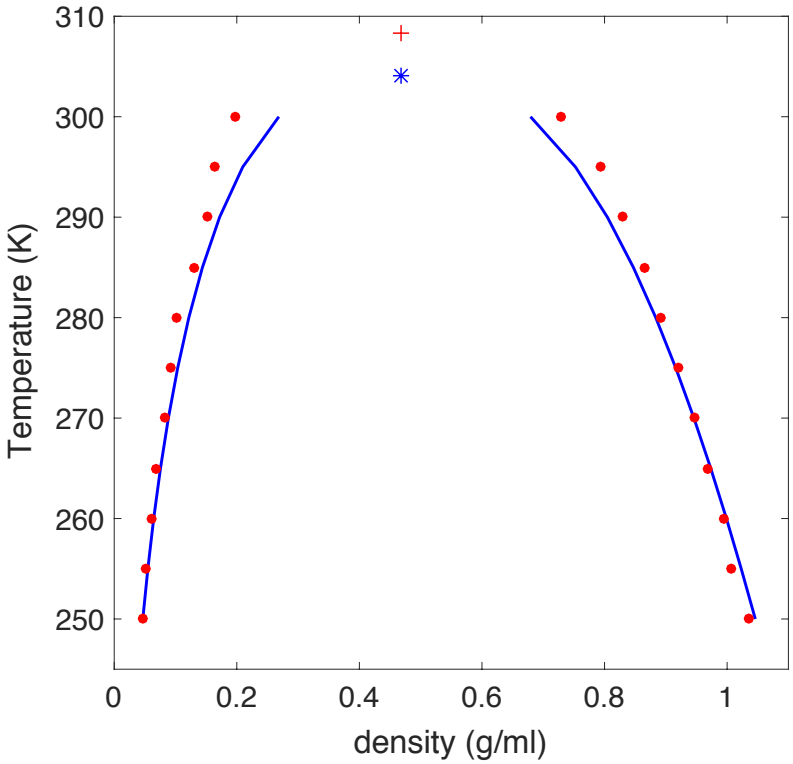

Figure 5.2: Vapour-liquid coexistence curve for CO_2. The blue curve and the asterisk are the coexistence line and critical point of the experimental data from the National Institute of Standards and Technology (NIST) [109]. The red circle and the plus sign are from my simulations.

relationship of the temperature and density difference follows the scaling law:

$$\rho_l - \rho_g = B(T - T_c)^\beta \tag{5.2}$$

where B is a parameter and β is the critical exponent which is approximately equal to 0.32 for a 3D system. This $\beta = 0.32$ is used in this fitting.

5.3 Results and discussion

The liquid-vapour coexistence densities are plotted in Fig. 5.2 and the vapour pressure as a function of temperature is plotted in Fig. 5.3. These plots show good agreement with the experimental results. The estimated critical point of

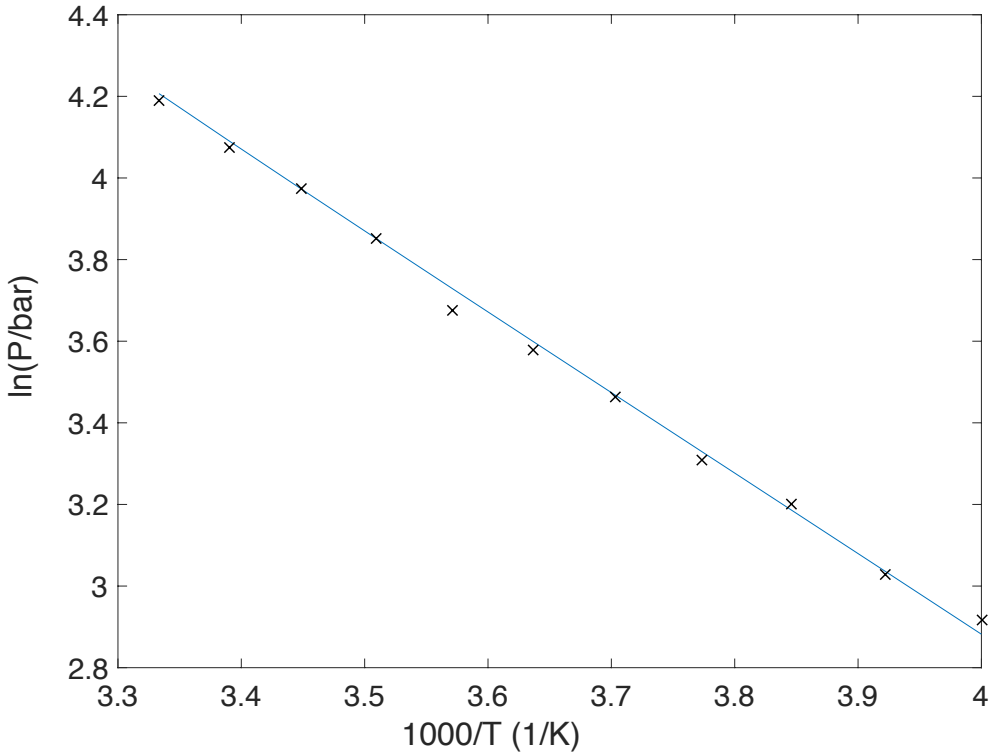

Figure 5.3: Clausius-Clapeyron plot of the saturated vapour pressure of CO_2 VS the inverse temperature. The blue line is the experiment data [109] and the black crosses are from my simulation.

our model is: T_c=308.39 K, P_c= 70.32 bar and ρ_c=465.95 kg/m^3. This agrees very well with the experiment data from NIST [109]: T_c=304.13 K, P_c= 73.77 bar and ρ_c=467.0 kg/m$_3$.

In Fig 5.2, I show the calculated phonon dispersion curves using GULP for both TraPPE model and our model and compare the simulation and experimental results. As can be seen, the dispersion curve from our model match the frequency spectrum of the measurement, but the TraPPE model gives a poor agreement with the experiment results. This result shows our model can reproduce much better crystal property.

5.4 Conclusions

In this chapter, I derived the parameters of CO_2 empirical potential using the ab initio method. This model results in a good agreement with the experiment results of vapour-liquid coexistence and the phonon dispersion curves. This gives us the confidence to study the dynamical properties of this system. This potential will be used to calculate the Frenkel line in CO_2 in the next section. It is also my hope that the new potential will be useful to the community interested in the properties of CO_2.

Chapter 6

Frenkel line and solubility maximum in supercritical fluids

A new dynamical line, the Frenkel line, has recently been proposed to separate the supercritical state into two states: rigid liquid and non-rigid gas-like fluid. The location of the Frenkel line on the phase diagram is unknown for real fluids. Here, I map the Frenkel line for three important systems: carbon dioxide (CO_2), water (H_2O) and methane (CH_4). This provides an important demarcation on the phase diagram of these systems, the demarcation that separates two distinct physical states with liquid-like and gas-like properties. I find that the Frenkel line can have similar trend as the melting line above the critical pressure. Moreover, I discuss the relationship between the unexplained solubility maxima and Frenkel line, and propose that the Frenkel line corresponds to the optimal conditions for solubility.

6.1 Introduction

Recently, there has been an increase of using supercritical fluids in extraction and purification applications, including in food, nuclear waste, petrochemical and pharmaceutical industries [27, 28, 42, 43]. Supercritical fluids attract significant attention due to their extremely good dissolving power and “tunable" properties. The solubility of supercritical fluids depends on density and diffusivity. Supercritical fluids combine the best of both worlds: high density of liquids and large diffusion constants of gases. Moreover, both of those properties can be tuned over a wide range pressure and temperature above the critical point, optimizing their dissolving ability.

Carbon dioxide, water and methane are three most commonly used supercritical fluids. In particular, H_2O and CO_2, are both abundant, non flammable and non toxic. They are also “non-polar” and “polar” solvent, respectively, so they can dissolve “polar” and “non-polar” solutes, respectively. The critical temperature (T_c) of CO_2 is 304 K, which is near room temperature, and the critical pressure (P_c) is 74 bar, which is also accessible. Additionally, CO_2 can be used with co-solvents to modify it into a "polar" solvent.

The solubility of a variety of solutes have been measured in supercritical CO_2 near T_c as a function of pressure [27]. Interestingly, the experiments show intriguing solubility maxima above the critical temperature: the solubility first substantially increases with pressure, followed by its decrease at higher pressure (the pressure range up to 1 GPa)[113–120]. This effect is not currently understood theoretically. Understanding it would lead to more efficiently use of supercritical fluids. More generally, it is often acknowledged that wider deployment of supercritical fluids and optimising their use would benefit from a theoretical guidance [27, 28].

Until recently, the supercritical state was believed to be physically homogeneous, which means that moving along any path on a pressure and temperature above the critical point does not involve marked or distinct changes. The Frenkel line has recently been proposed, which separates two dynamically distinct states: the gas-like regime where particle only have diffusive motion and the liquid-like regime where particle combine both solid-like quasi-harmonic vibrational motion and gas-like diffusive motion [30, 31, 121]. This transition take place when liquid relaxation time τ approaches Debye vibration period, τ_D. Debye vibration period is the inverse of Debye frequency. In Debye model, the Debye frequency is defined as the approximation of highest vibrational frequency in solid. The liquid relaxation time is defined in the usual way as the average time between two consecutive diffusion events (molecular rearrangements between two quasi-equilibrium positions) in the liquid at one point in space [2]. When $\tau \approx \tau_D$, the system loses the ability to support shear modes at all available frequencies, up to Debye frequency, and retains gas-like diffusive dynamics only. The Frenkel line starts from 0.7–0.8 T_c at P_c and extends to arbitrarily high pressure and temperature on the phase diagram [29]. There are many ways to locate the Frenkel line on the phase diagram, yet the velocity autocorrelation function (VACF) provides a convenient and mathematically meaningful criterion. It is well known that the VACF is a monotonically decaying function in the gas state, whereas it shows damped oscillations in the liquid and solid state. The VACF is defined as:

$$Z(t) = < \mathbf{v}(0) \cdot \mathbf{v}(t) > \tag{6.1}$$

On the basis of monotonic decay of VACF in gases, it has been proposed that the disappearance of oscillations and minima of the VACF, when varying temperature of pressure, corresponds to the point of pressure and temperature crossing the Frenkel line (FL) [29]. The disappearance of oscillations and

minima is result from the cage effect, namely the tagged atom is reflected neighbouring atoms [122]. Comparing with the Widom line [123] and Frenkel line, the Widom line serves as a continuation of liquid-vapour line beyond critical point and the Frenkel line separates the liquid-like rigid-fluids from supercritical fluids.

The Frenkel line has another independent thermodynamic definition. As discussed in the next chapter in more detail, liquids support solid-like transverse modes above the frequency $\frac{1}{\tau}$, i.e. at frequency at which the liquid is static and solid-like. As τ decreases with temperature, it starts to approaching the shortest (Debye) vibration period τ_{D}, at which point a particle spends about the same time oscillating and jumping. In other words, the loss of oscillatory behavior of particles corresponds to $\tau \to \tau_{\mathrm{D}}$, and when this happens all transverse disappear because they can propagate only above the frequency $\frac{1}{\tau}$. At higher temperature, only the longitudinal mode remains [124] (the longitudinal mode, related to density fluctuations, propagates in any elastic medium). The disappearance of transverse modes implies a well-defined value of specific heat $c_v = 2k_{\mathrm{B}}T$. Indeed, the remaining longitudinal mode contributes $k_{\mathrm{B}}T$ to the energy and the kinetic energy component of two transverse modes contributes $k_{\mathrm{B}}T/2$ to the energy each (the potential energy component of the two transverse modes disappears).

Importantly, the two independent criteria of the Frenkel line, the first one based on VAF and the second one based on c_v, coincide [29]. The coincidence serves as a self-consistency check in terms of physical effects. The coincidence enabled the authors to refer to the dynamical transition as the line, although I note that some physical properties such as viscosity and diffusion may not change at the line directly but close to it because they are path-dependent [16]. Indeed, viscosity and diffusion undergo qualitative changes in the supercritical

region but these changes may happen at different temperature and pressure depending on the path (e.g. along the isochore, isobar and so on).

In this chapter, I map the Frenkel line on the phase diagram for CO_2, H_2O and CH_4 using the VACF criterion and MD simulations. I study the location of the FL on the phase diagram, particularly addressing the slope of the line in relation to the melting line. I subsequently compare the Frenkel line with the solubility maximum from experiments [113–115, 117] and discuss why the Frenkel line can be related to the solubility maxima.

6.2 Methods

I use DL_POLY MD simulation package [44] and simulate 4576 CO_2 molecules, 3375 H_2O molecules and 3375 CH_4 molecules using constant-pressure-temperature ensemble. The intermolecular potential for CO_2 is my rigid-body potential described in the previous section. There is a large number of H_2O model due to its importance. TIP4P/2005 rigid non-polarizable model shows overall good performance for many properties [125, 126] among all the rigid non-polarizable models and acceptable computational cost. Thus in the chapter, the intermolecular potential of H_2O is TIP4P/2005 [127]. The intermolecular potential of CH_4 is taken from Ref. [128]. This potential also shows good accuracy in the supercritical state. I used a cut-off as 12 Å for potential. The simulation followed same protocol as described in methods section. I first equilibrate the system during 10 ps by scaling the velocities, then switche off the scaling during subsequent 40 ps under NPT ensemble. I collect and analyse the result during following 50 ps under NVE ensemble. That protocol gives convergent of VACF. In the range of my simulations, the difference between MD and experimental density from the NIST data base [109], is less than 5%.

The pressure range extends to several GPa and includes the pressure used in industrial applications.

6.3 Results and Discussion

In the previous work [29], it was proposed that the disappearance of VACF minima corresponds to pressure and temperature of the Frenkel line. In Fig. 6.1, I show representative VACFs for CO_2, H_2O and CH_4 at 900 bar. I can clearly see that as the temperature increases, the minimum becomes more shallow and finally disappears, which corresponds to the loss of oscillatory component of molecular motion and gives (P,T) for the Frenkel line.

In Fig. 6.2, I map the Frenkel line for CO_2, H_2O and CH_4 using the VACF criterion of the disappearance of the minimum. I also show the melting line [129–132] on the phase diagram. I can see the the Frenkel line for all three fluids starts from $0.7\sim 0.8$ T_c at P_c, similarly to the previous result for Lennard-Jones fluids [29].

It has been predicted in Ref.[29] that the Frenkel line starts slightly below the critical point and at high pressure is parallel to the melting line in the log-log plot [133]. The parallelism follows from the scaling argument: starting from high GPa pressures, the intermolecular interaction is reduced to its repulsive part only, whereas the cohesive attracting part no longer affects interactions (at low pressure, the parallelism between the two lines holds only approximately because the interactions are not well approximated by simple repulsive laws, see below). In a sufficiently wide pressure range, the repulsive part can be well approximated by several empirical interatomic potentials such as the Buckingham-type functions or Lennard-Jones potentials with inverse power-law leading terms at short distances $U \propto \frac{1}{r^n}$. For the inverse power law, a

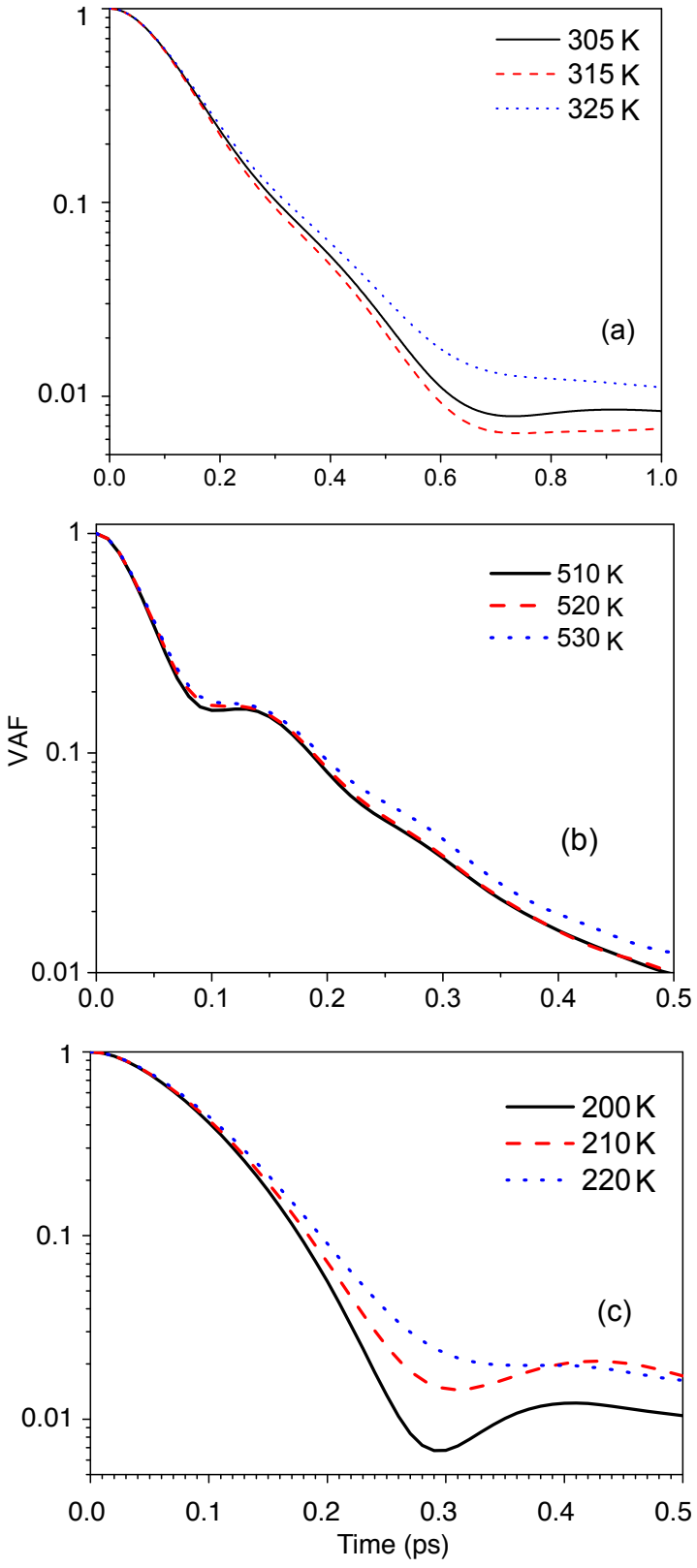

Figure 6.1: VACFs for CO_2 (a), H_2O (b) and CH_4 (c) calculated at 900 bar showing the disappearance of the minima at the Frenkel line.

well-known scaling of pressure and temperature exists: the system properties depend only on the combination of TP^{γ} , where γ is uniquely related to n. Consequently, TP^{γ} = constant on all (P, T) lines where the dynamics of particles changes qualitatively, as it does on both the melting line and the Frenkel line. This implies that the Frenkel and melting lines are parallel to each other in the double-logarithmic plot.

Although my simulation did not extend to high enough pressure to meet the condition above, I still can see that the Frenkel line has a similar trend as the melting line: for CO_2, the slopes of the Frenkel line and the melting line both starts to increase around 1,000 bar. For H_2O, both lines are flat below 1,000 bar, but their slopes start increasing at higher pressure. I also observe a similar increase in slope for methane simultaneously around 1,200 bar.

To discuss the relationship between the solubility and the dynamic property of supercritical fluid, I show experimental isothermal solubility maxima of different solutes in CO_2 [113–119], on the phase diagram (Fig. 6.2(a)). Importantly, I observe the points of solubility maxima are close to the Frenkel line. The solubility of maxima of several solutes, such as β-carotene, 1,4-bis-(n-alkylamino)-9,10-anthraquinone and 1,4-bis-(hexadecylamino)-9,10-anthraquinone coincide with the Frenkel line.

I now explain the proximity of the solubility maxima and Frenkle line as follows. Let us fix a temperature above the critical point to the left of the Frenkel line and increase the pressure (moving horizontally to the right in Fig. 6.2). Pressure has two competing effects on diffusion. On one hand, it increases density and hence the contact area and cleaning (dissolving) efficiency. On the other hand, the density increase results in decreasing the diffusion constant and hence reduces the solubility. Indeed, below the Frenkel line

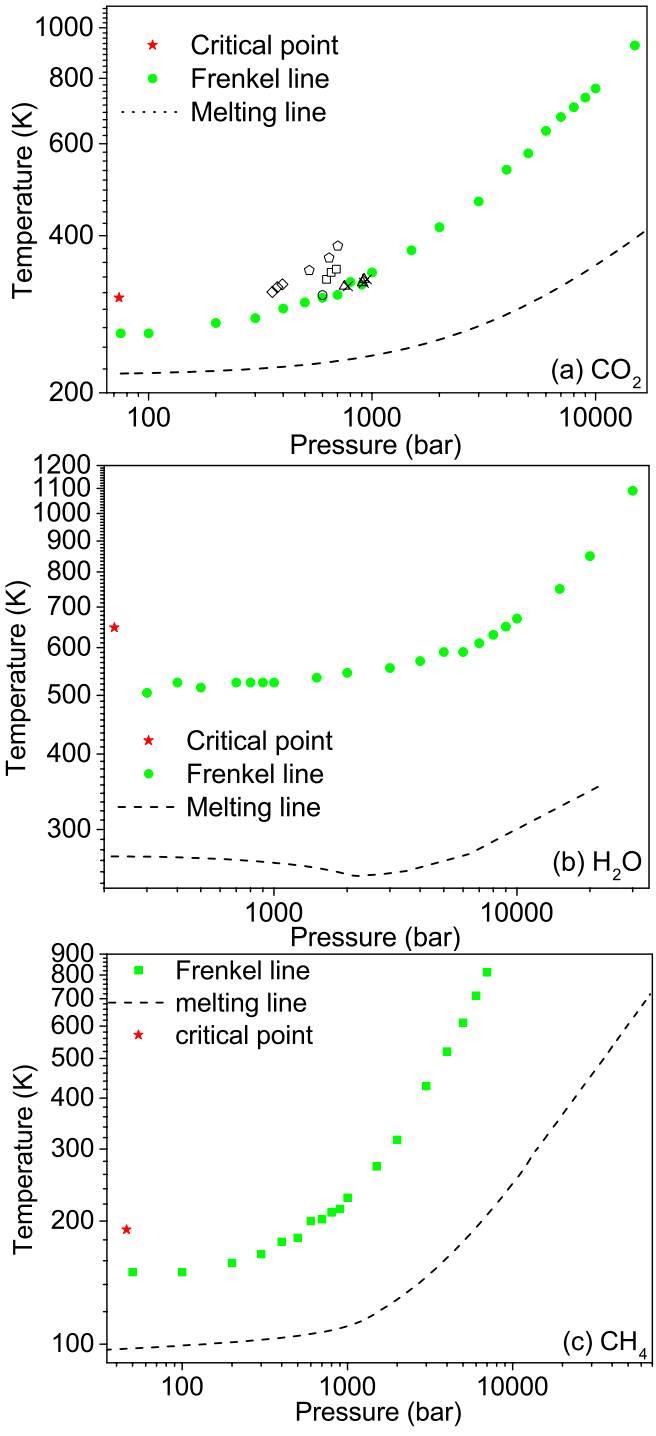

Figure 6.2: (P,T) phase diagram of Frenkel line of CO_2, H_2O and CH_4. The solubility maximum of different solutes in supercritical CO_2 are shown in graph (a). The open circle are the solubility of β-carotene [117]; the squares are 1,4-bis-(octadecylamino)-9,10-anthraquinone [113]; triangles are 1,4-bis-(n-alkylamino)-9,10-anthraquinone [114]; the diamonds are biphenyl [115]; the pentagon are adamantane [118]; the cross are 1,4-bis-(hexadecylamino)-9,10-anthraquinone [119]

where the molecular dynamics acquires the oscillatory component, molecular rearrangements become markedly less frequent, in contrast to the gas-like dynamics above the line where the oscillatory component of motion is absent. At the Frenkel line, the supercritical fluid has maximal density possible at which the diffusion is still in the fast gas-like regime and not in the slow liquid-like regime. Therefore, the proposal is that the optimal combination of these two properties at the Frenkel line gives the observed solubility maxima.

The data for solubility maxima for H_2O and CH_4 are not available. From the Fig. 6.2 (b) and (c), I see the reason why it is difficult to perform these experiments. In the case of water, the pressure at the Frenkel line corresponding to T_c is about 9,000 bar, or approximately $40P_c$ of H_2O (220.64 bar). Although the pressure of CH_4 corresponding to T_c at the Frenkel line is not too high ($\sim$600 bar), the pressure increases to $\sim$4,000 bar at room temperature. In both cases, these pressure are much higher than P_c, and performing solubility experiments at these pressures is challenging. On the other hand, the pressure corresponding to T_c at the Frenkel line for CO_2 is lower and about $1,000$ bar.

Based on the above results, I propose that the Frenkel line can serve as a predictive tool to locate the solubility maxima on the phase diagram. This provides a useful guide for future experiments.

I note that the increase of pressure along the Frenkel line results in several other interesting and potentially important effects such as the increase of fluid density and diffusion constant as well as the appearance of the viscosity minimum [29–31, 121]. In addition, surface tension tends to zero around and above the critical point so that that the problem of wetting is avoided. Accordingly, these conditions may favour other important properties of supercritical fluids: for example, the speed of chemical reactions may have a maximum close

to the Frenkel line. In this and other cases, supercritical technology could further benefit from theoretical guidance and receive an impetus for using the supercritical fluids in the hitherto unknown range of 1-10 kbars.

6.4 Conclusions

In summary, I mapped the Frenkel line for three important system: CO_2, H_2O and CH_4. This provides an important demarcation on the phase diagram of these systems, the demarcation that separates two distinct physical states with liquid-like and gas-like properties. I proposed that the Frenkel line can serve as a important guide to estimate the location of solubility maxima so that the cleaning and dissolving abilities of the supercritical fluids are optimized.

Chapter 7

Emergence and evolution of k-gap in spectra of liquid and supercritical states

Fundamental understanding of strongly-interacting systems necessarily involves collective modes, but their nature and evolution is not generally understood in dynamically disordered and strongly-interacting systems such as liquids and supercritical fluids. I report the results of extensive molecular dynamics simulations and provide direct evidence that liquids develop a gap in solid-like transverse spectrum in the reciprocal space, with no propagating modes between zero and a threshold value. In addition to the liquid state, this result importantly applies to the supercritical state of matter. I show that the emerging gap increases with the inverse of liquid relaxation time and discuss how the gap affects properties of liquid and supercritical states.

7.1 Introduction

Dynamical and thermodynamic properties of an interacting system are governed by collective excitations, or phonon modes. Collective modes have been studied in depth and are well-understood in solids and gases. This is not the case for the liquid state where the combination of strong interactions and dynamical disorder has been thought to preclude the development of a general theory [66] including understanding the nature of collective modes.

Collective modes in solids include one longitudinal and two transverse acoustic modes. In gases, the collective mode is one longitudinal long-wavelength sound wave considered in the hydrodynamic approximation. In liquids, collective modes are well-understood in the hydrodynamic approximation $\omega\tau < 1$ [134], where ω is frequency and τ is liquid relaxation time, the average time between diffusive particle jumps at one point in space in the liquid [2]. Importantly, there is a different regime of wave propagation: $\omega\tau > 1$ where waves propagate in the constant-structure environment, i.e. in the solid-like regime. Experiments have reported both indirect and direct evidence for the existence of solid-like waves in liquids and have ascertained that they are essentially different from the hydrodynamic modes [18–20, 22–26, 135–139] including those discussed in generalized hydrodynamics [7, 10].

As mentioned in the previous chapter, the first proposal regarding solid-like waves in liquids was due to Frenkel [2] who proposed that at times smaller than τ, particles do not jump and hence the system behaves like a solid. Therefore, for frequencies larger than

$$\omega_{\mathrm{F}} = \frac{1}{\tau} \tag{7.1}$$

the liquid supports two transverse acoustic modes as does the solid (glass or crystal). The longitudinal acoustic mode is unmodified (except for different dissipation laws in regimes $\omega\tau > 1$ and $\omega\tau < 1$ [2]): density fluctuations exist in any interacting medium, and in liquids they have been shown to propagate with wavelengths extending to the twice of the shortest interatomic separation [19, 20, 23–26].

The proposal that liquids are able to support solid-like transverse modes with frequencies extending to the highest frequency implies that liquids are similar to solids in terms of collective excitations. Therefore, main liquid properties such as energy and heat capacity can be described using the same first-principles approach based on collective modes as in solids, an assertion that was considered as unusual in the past when no evidence for propagating solid-like modes in liquids existed. Importantly, high-frequency modes are particularly relevant for liquid thermodynamics because, similarly to solids, they make the largest contribution to system's energy and other properties whereas the contribution of hydrodynamic modes is negligible [16].

The transverse modes were initially observed in viscous liquids, such as liquid boron trioxide and glycerol, using Brillouin scattering [136, 137]. The propagation of high-frequency transverse modes was later studied in low-viscosity liquids on the basis of positive dispersion [19, 20, 138, 139]. More recently, transverse modes were directly measured in the form of distinct dispersion branches and verified on the basis of computer modeling [22–26, 139]. However, this has been done at constant temperature (constant τ) only. The crucial open question is related to the *e*volution of propagating transverse modes in liquids: does the range of transverse modes dynamically change with τ and how? Answering it directly is essential for fundamental understanding of collective modes in liquids and for liquid theory in general.

Traditionally, Eq. (7.1) has been the basis for the transformation of liquid transverse modes [67]. It predicts that at a frequency above ω_{F}, the liquid response is solid-like. It further predicts that liquid collective modes transform: smaller τ at higher temperature results in shrinking the frequency range of transverse modes and their eventual disappearance when τ becomes comparable to the shortest time in the system comparable to Debye vibration period.

To describe the ability of liquid to operate in both hydrodynamic and solid-like elastic regimes, Frenkel modified the Navier-Stokes equation as follow:

$$\nabla^2 \mathbf{v} = \frac{1}{\eta}\left(\rho \frac{d\mathbf{v}}{dt} + \nabla p\right) \tag{7.2}$$

where $\mathbf{v}$ is velocity, p is pressure, η is shear viscosity, ρ is density and the total derivative is $\frac{d}{dt} = \frac{\partial}{\partial t} + \mathbf{v}\nabla$.

Accounting for both long-time viscosity and short-time elasticity is equivalent to making the substitution $\frac{1}{\eta} \rightarrow \frac{1}{\eta} + \frac{1}{G}\frac{d}{dt}$. Using the Maxwell relationship $\eta = G\tau$ this gives:

$$\frac{1}{\eta} \rightarrow \frac{1}{\eta}\left(1 + \tau \frac{d}{dt}\right) \tag{7.3}$$

Using (7.3) in Eq. (7.2) gives

$$\nabla^2 \mathbf{v} = \frac{1}{\eta}(1 + \tau \frac{\mathrm{d}}{\mathrm{d}t})(\rho \frac{\mathrm{d}\mathbf{v}}{\mathrm{d}t} + \nabla p) \tag{7.4}$$

An approximate solution of Eq. (7.4) has been proposed in ref. [16].

Considering the absence of external forces, $p = 0$ and the slowly-flowing fluid so that $\frac{d}{dt} = \frac{\partial}{\partial t}$. Then, Eq. (7.4) reads

$$\eta \frac{\partial^2 v}{\partial x^2} = \rho\tau \frac{\partial^2 v}{\partial t^2} + \rho \frac{\partial v}{\partial t} \tag{7.5}$$

where v can be y or z velocity components perpendicular to x.

In contrast to the Navier-Stokes equation, Eq. (7.5) contains the second time derivative of v and therefore allows for propagating waves. Indeed, Eq. (7.5) without the last term represents the wave equation for shear waves with velocity $c_s = \sqrt{\frac{\eta}{\tau\rho}} = \sqrt{\frac{G}{\rho}}$. Using $\eta = G\tau = \rho c_s^2 \tau$, Eq. (7.5) can be re-written as

$$c_s^2 \frac{\partial^2 v}{\partial x^2} = \frac{\partial^2 v}{\partial t^2} + \frac{1}{\tau} \frac{\partial v}{\partial t} \tag{7.6}$$

Looking for the solution of (7.6) as $v = v_0 \exp\left(i(kx - \Omega t)\right)$ gives the quadratic equation for Ω:

$$\Omega^2 + \Omega \frac{i}{\tau} - c_s^2 k^2 = 0 \tag{7.7}$$

Equation (7.7) has imaginary roots if $c_s k < \frac{1}{2\tau}$. If $c_s k > \frac{1}{2\tau}$, Eq. (7.7) gives $\Omega = -\frac{i}{2\tau} \pm \sqrt{c_s^2 k^2 - \frac{1}{4\tau^2}}$. This gives

$$\begin{aligned} v &\propto \exp\left(-\frac{t}{2\tau}\right) \exp(i\omega t) \\ \omega &= \sqrt{c_s^2 k^2 - \frac{1}{4\tau^2}} \end{aligned} \tag{7.8}$$

where k is the absolute value of wavevector and τ is the relaxation time. Eq. (7.8) describes propagating shear waves.

Interestingly, Eq. (7.8) predicts that liquid transverse acoustic modes develop a *gap* of k points from 0 to k_{gap}:

$$k_{gap} = \frac{1}{c\tau} \tag{7.9}$$

The τ, in this equation, is understood to be the full period of particles' jump motion equal to twice Frenkel's τ. Eqs. (7.8)-(7.9) further predict that the k-gap increases with temperature because τ decreases.

Importantly, it can be predicted that the k-gap also emerges in the supercritical state of matter. It has been proposed earlier that solid-like transverse modes should propagate above the critical point provided the system is below the Frenkel line (FL) [16, 29–31]. I therefore predict that supercritical fluids below the FL should also develop the same gap (7.9) in the transverse spectrum.

The main aim of this chapter is to obtain direct evidence for the gap discussed above. I perform extensive molecular dynamics simulations in different types of liquids and supercritical fluids, including noble and molecular. I find that a gap develops in solid-like transverse acoustic spectrum in reciprocal space which increases with the inverse of liquid relaxation time. These specific results call for new high-temperature and pressure experiments.

7.2 Methods

7.2.1 Details of molecular dynamics simulations

I aimed to study the propagation of solid-like transverse waves in liquids with different structure and bonding types, and have simulated noble liquid Ar with Lennard-Jones potential as well as molecular CO_2 with the empirical potential I derived and described in chapter 5. I have used the DL_POLY molecular dynamics (MD) program [44] and systems with 125,000 and 117,912 particles for Ar and CO_2, respectively with periodic boundary conditions. I equilibrated

the system during 15 ps in NPT ensemble and ensured the equilibration at given (P,T) during the subsequent 10 ps run. I collect the results during the following 200 ps for Ar, and 80 ps for CO_2 in NVE ensemble. The pressure was fixed at 40 bar for subcritical liquid Ar, 10 kbar for supercritical Ar and 9 kbar for supercritical CO_2. The temperature was extended well above critical for the last two systems. Relaxation time τ was calculated as the time during which the intermediate scattering function reduces by a factor of e [140]. The intermediate scattering function is described in the below.

7.2.2 Intermediate scattering function

The intermediate scattering, which is the Fourier transform of the van Hove function, describes density fluctuations in the system. The van Hove Function is a time dependent radial distribution function [141]. The density in the system can be defined as:

$$\rho(r,t) = \sum_{i=1}^{N} \delta(r - r_i(t)) \tag{7.10}$$

where r_i is the coordinates of the particle i and N is the total number of particles. The Fourier transform of the density function reads:

$$\begin{aligned} \rho(\mathbf{Q},t) &= \frac{1}{2\pi} \sum_{i=1}^{N} \int \mathrm{d}r \exp(i\mathbf{Q}\cdot r)\delta(r - r_i(t)) \\ &= \frac{1}{2\pi} \sum_{i=1}^{N} \exp[i\mathbf{Q}\cdot r_i(t)] \end{aligned} \tag{7.11}$$

where $\mathbf{Q}$ is wavevector. The intermediate scattering can be calculated as the density correlation function:

$$\begin{aligned} F(\mathbf{Q},t) &= \frac{1}{N}\langle \rho(-\mathbf{Q},0)\rho(\mathbf{Q},t)\rangle \\ &= \frac{1}{N}\langle \sum_{i=1}^{N}\sum_{j=1}^{N} \exp[i\mathbf{Q}\cdot(r_j(0) - r_i(t))]\rangle \end{aligned} \tag{7.12}$$

The self-part of intermediate scattering function is also called incoherent intermediate scattering function:

$$F_{\mathrm{s}}(\mathbf{Q},t)=\frac{1}{N}\langle\sum_{i=1}^{N}\exp[i\mathbf{Q}\cdot(r_i(0)-r_i(t))]\rangle \tag{7.13}$$

The incoherent intermediate scattering function does not contain the information about structure, but the dynamic property of a single particle. In liquids, this function will follow the power law:

$$F_{\mathrm{s}}(\mathbf{Q},t)=\exp(-\frac{t}{\tau}) \tag{7.14}$$

where τ is the relaxation time. Thus, I can evaluate liquid relaxation time τ as the time during which the intermediate scattering function decays by a factor e [140].

7.2.3 Current-current correlation function

I calculate the propagating transverse modes using transverse current correlation functions [10]. Taking the derivative of Eq. 7.11, we can write:

$$\frac{\mathrm{d}\rho(\mathbf{k},t)}{\mathrm{d}t}=i\mathbf{k}\cdot\sum_{i=1}^{N}v_i(t)\exp[i\mathbf{k}\cdot r_i(t)] \tag{7.15}$$

The current function is defined as:

$$j(\mathbf{k},t)=\sum_{i=1}^{N}v_i(t)\exp[i\mathbf{k}\cdot r_i(t)] \tag{7.16}$$

In Eq. 7.15, the function only includes the case where wavevectors $\mathbf{k}$ parallel to the current. The full current can be written as:

$$\begin{aligned} j(\mathbf{k},t) &= j_{\mathrm{L}}(\mathbf{k},t)+j_{\mathrm{T}}(\mathbf{k},T) \\ &= \mathbf{k}\cdot j(\mathbf{k},t)+\mathbf{k}\times j(\mathbf{k},t) \end{aligned} \tag{7.17}$$

where $j_{\mathrm{L}}(\mathbf{k},t)$ is the longitudinal current and $j_{\mathrm{T}}(\mathbf{k},T)$ is the transverse current.

The current-current correlation is calculated as:

$$C_{\mathrm{L}}(k,t) = \langle j_{\mathrm{L}}(\mathbf{k},0) j_{\mathrm{L}}(-\mathbf{k},t)\rangle \quad C_{\mathrm{T}}(k,t) = \langle j_{\mathrm{T}}(\mathbf{k},0) j_{\mathrm{T}}(-\mathbf{k},t)\rangle \tag{7.18}$$

where k is absolute value of the wave vector. The spectra of the longitudinal and transverse current can be calculated by the Fourier transform:

$$\begin{aligned} C_{\mathrm{L}}(k,\omega) &= \frac{1}{2\pi}\int C_{\mathrm{L}}(k,t)\exp(-i\omega t)\mathrm{d}t = \omega^2 S(Q,\omega) \\ C_{\mathrm{T}}(k,\omega) &= \frac{1}{2\pi}\int C_{\mathrm{T}}(k,t)\exp(-i\omega t)\mathrm{d}t \end{aligned} \tag{7.19}$$

$S(Q,\omega)$ is the Fourier transform of intermediate scattering function $F(Q,t)$. These function gives us the information about collective modes in liquid. The maxima of $C_{\mathrm{L}}(k,\omega)$ and $C_{\mathrm{T}}(k,\omega)$ gives us the peak mode frequencies, enabling us to construct dispersion curves for longitudinal modes and transverse modes. Although the transverse modes cannot be directly measured in liquids experimentally[1] , the MD simulation enables to calculate the transverse current-current correlation function directly.

A smoothing function is often used for the analysis of C_{T} in order to reduce the noise [25, 26]. To get better quantitative and model-free results, I choose not to use the smoothing function. Instead, I repeat my MD simulations 20 times using different starting velocities and average the results. This produces C_{T} with reduced noise which does not appreciably change when the number of simulations is increased. When oscillations of $C_{\mathrm{T}}(k,\omega)$ are clearly visible, the Fourier transforms are taken to calculate $C_{\mathrm{T}}(k,\omega)$. I show examples of $C_{\mathrm{T}}(k,\omega)$ for two different peak position of frequencies spectrum and two different wavevector in Fig. 7.1 and Fig. 7.2 respectively.

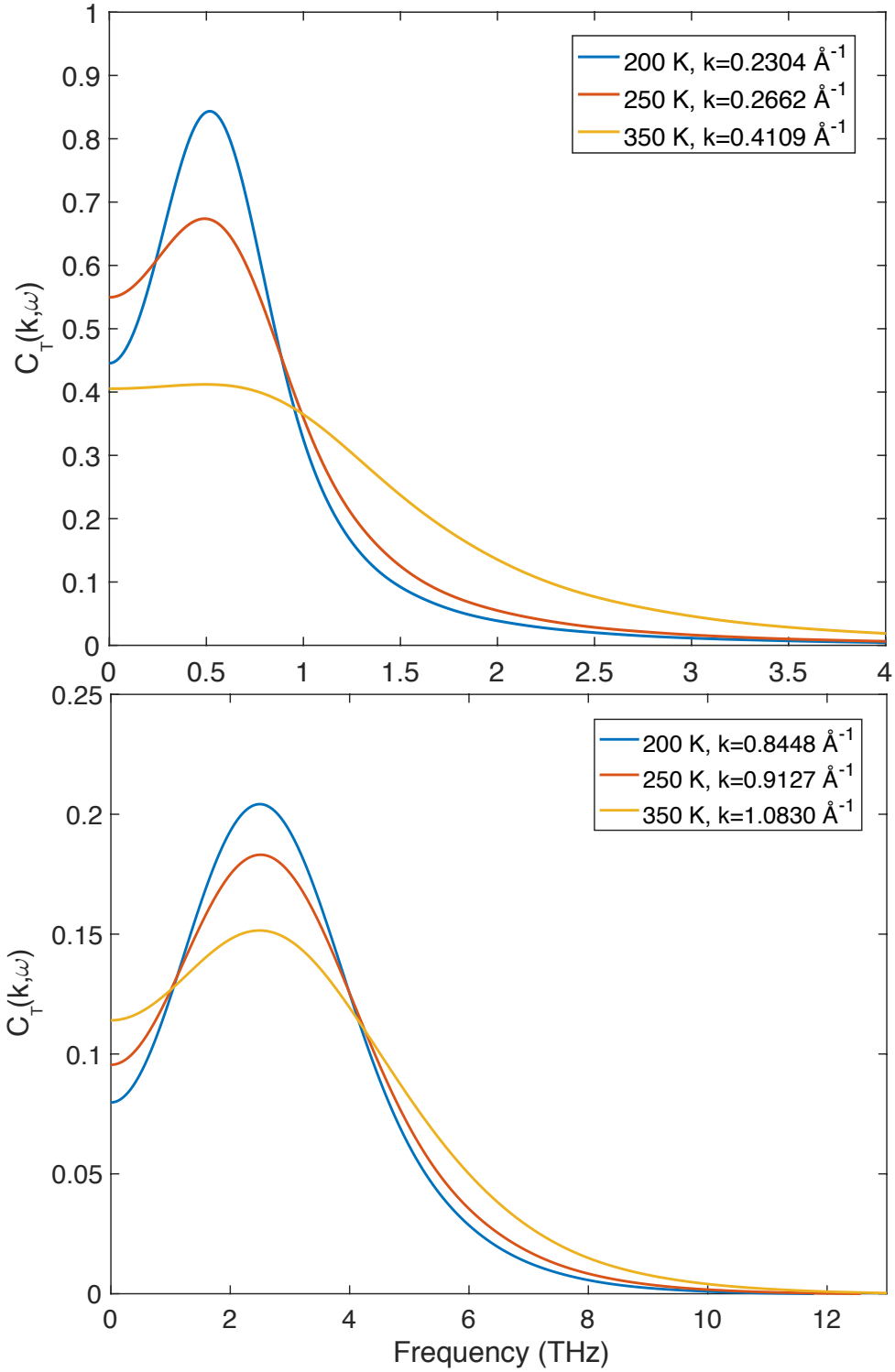

Figure 7.1: $C_T(k,\omega)$ of supercritical Ar at 200 K, 250 K and 350 K for two phonon modes with peak frequencies of about 0.5 THz (top) and 2 THz (bottom). To study the effect of temperature on peak frequency, $C_T(k,\omega)$ at higher temperature are shown at larger k because ω decreases with temperature (see Fig. 7.4).

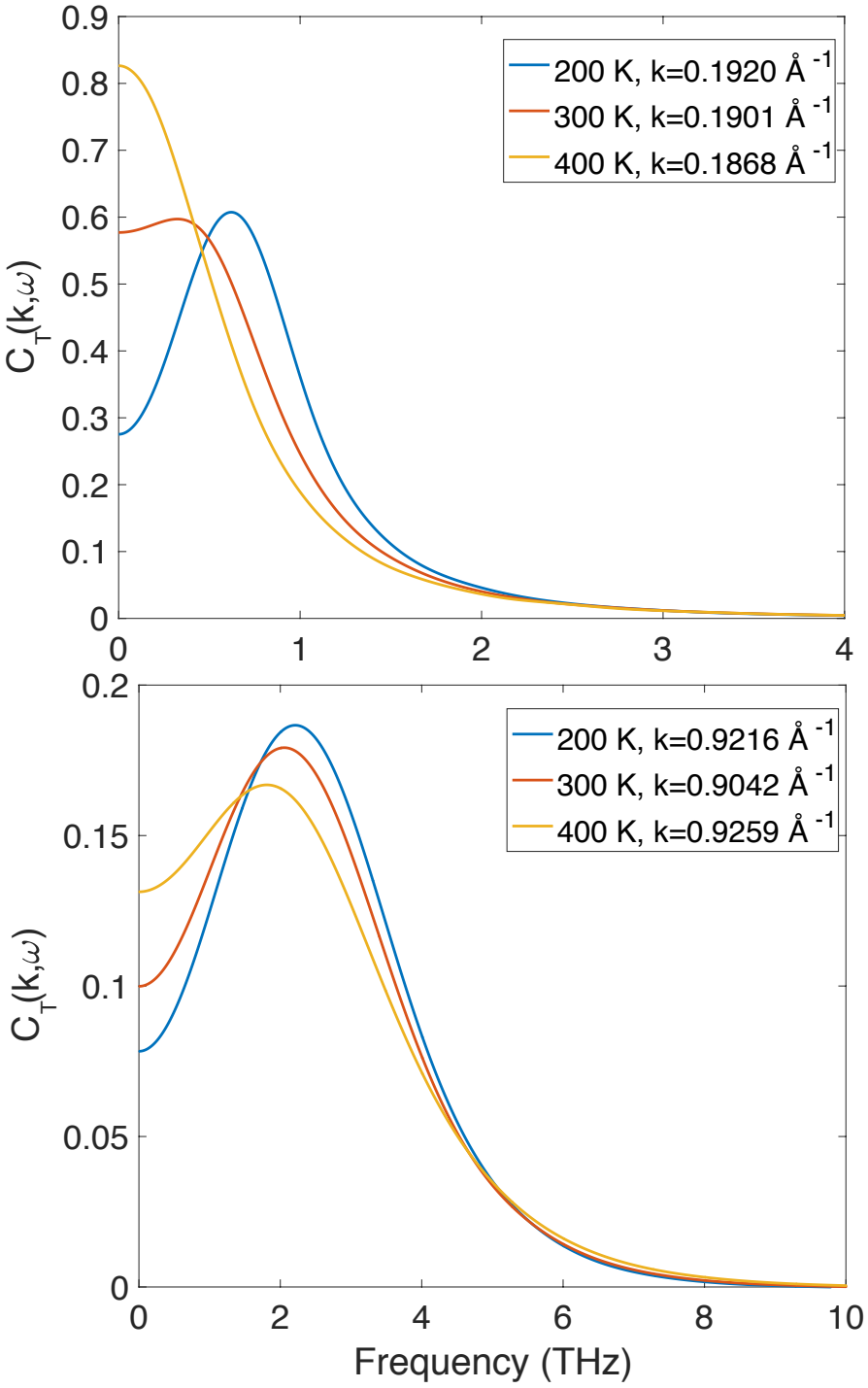

Figure 7.2: $C_T(k,\omega)$ of supercritical Ar at 200 K, 300 K and 400 K for two phonon modes with fixed wavevector.

7.3 Results and Discussion

I observe that the intensity of $C_{\mathrm{T}}(k,\omega)$ peaks decreases and broadens with temperature for all mode frequencies, but lower-frequency peaks decay much faster as compared to higher-frequency ones. In examples in Fig. 7.1, both 0.5 THz and 2 THz transverse modes show a clear peak at 200 K but whereas the peak of the 0.5 THz mode almost disappears at 350 K, the 2 THz mode peak remains pronounced. This is consistent with the experimental results showing that low-frequency transverse phonons are not experimentally detected [23, 24]. In the Fig. 7.2, the $C_{\mathrm{T}}(k,\omega)$ shows monotonically decay at 400 K and $k = 0.1920$, which suggest this transverse mode has disappeared.

The main observation is related to the evolution of dispersion curves. I plot intensity maps $C_{\mathrm{T}}(k,\omega)$ in Figure 7.3 and observe that a gap develops in k space and the range of transverse modes progressively shrinks.

A maximum of $C_{\mathrm{T}}(k,\omega)$ at frequency ω is related to a propagating mode at that frequency and gives a point (k,ω) on the dispersion curve [10]. I plot dispersion curves in Figure 7.4 and observe a detailed evolution of the gap. It can be seen that although the the value of wavevector changes with increasing temperature at fixed frequency, the relative wavevector $k - k_{\mathrm{gap}}$ varies little. At the highest temperature simulated, $C_{\mathrm{T}}(k,\omega)$ becomes not easily discernible from the noise.

I observe that the gap k_{gap} develops in all systems simulated. Importantly, the simulated systems where I detect transverse modes extended into the supercritical state: our maximal temperature and pressure correspond to ($205.6P_c$, $6.3T_c$) for Ar and ($122.0P_c$, $2.0T_c$) for CO_2. Using the previously

[1] transverse modes are detected in the longitudinal scattering function due to the projection of transverse waves along longitudinal direction [22–25]

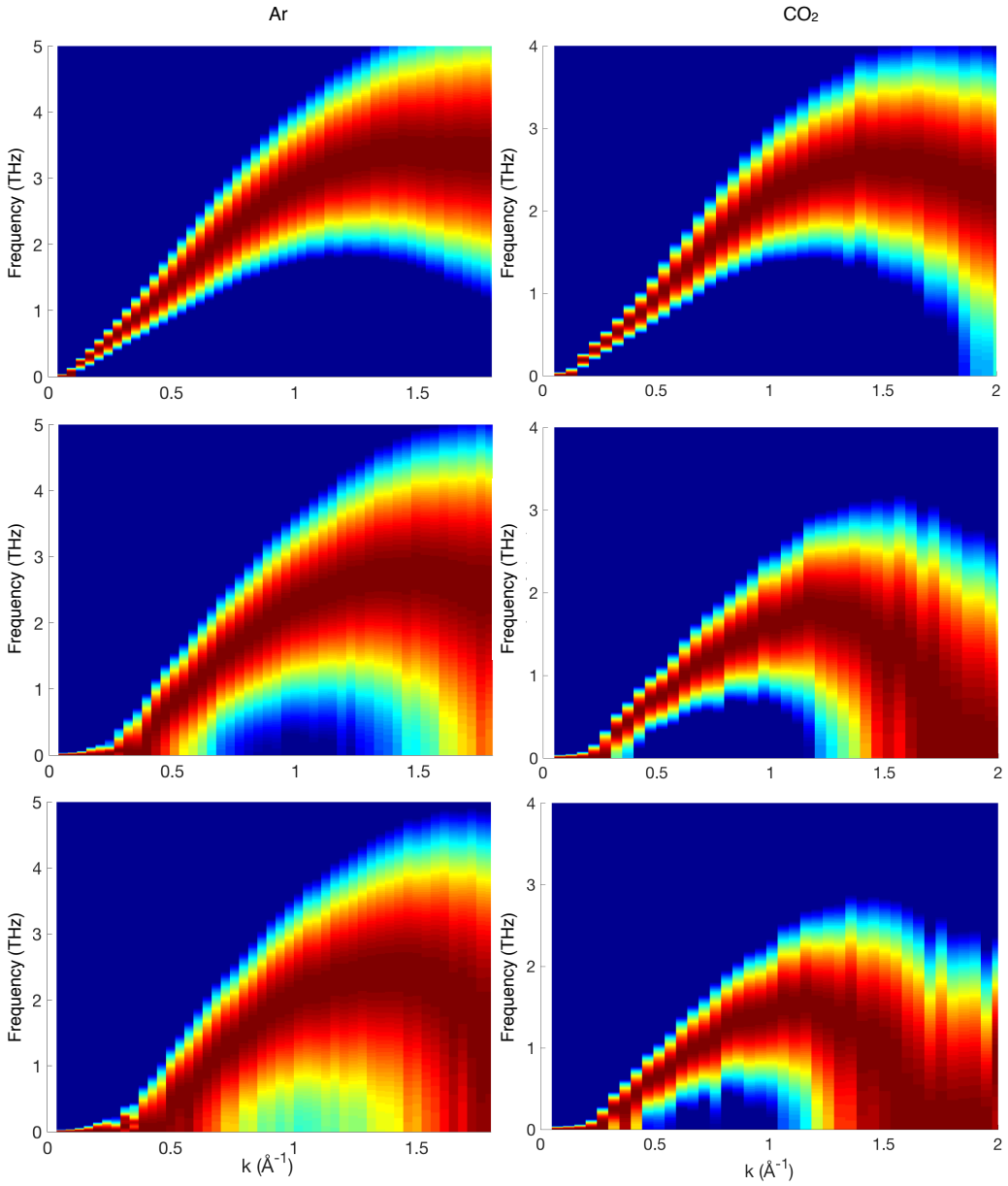

Figure 7.3: Intensity maps of $C_T(k,\omega)$ for supercritical Ar at 250 K (top), 350 K (middle) and 450 K (bottom) and supercritical CO_2 at 300 K (top), 400 K (middle) and 500 K (bottom). The maximal intensity corresponds to the middle points of dark red areas and reduces away from them.

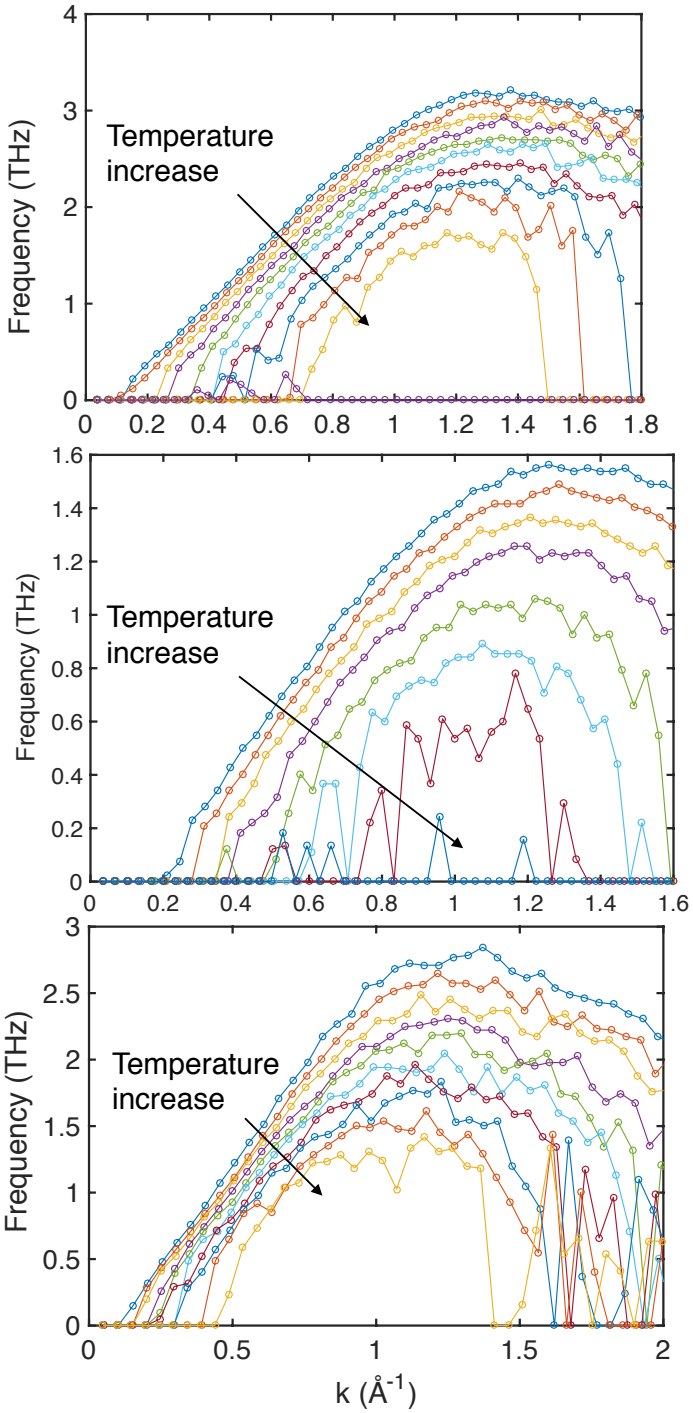

Figure 7.4: Phonon dispersion curve of supercritical Ar at 200-500 K and 550 K (top), subcritical liquid Ar at 85-120 K (middle) and supercritical CO_2 at 300-600 K (bottom). The temperature increment is 30 K, 5 K and 30 K for supercritical Ar, subcritical liquid Ar and supercritical CO_2, respectively.

calculated FL for Ar [29] and CO_2, I find that propagating solid-like transverse modes reported in Figure 7.3 correspond to supercritical Ar and CO_2 below the FL. My data therefore give direct evidence for propagating transverse modes in supercritical fluids below the FL. This is an important finding on its own because it has remained unclear whether the supercritical state is able to support solid-like transverse modes at all. Indeed, it has been proposed that the supercritical state supports transverse modes below the Frenkel line (FL), but there was no direct confirmation of this proposal.

I note that reduced peak intensity of $C_{\mathrm{T}}(k,\omega)$ at very high temperature, together with the persisting noise, can obfuscate the criterion of a propagating mode because a difference between a peak in $C_{\mathrm{T}}(k,\omega)$ at low temperature and a broad shoulder (hidden peak) at high temperature becomes less pronounced. However, one can also consider the oscillatory behavior of $C_{\mathrm{T}}(k,t)$ as an indicator of a propagating mode. In Figure 7.5, I plot $C_{\mathrm{T}}(k,t)$ in the high temperature range 900-1000 K for k close to the Brillouin pseudo-boundary. Despite no maxima of $C_{\mathrm{T}}(k,\omega)$ in that temperature range, I observe the minima and oscillatory behavior at 900 and 950 K but not at 1000 K. In agreement with this, the temperature of the Frenkel line demarcating propagating and non-propagating transverse modes is about 1000 K [29].

I can now directly verify the predictions for the gap $k_{\mathrm{gap}} = \frac{1}{c\tau}$ in (7.9). First, in Fig. 7.6 I observe a nearly linear relationship between k_{gap} and $\frac{1}{\tau}$ for both subcritical liquids and supercritical fluids. More computationally consuming CO_2 with smaller cell size involves smaller resolution of k and larger noise, showing a linear trend nevertheless. The increase of slope of k_{gap} vs $\frac{1}{\tau}$ at large $\frac{1}{\tau}$ at high temperature is expected because c decreases with temperature ($\frac{1}{c}$ increases). Second, I calculate c for each system from the dispersion curves in the linear regime at small k in Figure 7.4 and find them to be in acceptable

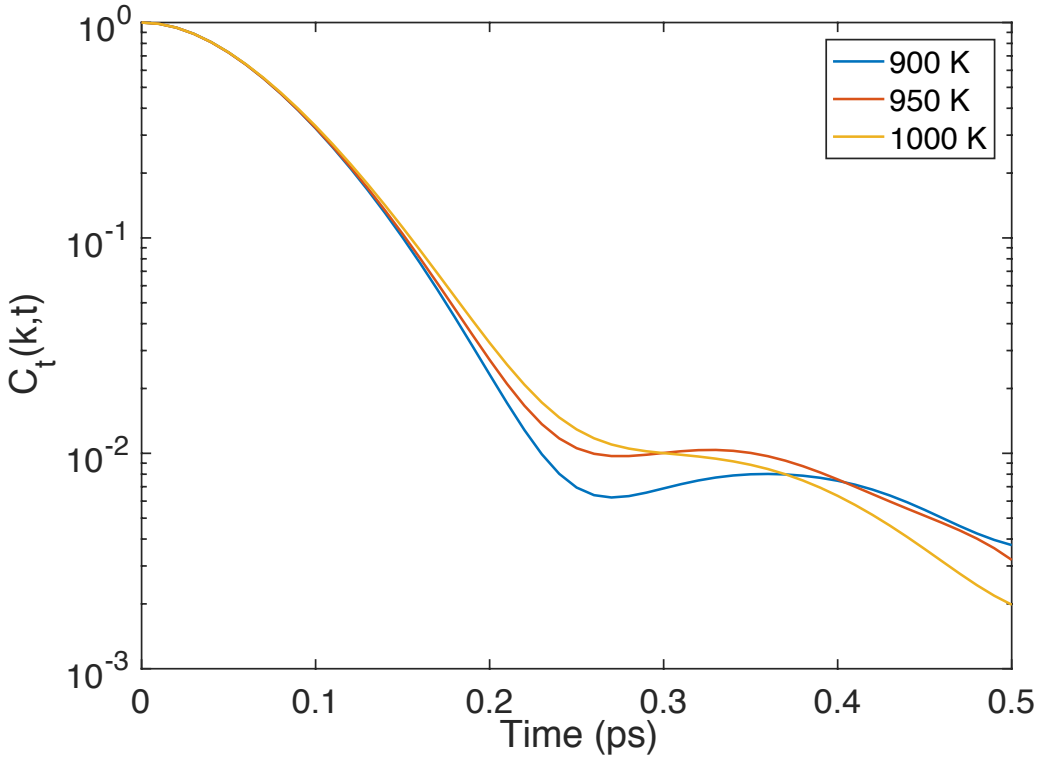

Figure 7.5: $C_T(k,t)$ of supercritical Ar near the first Brillouin pseudo-zone boundary showing the crossover from the oscillatory to monotonic behavior.

12-27 % agreement with c extracted from the linear regime in Figure 7.6 for the three systems studied.

I note that Eq. (7.8) predicts no gap in the frequency spectrum, in seeming contradiction to the commonly used Eq. (7.1): transverse frequency starts from 0 and reaches $\sqrt{c^2k_{\text{gap}}^2 - \frac{1}{\tau^2}}$, where k_{gap} is the maximal value of k. It is interesting to discuss why the gap develops in k-space rather than in the frequency domain. Eq. (7.8) follows from the solution of the Navier-Stokes equation extended by Frenkel to include the solid-like elastic response of liquids at time shorter than τ [16]. A qualitatively similar result can be also inferred from generalized hydrodynamics where the hydrodynamic transverse current correlation function is generalized to include large k and ω [7]. The

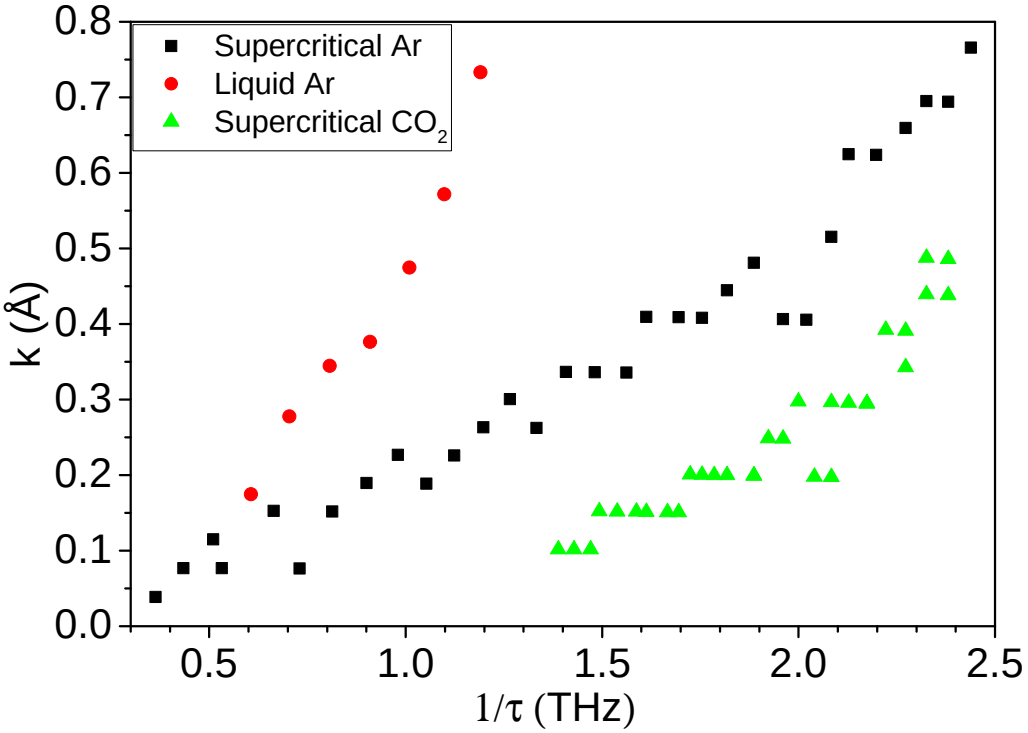

Figure 7.6: The width of k-gap vs $\frac{1}{\tau}$ for subcritical liquid Ar in the range 85-115 K, supercritical Ar in the range 200-500 K and supercritical CO_2 in the range 300-600 K.

approach assumes that the shear viscosity function K, the memory function for transverse current correlation function, exponentially decays with time τ, giving a resonant frequency in the transverse current correlation function. If I now identify K at short times with c^2, the resonant frequency becomes similar to (7.8). A gap in k-space could also be inferred from the generalized collective mode approach [142] provided one appropriately identifies some of the model parameters with τ, although the approach does not describe the dynamics with large k in the non-hydrodynamic regime.

Using (7.9), I write the condition $k > k_{\text{gap}}$ as

$$\lambda < 2\pi d_{el}$$

$$d_{el} = c\tau \tag{7.20}$$

where d_{el} is liquid elasticity length, the propagation length of a shear wave in liquids, or length over which a liquid can support shear stress [143]. The microscopic meaning of d_{el} follows from noting that particles in liquids jump with a period of τ and hence start significantly disrupting the wave continuity at distances equal to, or larger than $c\tau$, setting the longest wavelength of propagating waves. Therefore, the condition $k > k_{\mathrm{gap}}$ inherent in Eq. (7.8) is consistent with the condition that allowed wavelengths should be smaller than the wave propagation length.

In addition to providing direct evidence for the nature of transverse modes and their evolution in liquids and supercritical fluids, these results are important for understanding liquid thermodynamics. The k-gap in the transverse spectrum implies that the energy of transverse modes can be calculated as

$$E_t = \frac{V}{(2\pi)^3} \int_{k_{\mathrm{gap}}}^{k_{\mathrm{D}}} E(k) 4\pi k^2 dk \tag{7.21}$$

where V is volume, k_{D} is Debye wave vector and k_{gap} is given by (7.9). Taking $E(k) = k_{\mathrm{B}}T$ in the classical case and integrating gives

$$E_t = 2Nk_{\mathrm{B}}T \left(1 - \left(\frac{\omega_{\mathrm{F}}}{\omega_{\mathrm{D}}}\right)^3\right) \tag{7.22}$$

where N is the number of particles, $2N = \frac{Vk_{\mathrm{D}}^3}{6\pi^2}$ is the number of transverse modes in the solid and $\omega_{\mathrm{D}} = ck_{\mathrm{D}}$ is Debye frequency.

I observe that a result identical to (7.22) can be obtained if I calculate the energy of transverse modes propagating above the frequency ω_F as Eq. (7.1) predicts, i.e. if we consider a gap in the *frequency* spectrum from 0 to ω_F. Indeed, this energy can be written as $\int_{\omega_F}^{\omega_D} g(\omega) T d\omega$, where $g(\omega) = \frac{6N}{\omega_D^3}\omega^2$ is Debye density of states of transverse modes. This gives $E_t = 2Nk_BT\left(1 - \left(\frac{\omega_F}{\omega_D}\right)^3\right)$, the same as (7.22). As ω_F increases with temperature, the number of transverse modes decrease, resulting in the decrease of specific heat in agreement with the experimental results for many liquids and supercritical fluids in a wide temperature range [16]. I therefore find that from the point of view of thermodynamics, the transverse modes can be considered to have a frequency gap between 0 and ω_F, in agreement with the original assumption in (7.1).

7.4 Conclusions

In summary, I showed that how collective modes change in liquids: they transform with temperature and develop a *k*-gap in solid-like transverse spectrum which increases with the inverse of relaxation time. This applies to the supercritical state below the Frenkel line as well as to subcritical liquids. These specific results will guide future high-temperature and pressure experiments in liquid and supercritical states.

Chapter 8

Conclusions

In this thesis I reported the results of molecular dynamics simulations in two important classes of disordered materials, amorphous solids and liquids. I started by studying the diffusion in amorphous zirconolite, a potential waste form to encapsulate highly radioactive nuclear waste. I found that amorphization has a dramatic effect for diffusion. Interestingly and differently from previous understanding, diffusion increases as a result of amorphization at constant density. Another interesting insight was related to different response of diffusion of different atomic species to structural disorder. I calculated both activation energies and diffusion pre-factors. These numbers can be used to predict long-term diffusion properties in this system, and I hope they can be useful to the industry for the application based on solid diffusion. I also hope that my work stimulates future experiments where diffusion is measured so that the results can be compared. This will improve our understanding of how waste forms operate and provide the community with a recipe to predict their performance.

I subsequently studied the effects of phase coexistence and phase decomposition in Y-stabilized zirconia, the system of interest in many industrial

applications. For the first time I observed how the microstructure emerges and evolves in this system. An important part of this study was using very large system sizes which enabled microstructure formation. I showed that the microstructure importantly affects O diffusion. This has not been known before and I hope it will stimulate future experiments aimed at better understanding of zirconia performance in several important applications. Another future activity can involve simulating collision cascades in the zirconia system with different crystalline domains. This has not been done before despite a large number of MD simulations of radiation damage which were all done in mono-crystalline systems. I hope that these studies will uncover new interesting effects and will assist in our understanding of how zirconia behaves under irradiation.

I developed a new empirical potential for CO_2 with improved properties. This involved fitting to crystal properties, including structure and lattice dynamics, ab initio energies, and also tuned to the phase diagram. This model is designed for simulating both crystal and fluid. There is a large community of MD modelers interested in this system, and hope they will benefit from using the new potential. I have used this potential in mapping the Frenkel line in the supercritical state and in calculating the gap emerging in the dispersion curve in the reciprocal space in CO_2 liquid.

The remaining part of my thesis was related to the study of dynamical properties of both subcritical liquids and supercritical fluids. First, I mapped the Frenkel line for three important systems: H_2O, CO_2 and CH_4. This has not been previously achieved and will inform the community regarding the area of the supercritical phase diagram where one expects to find the crossover between the liquid-like and gas-like behavior. Knowing this area is important because it has been proposed that several important supercritical properties

change around the Frenkel line. In addition, I observed that the Frenkel line coincides with experimentally found maxima of solubility in supercritical fluids. These maxima were not previously explained. My explanation involved noting that the Frenkel line corresponds to the optimal combination of density and temperature where the density is maximal and the diffusion is still in the fast gas-like regime. My finding can serve as a guide in future applications of supercritical fluids and will result in their more efficient use: staying close to the Frenkel line implies maximal solubility and can also imply reducing temperature or pressure and therefore reducing operating costs.

Finally, I provided the first direct evidence that a gap emerges and evolves in the reciprocal space in transverse spectra of liquids. I ascertained that the gap increases with temperature and is inversely proportional to liquid relaxation time. Interestingly, the gap emerges and evolves not only in subcritical liquids but also in supercritical fluids as long as they are below the Frenkel line. Given the importance of phonons in condensed matter physics and other areas of physics, I propose that the discovery of the gap represents a paradigm change. There is an active interest in the dynamics of liquids and supercritical fluids, and I therefore hope that my results will quickly stimulate high-temperature and high-pressure experiments aimed at detecting and studying the gap in several important systems.

Bibliography

[1] R. Zallen, *The Physics of Amorphous Solids*, John Wiley & Sons, **2008**.

[2] J. Frenkel, *Kinetic Theory of Liquids*, Dover Publications, **1955**.

[3] S. Chapman, T. Cowling, *The Mathematical Theory of Non-uniform Gases: An Account of the Kinetic Theory of Viscosity, Thermal Conduction and Diffusion in Gases*, Cambridge University Press, **1995**.

[4] P. Tarazona, "Free-energy density functional for hard spheres", *Physical Review A* **1985**, *31*, 2672.

[5] N. Choudhury, S. K. Ghosh, "A perturbative density functional theory of inhomogeneous fluid mixture", *The Journal of chemical physics* **1999**, *110*, 8628–8635.

[6] L. D. Landau, E. Lifshitz, *Statistical Physics*, Oxford: Pergamon, **1969**.

[7] J. P. Boon, S. Yip, *Molecular Hydrodynamics*, Dover, **1980**.

[8] N. March, *Liquid Metals. Concepts and Theory*, Cambridge University Press, **1990**.

[9] N. March, M. P. Tosi, *Atomic Dynamics in Liquids*, Courier Corporation, **1991**.

[10] U. Balucani, M. Zoppi, *Dynamics of the Liquid State, Vol. 10*, Oxford University Press, **1995**.

[11] R. Zwanzig, *Nonequilibrium Statistical Mechanics*, Oxford University Press, **2001**.

[12] T. E. Faber, *Introduction to the Theory of Liquid Metals*, Cambridge University Press, **2010**.

[13] J. L. Barrat, J. P. Hansen, *Basic Concepts for Simple and Complex Liquids*, Cambridge University Press, **2003**.

[14] J. P. Hansen, I. R. McDonald, *Theory of Simple Liquids: With Applications to Soft Matter*, Academic Press, **2013**.

[15] A. Granato, "The specific heat of simple liquids", *Journal of Non-Crystalline Solids* **2002**, *307–310*, 376–386.

[16] K. Trachenko, V. Brazhkin, "Collective modes and thermodynamics of the liquid state", *Reports on Progress in Physics* **2015**, *79*, 016502.

[17] J. R. D. Copley, J. M. Rowe, "Short-Wavelength Collective Excitations in Liquid Rubidium Observed by Coherent Neutron Scattering", *Physical Review Letters* **1974**, *32*, 49–52.

[18] W.-C. Pilgrim, S. Hosokawa, H. Saggau, H. Sinn, E. Burkel, "Temperature dependence of collective modes in liquid sodium", *Journal of Non-Crystalline Solids* **1999**, *250*, 96–101.

[19] E. Burkel, "Phonon spectroscopy by inelastic x-ray scattering", *Reports on Progress in Physics* **2000**, *63*, 171.

[20] W. Pilgrim, C. Morkel, "State dependent particle dynamics in liquid alkali metals", *Journal of Physics: Condensed Matter* **2006**, *18*, R585.

[21] G. Ruocco, F. Sette, "The high-frequency dynamics of liquid water", *Journal of Physics: Condensed Matter* **1999**, *11*, R259.

[22] S. Hosokawa, M. Inui, Y. Kajihara, K. Matsuda, T. Ichitsubo, W.-C. Pilgrim, H. Sinn, L. González, D. González, S. Tsutsui, et al., "Transverse acoustic excitations in liquid Ga", *Physical Review Letters* **2009**, *102*, 105502.

[23] V. M. Giordano, G. Monaco, "Fingerprints of order and disorder on the high-frequency dynamics of liquids", *Proceedings of the National Academy of Sciences* **2010**, *107*, 21985–21989.

[24] V. M. Giordano, G. Monaco, "Inelastic x-ray scattering study of liquid Ga: Implications for the short-range order", *Physical Review B* **2011**, *84*, 052201.

[25] S. Hosokawa, M. Inui, Y. Kajihara, S. Tsutsui, A. Baron, "Transverse excitations in liquid Fe, Cu and Zn", *Journal of Physics: Condensed Matter* **2015**, *27*, 194104.

[26] S. Hosokawa, S. Munejiri, M. Inui, Y. Kajihara, W. Pilgrim, Y. Ohmasa, S. Tsutsui, A. Baron, F. Shimojo, K. Hoshino, "Transverse excitations in liquid Sn", *Journal of Physics: Condensed Matter* **2013**, *25*, 112101.

[27] E. Kiran, P. G. Debenedetti, C. J. Peters, *Supercritical Fluids: Fundamentals and Applications*, *Vol. 366*, Springer Science & Business Media, **2012**.

[28] J. McHardy, S. Sawan, "upercritical Fluid Cleaning: Fundamentals, Technology and Applications", *Technology and Applications Noyes Westwood NJ* **1998**.

[29] V. V. Brazhkin, Y. D. Fomin, A. G. Lyapin, V. N. Ryzhov, E. N. Tsiok, K. Trachenko, ""Liquid-gas" transition in the supercritical region: Fundamental changes in the particle dynamics", *Physical Review Letters* **2013**, *111*, 145901.

[30] V. V. Brazhkin, K. Trachenko, "What separates a liquid from a gas?", *Physics Today* **2012**, *65*, 68–69.

[31] V. V. Brazhkin, Y. D. Fomin, A. G. Lyapin, V. N. Ryzhov, K. Trachenko, "Two liquid states of matter: A new dynamic line on a phase diagram", *Physical Review E* **2012**, *85*.

[32] A. Stoneham, J. Matthews, I. Ford, "Innovative materials for fusion power plant structures: separating functions", *Journal of Physics: Condensed Matter* **2004**, *16*, S2597–S2621.

[33] S. Dudarev, J.-L. Boutard, R. Lässer, M. Caturla, P. Derlet, M. Fivel, C.-C. Fu, M. Lavrentiev, L. Malerba, M. Mrovec, D. Nguyen-Manh, K. Nordlund, M. Perlado, R. Schäublin, H. V. Swygenhoven, D. Terentyev, J. Wallenius, D. Weygand, F. Willaime, "The EU programme for modelling radiation effects in fusion reactor materials: An overview of recent advances and future goals", *Journal of Nuclear Materials* **2009**, 1–7.

[34] E. Zarkadoula, S. Daraszewicz, D. Duffy, M. Seaton, I. Todorov, K. Nordlund, M. Dove, K. Trachenko, "The nature of high-energy radiation damage in iron", *Journal of Physics: Condensed Matter* **2013**, *25*, 125402.

[35] W. Weber, R. Ewing, C. Catlow, T. de la Rubia, L. Hobbs, C. Kinoshita, H. Matzke, A. Motta, M. Nastasi, E. Salje, E. Vance, S. Zinkle, "Radiation effects in crystalline ceramics for the immobilization of high-level nuclear waste and plutonium", *Journal of Materials Research* **1998**, *13*, 1434–1484.

[36] R. Ewing, W. Weber, F. Clinard, "Radiation effects in nuclear waste forms for high-level radioactive waste", *Progress in Nuclear Energy* **1995**, *29*, 63–127.

[37] A. Ringwood, S. Kesson, N. Ware, W. Hibberson, A. Major, "Immobilisation of high level nuclear reactor wastes in SYNROC", *Nature* **1979**, *278*, 219–223.

[38] A. Ringwood, V. Oversby, S. Kesson, W. Sinclair, N. Ware, W. Hibberson, A. Major, "Immobilization of high-level nuclear reactor wastes in SYNROC: a current appraisal", *Nuclear and Chemical Waste Management* **1981**, *2*, 287–305.

[39] U.S. Nuclear Waste Technical Review Board, Technical advancements and issues associated with the permanent disposal of high-activity wastes (Report to Congress and the Secretary of Energy, June 2011), `http://www.nwtrb.gov/reports/reports.html`.

[40] K. E. Sickafus, J. A. Valdez, J. R. Williams, R. W. Grimes, H. T. Hawkins, "Radiation induced amorphization resistance in $A_2O_3BO_2$ oxides", *Nuclear Instruments and Methods in Physics Research Section B: Beam Interactions with Materials and Atoms* **2002**, *191*, 549–558.

[41] K. E. Sickafus, H. Matzke, T. Hartmann, K. Yasuda, J. A. Valdez, P. Chodak, M. Nastasi, R. A. Verrall, "Radiation damage effects in zirconia", *Journal of Nuclear Materials* **1999**, *274*, 66–77.

[42] J. S. Wang, C. N. Sheaff, B. Yoon, R. S. Addleman, C. M. Wai, "Extraction of uranium from aqueous solutions by using ionic liquid and supercritical carbon dioxide in conjunction", *Chemistry-A European Journal* **2009**, *15*, 4458–4463.

[43] C. M. Wai in ACS symposium series, *Vol. 943*, Oxford University Press, **2006**, pp. 161–170.

[44] I. Todorov, W. Smith, K. Trachenko, M. Dove, "DL_POLY 3: New dimensions in molecular dynamics simulations via massive parallelism", *Journal of Materials Chemistry* **2006**, *16*, 1911–1918.

[45] D. Frenkel, B. Smit, *Understanding Molecular Simulation: from Algorithms to Applications*, *Vol. 1*, Elsevier (formerly published by Academic Press), **2002**.

[46] M. Parrinello, A. Rahman, "Crystal Structure and Pair Potentials: A Molecular-Dynamics Study", *Physical Review Letters* **1980**, *45*, 1196–1199.

[47] M. Parrinello, A. Rahman, "Polymorphic transitions in single crystals: A new molecular dynamics method", *Journal of Applied Physics* **1981**, *52*, 7182–7190.

[48] S. Nosé, "A unified formulation of the constant temperature molecular dynamics methods", *The Journal of Chemical Physics* **1984**, *81*, 511–519.

[49] B. J. Palmer, C. Lo, "Molecular dynamics implementation of the Gibbs ensemble calculation", *The Journal of Chemical Physics* **1994**, *101*, 10899–10907.

[50] M. J. Kotelyanskii, R. Hentschke, "Gibbs-ensemble molecular dynamics: Liquid-gas equilibrium in a Lennard-Jones system", *Physical Review E* **1995**, *51*, 5116–5119.

[51] C. Bratschi, H. Huber, "Non-Hamiltonian molecular dynamics implementation of the Gibbs ensemble method. I. Algorithm", *The Journal of Chemical Physics* **2007**, *126*, 164104.

[52] A. Z. Panagiotopoulos, "Direct determination of phase coexistence properties of fluids by Monte Carlo simulation in a new ensemble", *Molecular Physics* **1987**, *61*, 813–826.

[53] P. P. Ewald, "Die Berechnung optischer und elektrostatischer Gitterpotentiale", *Annalen der Physik* **1921**, *369*, 253–287.

[54] J. E. Jones in Proceedings of the Royal Society of London A: Mathematical, Physical and Engineering Sciences, *Vol. 106*, The Royal Society, **1924**, pp. 463–477.

[55] R. A. Buckingham in Proceedings of the Royal Society of London A: Mathematical, Physical and Engineering Sciences, *Vol. 168*, The Royal Society, **1938**, pp. 264–283.

[56] J. D. Gale, A. L. Rohl, "The general utility lattice program (GULP)", *Molecular Simulation* **2003**, *29*, 291–341.

[57] J. Icenhower, D. Strachan, B. McGrail, R. Scheele, E. Rodriguez, J. Steele, V. Legore, "Dissolution kinetics of pyrochlore ceramics for the disposition of plutonium", *American Mineralogist* **2006**, *91*, 39–53.

[58] T. Geisler, U. Schaltegger, F. Tomaschek, "Re-equilibration of zircon in aqueous fluids and melts", *Elements* **2007**, *3*, 43–50.

[59] T. Geisler, K. Trachenko, S. Rios, M. Dove, E. Salje, "Impact of self-irradiation damage on the aqueous durability of zircon (ZrSiO4): implications for its suitability as a nuclear waste form", *Journal of Physics: Condensed Matter* **2003**, *15*, L597–L605.

[60] K. Trachenko, M. Dove, T. Geisler, I. Todorov, B. Smith, "Radiation damage effects and percolation theory", *Journal of Physics: Condensed Matter* **2004**, *16*, S2623–S2627.

[61] K. Trachenko, "Understanding resistance to amorphization by radiation damage", *Journal of Physics: Condensed Matter* **2004**, *16*, R1491–R1515.

[62] E. Zarkadoula, R. Devanathan, W. J. Weber, M. A. Seaton, I. T. Todorov, K. Nordlund, M. T. Dove, K. Trachenko, "High-energy radiation damage in zirconia: Modeling results", *Journal of Applied Physics* **2014**, *115*, 083507.

[63] D. M. Strachan, R. D. Scheele, E. C. Buck, A. E. Kozelisky, R. L. Sell, R. J. Elovich, W. C. Buchmiller, "Radiation damage effects in candidate titanates for Pu disposition: Zirconolite", *Journal of Nuclear Materials* **2008**, *372*, 16–31.

[64] D. Strachan, R. Scheele, A. Kozelisky, R. Sell, H. Schaef, M. O'Hara, C. Brown, W. Buchmiller in *Scientific Basis for Nuclear Waste Management XXV*, (Ed.: McGrail, BP and Cragnolino, GA), Materials Research Society Symposium Proceedings, **2002**, 461–468.

[65] P. Pöml, T. Geisler, J. Cobos-Sabaté, T. Wiss, P. Raison, P. Schmid-Beurmann, X. Deschanels, C. Jégou, J. Heimink, A. Putnis, "The mechanism of the hydrothermal alteration of cerium- and plutonium-doped zirconolite", *Journal of Nuclear Materials* **2011**, *410*, 10–23.

[66] L. D. Landau, E. M. Lifshitz, *Theory of Elasticity*, Pergamon Press Oxford, **1986**.

[67] J. C. Dyre, "Colloquium: The glass transition and elastic models of glass-forming liquids", *Reviews of Modern Physics* **2006**, *78*, 953–972.

[68] V. Brazhkin, A. Lyapin, V. Goncharova, O. Stalgorova, S. Popova, "Elastic softness of amorphous tetrahedrally bonded GaSb and $(Ge_2)_0.27(GaSb)_0.73$ semiconductors", *Physical Review B* **1997**, *56*, 990–993.

[69] J. M. Ziman, *Models of Disorder: the Theoretical Physics of Homogeneously Disordered Systems*, CUP Archive, **1979**.

[70] A. I. Chumakov, G. Monaco, A. Fontana, A. Bosak, R. P. Hermann, D. Bessas, B. Wehinger, W. A. Crichton, M. Krisch, R. Rüffer, G. Baldi, G. Carini Jr., G. Carini, G. D'Angelo, E. Gilioli, G. Tripodo, M. Zanatta, B. Winkler, V. Milman, K. Refson, M. T. Dove, N. Dubrovinskaia, L. Dubrovinsky, R. Keding, Y. Z. Yue, "Role of Disorder in the Thermodynamics and Atomic Dynamics of Glasses", *Physical Review Letters* **2014**, *112*, 025502.

[71] V. V. Brazhkin, K. Trachenko, *Journal of Physical Chemistry B* **2014**, *118*, 11417–11427.

[72] E. Zarkadoula, S. L. Daraszewicz, D. M. Duffy, M. A. Seaton, I. T. Todorov, K. Nordlund, M. T. Dove, K. Trachenko, "The nature of the high-energy radiation damage in iron", *Journal of Physics: Condensed Matter* **2013**, *25*.

[73] H. R. Foxhall, K. P. Travis, L. W. Hobbs, S. C. Rich, S. L. Owens, "Understanding the radiation-induced amorphization of zirconolite using molecular dynamics and connectivity topology analysis", *Philosophical Magazine* **2013**, *93*, 328–355.

[74] H. R. Foxhall, K. P. Travis, S. L. Owens, "Effect of plutonium doping on radiation damage in zirconolite: A computer simulation study", *Journal of Nuclear Materials* **2014**, *444*, 220–228.

[75] H. F. Chappell, M. T. Dove, K. Trachenko, R. E. A. McKnight, M. A. Carpenter, S. A. T. Redfern, "Structural changes in zirconolite under α-decay", *Journal of Physics: Condensed Matter* **2013**, *25*.

[76] W. Weber, J. Wald, H. Matzke, "Effects of self-radiation damage in Cm-doped $GdTi_2O_7$ and $CaZrTi_2O_7$", *Journal of Nuclear Materials* **1986**, *138*, 196–209.

[77] C. Catlow, "Point Defect and Electronic Properties of Uranium Dioxide", *Proceedings of the Royal Society A, covering mathematics and physical sciences* **1977**, *353*, 533–561.

[78] J. Chevalier, L. Gremillard, A. V. Virkar, D. R. Clarke, "The tetragonal-monoclinic transformation in zirconia: Lessons learned and future trends", *Journal of the American Ceramic Society* **2009**, *92*, 1901–1920.

[79] M. Yashima, M. Kakihana, M. Yoshimura, "Metastable-stable phase diagrams in the zirconia-containing systems utilized in solid-oxide fuel cell application", *Solid State Ionics* **1996**, *86-88*, 1131–1149.

[80] N. Mahato, A. Banerjee, A. Gupta, S. Omar, K. Balani, "Progress in Material Selection for Solid Oxide Fuel Cell Technology: A Review", *Progress in Materials Science* **2015**, *72*, 141–337.

[81] O. Fabrichnaya, F. Aldinger, "Assessment of thermodynamic parameters in the system ZrO2 – Y2O3 – Al2O3", *Zeitschrift für Metallkunde* **2004**, *95*, 27–39.

[82] J. Goff, W. Hayes, S. Hull, M. Hutchings, K. Clausen, "Defect structure of yttria-stabilized zirconia and its influence on the ionic conductivity at elevated temperatures", *Physical Review B* **1999**, *59*, 14202–14219.

[83] S. García-Martín, D. Fagg, J. Irvine, "Characterization of diffuse scattering in Yttria-stabilized zirconia by electron diffraction and high-resolution transmission electron microscopy", *Chemistry of Materials* **2008**, 5933–5938.

[84] H. Kim, J. Y. Moon, J.-H. Lee, J.-K. Lee, Y.-W. Heo, J.-J. Kim, H. S. Lee, "Transmission Electron Microscopy Study of 3.2 YSZ Single Crystals Manufactured by the Skull Melting Method", *Journal of Nanoscience and Nanotechnology* **2014**, *14*, 7961–7964.

[85] E. V. Stefanovich, A. L. Shluger, C. R. A. Catlow, “Theoretical study of the stabilization of cubic-phase ZrO2 by impurities”, *Physical Review B* **1994**, *49*, 11560–11571.

[86] X. Xia, R. Oldman, R. Catlow, “Computational modeling study of bulk and surface of yttria-stabilized cubic zirconia”, *Chemistry of Materials* **2009**, *21*, 3576–3585.

[87] P. K. Schelling, S. R. Phillpot, D. Wolf, “Mechanism of the cubic-to-tetragonal phase transition in zirconia and yttria-stabilized zirconia by molecular-dynamics simulation”, *Journal of the American Ceramic Society* **2001**, *84*, 1609–1619.

[88] D. S. Aidhy, Y. Zhang, W. J. Weber, “Stabilizing nanocrystalline grains in ceramic-oxides.”, *Physical Chemistry Chemical Physics* **2013**, *15*, 18915–20.

[89] M. Kilo, C. Argirusis, G. Borchardt, R. a. Jackson, “Oxygen diffusion in yttria stabilised zirconia–experimental results and molecular dynamics calculationsPresented at the 78th International Bunsen Discussion Meeting on "Complex Oxides: Defect Chemistry, Transport and Chemical Reaction", Vaals, The Netherl”, *Physical Chemistry Chemical Physics* **2003**, *5*, 2219.

[90] X. Li, B. Hafskjold, “Molecular dynamics simulations of yttrium-stabilized zirconia”, *Journal of Physics: Condensed Matter* **1995**, *7*, 1255.

[91] M. Filal, C. Petot, M. Mokchah, C. Chateau, J. L. Carpentier, “Ionic conductivity of yttrium-doped zirconia and the "composite effect"”, *Solid State Ionics* **1995**, *80*, 27–35.

[92] P. Manning, “The kinetics of oxygen transport in 9.5 mol % single crystal yttria stabilised zirconia”, *Solid State Ionics* **1997**, *100*, 1–10.

[93] J. Luo, D. P. Almond, R. Stevens, "Ionic mobilities and association energies from an analysis of electrical impedance of ZrO_2-Y_2O_3 alloys", *Journal of the American Ceramic Society* **2000**, *83*, 1703–1708.

[94] D. Marrocchelli, P. A. Madden, S. T. Norberg, S. Hull, "Structural disorder in doped zirconias, part II: Vacancy ordering effects and the conductivity maximum", *Chemistry of Materials* **2011**, *23*, 1365–1373.

[95] I. R. Gibson, J. T. S. Irvine, "Study of the order-disorder transition in yttria-stabilised zirconia by neutron diffraction", *Journal of Materials Chemistry* **1996**, *6*, 895.

[96] R. Krishnamurthy, Y.-G. Yoon, D. J. Srolovitz, R. Car, "Oxygen Diffusion in Yttria-Stabilized Zirconia: A New Simulation Model", *Journal of the American Ceramic Society* **2004**, *1830*, 1821–1830.

[97] R. Pornprasertsuk, P. Ramanarayanan, C. B. Musgrave, F. B. Prinz, "Predicting ionic conductivity of solid oxide fuel cell electrolyte from first principles", *Journal of Applied Physics* **2005**, *98*, 1–8.

[98] J. E. Jaffe, R. a. Bachorz, M. Gutowski, "Low-temperature polymorphs of ZrO2 and HfO2: A density-functional theory study", *Physical Review B* **2005**, *72*, 1–9.

[99] A. J. G. Lunt, M. Y. Xie, N. Baimpas, S. Y. Zhang, S. Kabra, J. Kelleher, T. K. Neo, A. M. Korsunsky, "Calculations of single crystal elastic constants for yttria partially stabilised zirconia from powder diffraction data", *Journal of Applied Physics* **2014**, *116*.

[100] D. Marrocchelli, P. A. Madden, S. T. Norberg, S. Hull, "Structural disorder in doped zirconias, part II: Vacancy ordering effects and the conductivity maximum", *Chemistry of Materials* **2011**, *23*, 1356–1364.

[101] D. W. Strickler, W. G. Carlson, "Ionic Conductivity of Cubic Solid Solutions in the System CaO-Y_2O_3-ZrO_2", *Journal of the American Ceramic Society* **1964**, *47*, 122–127.

[102] R. Devanathan, W. J. Weber, S. C. Singhal, J. D. Gale, "Computer simulation of defects and oxygen transport in yttria-stabilized zirconia", *Solid State Ionics* **2006**, *177*, 1251–1258.

[103] J. G. Harris, K. H. Yung, "Carbon Dioxide's Liquid-Vapor Coexistence Curve And Critical Properties as Predicted by a Simple Molecular Model", *The Journal of Physical Chemistry* **1995**, *99*, 12021–12024.

[104] J. J. Potoff, J. I. Siepmann, "Vapor–liquid equilibria of mixtures containing alkanes, carbon dioxide, and nitrogen", *AIChE Journal* **2001**, *47*, 1676–1682.

[105] E. Aprà, E. J. Bylaska, D. J. Dean, A. Fortunelli, F. Gao, P. S. Krstić, J. C. Wells, T. L. Windus, "NWChem for materials science", *Computational Materials Science* **2003**, *28*, 209–221.

[106] M. Valiev, E. J. Bylaska, N. Govind, K. Kowalski, T. P. Straatsma, H. J. Van Dam, D. Wang, J. Nieplocha, E. Apra, T. L. Windus, et al., "NWChem: a comprehensive and scalable open-source solution for large scale molecular simulations", *Computer Physics Communications* **2010**, *181*, 1477–1489.

[107] A. Stone, M. Alderton, "Distributed multipole analysis", *Molecular Physics* **1985**, *56*, 1047–1064.

[108] A. Misquitta, A. Stone, "CamCASP: a program for studying intermolecular interactions and for the calculation of molecular properties in distributed form", *University of Cambridge* **2007**.

[109] `http://webbook.nist.gov/chemistry/fluid`.

[110] M. G. Martin, "MCCCS Towhee: a tool for Monte Carlo molecular simulation", *Molecular Simulation* **2013**, *39*, 1212–1222.

[111] B. Smit, P. D. Smedt, D. Frenkel, "Computer simulations in the Gibbs ensemble", *Molecular Physics* **1989**, *68*, 931–950.

[112] J. A. Zollweg, G. W. Mulholland, "On the Law of the Rectilinear Diameter", *The Journal of Chemical Physics* **1972**, *57*, 1021–1025.

[113] U. Haarhaus, P. Swidersky, G. Schneider, "High-pressure investigations on the solubility of dispersion dyestuffs in supercritical gases by VIS/NIR-spectroscopy. Part I — 1,4-Bis-(octadecylamino)-9,10-anthraquinone and disperse orange in CO_2 and N_2O Up to 180 MPa", *Journal of Supercritical Fluids* **1995**, *8*, 100–106.

[114] P. Swidersky, D. Tuma, G. Schneider, "High-pressure investigations on the solubility of anthraquinone dyestuffs in supercritical gases by VIS-spectroscopy. Part II—1,4-Bis-(n-alkylamino)-9,10-anthraquinones and disperse Red 11 in CO_2, N_2O, and CHF_3 up to 180 MPa", *Journal of Supercritical Fluids* **1996**, *9*, 12–18.

[115] M. Mchugh, M. Paulaitis, "Solid solubilities of naphthalene and biphenyl in supercritical carbon dioxide", *Journal of Chemical and Engineering Data* **1980**, *25*, 326–329.

[116] D. Tuma, G. Schneider, "High-pressure solubility of disperse dyes in near-and supercritical fluids: measurements up to 100MPa by a static method", *Journal of Supercritical Fluids* **1998**, *13*, 37–42.

[117] D. Tuma, G. Schneider, "Determination of the solubilities of dyestuffs in near-and supercritical fluids by a static method up to 180 MPa", *Fluid Phase Equilibria* **1999**, *158*, 743–757.

[118] T. Kraska, K. Leonhard, D. Tuma, G. Schneider, "Correlation of the solubility of low-volatile organic compounds in near-and supercritical fluids. Part I: applications to adamantane and β-carotene", *Journal of Supercritical Fluids* **2002**, *23*, 209–224.

[119] T. Kraska, D. Tuma, "High-pressure phase equilibria in binary and ternary mixtures with one near- or supercritical and one high-molecular component. New insights for application and theory", *Journal of Materials Science* **2006**, *41*, 1547–1556.

[120] U. K. Deiters, I. Swaid, "Calculation of Fluid-Fluid and Solid-Fluid Phase Equilibria in Binary Mixtures at High Pressures", *Berichte der Bunsengesellschaft für physikalische Chemie* **1984**, *88*, 791–796.

[121] V. V. Brazhkin, Y. D. Fomin, A. G. Lyapin, V. N. Ryzhov, K. Trachenko, "Universal crossover of liquid dynamics in supercritical region", *JETP Letters* **2012**, *95*, 164–169.

[122] A. Fiege, T. Aspelmeier, A. Zippelius, "Long-Time Tails and Cage Effect in Driven Granular Fluids", *Physical Review Letters* **2009**, *102*, 098001.

[123] L. Xu, P. Kumar, S. V. Buldyrev, S.-H. Chen, P. H. Poole, F. Sciortino, H. E. Stanley, "Relation between the Widom line and the dynamic crossover in systems with a liquid–liquid phase transition", *Proceedings of the National Academy of Sciences of the United States of America* **2005**, *102*, 16558–16562.

[124] D. Bolmatov, V. V. Brazhkin, K. Trachenko, "Thermodynamic behavior of supercritical matter", *Nature Communications* **2013**, *4*.

[125] J. Zielkiewicz, "Structural properties of water: Comparison of the SPC, SPCE, TIP4P, and TIP5P models of water", *The Journal of Chemical Physics* **2005**, *123*, 104501.

[126] C. Vega, J. L. F. Abascal, "Simulating water with rigid non-polarizable models: a general perspective", *Physical Chemistry Chemical Physics* **2011**, *13*, 19663–19688.

[127] J. Abascal, C. Vega, "A general purpose model for the condensed phases of water: TIP4P/2005", *Journal of Chemical Physics* **2005**, *123*.

[128] I. Skarmoutsos, L. Kampanakis, J. Samios, "Investigation of the vapor-liquid equilibrium and supercritical phase of pure methane via computer simulations", *Journal of Molecular Liquids* **2005**, *117*, 33–41.

[129] R. Span, W. Wagner, "A new equation of state for carbon dioxide covering the fluid region from the triple-point temperature to 1100 K at pressures up to 800 MPa", *Journal of Physical and Chemical Reference Data* **1996**, *25*, 1509–1596.

[130] V. M. Giordano, F. Datchi, A. Dewaele, "Melting curve and fluid equation of state of carbon dioxide at high pressure and high temperature", *Journal of Chemical Physics* **2006**, *125*.

[131] L. Spanu, D. Donadio, D. Hohl, G. Galli, "Theoretical investigation of methane under pressure", *Journal of Chemical Physics* **2009**, *130*.

[132] E. H. Abramson, "Melting curves of argon and methane", *High Pressure Research* **2011**, *31*, 549–554.

[133] K. Trachenko, V. Brazhkin, D. Bolmatov, "Dynamic transition of supercritical hydrogen: Defining the boundary between interior and atmosphere in gas giants", *Physical Review E* **2014**, *89*, 032126.

[134] L. Landau, E. Lifshitz, *Fluid Mechanics. 1987*, Butterworth-Heinemann, **1987**.

[135] T. Scopigno, G. Ruocco, F. Sette, "Microscopic dynamics in liquid metals: The experimental point of view", *Reviews of Modern Physics* **2005**, *77*, 881–933.

[136] M. Grimsditch, R. Bhadra, L. M. Torell, "Shear waves through the glass-liquid transformation", *Physical Review Letters* **1989**, *62*, 2616–2619.

[137] F. Scarponi, L. Comez, D. Fioretto, L. Palmieri, "Brillouin light scattering from transverse and longitudinal acoustic waves in glycerol", *Physical Review B* **2004**, *70*, 054203.

[138] E. Pontecorvo, M. Krisch, A. Cunsolo, G. Monaco, A. Mermet, R. Verbeni, F. Sette, G. Ruocco, "High-frequency longitudinal and transverse dynamics in water", *Physical Review E* **2005**, *71*, 011501.

[139] A. Cunsolo, C. Kodituwakku, F. Bencivenga, M. Frontzek, B. Leu, A. Said, "Transverse dynamics of water across the melting point: A parallel neutron and x-ray inelastic scattering study", *Physical Review B* **2012**, *85*, 174305.

[140] W. Kob, H. C. Andersen, "Testing mode-coupling theory for a supercooled binary Lennard-Jones mixture. II. Intermediate scattering function and dynamic susceptibility", *Physical Review E* **1995**, *52*, 4134.

[141] L. Van Hove, "Correlations in Space and Time and Born Approximation Scattering in Systems of Interacting Particles", *Physical Review* **1954**, *95*, 249–262.

[142] T. Bryk, "Non-hydrodynamic collective modes in liquid metals and alloys", *The European Physical Journal Special Topics* **2011**, *196*, 65–83.

[143] K. Trachenko, V. Brazhkin, "Understanding the problem of glass transition on the basis of elastic waves in a liquid", *Journal of Physics: Condensed Matter* **2009**, *21*, 425104.

Appendix

List of Publication

1. C. Yang, E. Zarkadoula, M. T. Dove, I. T. Todorov, T. Geisler, V. V. Brazhkin, K. Trachenko, "Solid-state diffusion in amorphous zirconolite", *Journal of Applied Physics*, **116** (18), 184901, 2014

2. C. Yang, V. V. Brazhkin, M. T. Dove, K. Trachenko, "Frenkel line and solubility maximum in supercritical fluids", *Physical Review E*, **91** (1), 12112, 2015

3. C. Yang, V. V. Brazhkin, M. T. Dove, K. Trachenko, "Emergence and evolution of k-gap in spectra of liquid and supercritical states" (submitted)

4. C. Yang, K. Trachenko, S. Hull, M. T. Dove, "Microstructure and oxygen diffusion in yttrium-stabilised cubic zirconia" (in preparation)